UNIVERSITY OF LIVERPOOL

Simulate fluid transport in gas diffusion layers of PEM Fuel Cells using lattice Boltzmann method and X-ray computed tomography

Thesis submitted in accordance with the requirements of the University of Liverpool for the degree of Doctor in Philosophy by

Yuan Gao

December 2012

Abstract

Polymer electrolyte fuel cell (PEMFC) is a devise to convert chemical energy to electricity by harvesting the electrons released in oxidation of hydrogen. The performance of PEMFC is affected by many factors, and one of them is gas flow in the porous gas diffusion layer (GDL) and catalyst layer (CL). The main objective of this PhD project is to investigate the impact of micron-scale pore structures of GDL on fluid flow using a combination of numerical modelling and imaging technology with a view to improve fuel cell design. X-ray computed micro-tomography was developed to visualize 3D structures of GDL at scales of one microns, and focused ion beam (FIB) scanning electron microscope was developed to visualize the 3D structure of the CL at a scale of a few nano-metres. The 3D structures were then combined with the lattice Boltzmann equation (LBE) model to investigate the gas flow through the GDL. The simulated microscopic velocity not only reveals the detailed gas flow paths in the GDL, but also provides a way to estimate the macroscopic transport parameters, including anisotropic permeability, diffusivity and tortuosity, some of which are difficult to measure experimentally. The attraction of the LBE methods is their flexibility in dealing with different microscopic forces and complicated boundaries. Different LBE methods have been developed in the literature, including single-relaxation time LBE model and multiple-relaxation time LBE model, with the former being claimed to be superior to the later. In this project, I thoroughly investigated the performance of the single-relaxation time LBE and the multiple-relaxation time LBE for simulating single-phase flow in GDL and other porous media. The results showed that, using only two thirds of the computational time of multiple-relaxation LBE model, the single-relaxation time LEB model could give reasonable results when the relaxation time was unity. For unity relaxation time, the fluid viscosity can be recovered by adjusting the size of the time step. This is significant for 3D simulations which are computation-demanded. Practical applications need to stack the fuel cells and to avoid gas leakage, in which the GDLs will be non-uniformly compressed. The impact of the compression on gas flow and hence fuel cell performance was also investigated. The by-product of fuel cells is water generated at the cathode; how to drain the water is a critical issue in fuel cell design. Based on the 3D x-ray images, I simulated the movement of liquid water through GDL from the catalyst layer to the channel with a view to investigate the impact of making GDL hydrophobic on water flow pattern. Another contribution of this thesis is gas flow in the catalyst layer in which the averaged

pore sizes is less than one micron and the Knudsen number cannot be neglected. The pore geometry of the pore in catalyst layer was simplified into a bundle of tubes with various diameters that can be calculated from the pore-size distribution. A model for gas flow in each tube is then simulated; the results show that the permeability of the catalyst layer is not constant but varies with Knudsen number, meaning that the permeability of catalyst layer for oxygen, water vapour, nitrogen and hydrogen is different. Assuming a constant permeability for all the gases, as used in the available fuel cell models in literature, could give rise to significant errors. The work presented in this thesis improved our understanding of gas flow processes in fuel cells, and would offer a tool to help fuel cell design.

Acknowledgement

I would like to thank my supervisors, Dr. Xiaoxian Zhang and Dr. Jian Guo Zhou for their guidance, encouragement and support during all stages of my PhD studies at Liverpool.

I am also grateful to UK Technology Strategy Board (TSB) for funding my PhD study through the consortium Project (TP/6/S/K3032H), and industrial and academic partners AVL list GmbH, Intelligent Energy Ltd., Johnson Matthey Fuel Cells Ltd., Saati Group Inc., Technical Fibre Products Ltd, Loughborough University and the University of Birmingham for their help over the past four years. I especially like to thank Dr. Pratap Rama at Loughborough University and Dr. Hossein Ostadi at Birmingham University for their help in fuel cell and x-ray computed tomography, respectively. I would also like to thank all my colleagues and staff in the School of Engineering at the University of Liverpool for their generous help, technical support and routine services.

We also thank my family, especially my husband, mum and mum-in-law, for their help, support and care over the last three years. Finally, I thank my baby son, Hou Bao, for being a good boy when I wrote my thesis.

List of Publications

[1] **Y. Gao** , X. Zhang, P. Rama, Y. Liu, R. Chen, H. Ostadi, K. Jiang (2012) Calculating the Anisotropic Permeability of Porous Media Using the Lattice Boltzmann Method and X-ray Computed Tomography. ***Transport in Porous media***. 92(2) 157-173

[2] **Y. Gao** , X. Zhang, P. Rama, Y. Liu, R. Chen, H. Ostadi, K. Jiang (2012) Modelling fluid flow in the gas diffusion layers in PEMFC using the multiple relaxation time Lattice Boltzmann method . ***Fuel Cells*** .12(3) 365-381,DOI: 10.1002/fuce.201000074

[3] **Y. Gao** , X. Zhang, P. Rama, Y. Liu, R. Chen, H. Ostadi, K. Jiang (2012) An improved MRT lattice Boltzmann model for calculating anisotropic permeability of compressed and uncompressed carbon cloth gas diffusion layers based on X-ray computed micro-tomography. ***Journal of Fuel Cell Science and Technology.*** DOI: 10.1115/1.4006796

[4] **Y. Gao** , X. Zhang, P. Rama, Y. Liu, R. Chen, H. Ostadi, K. Jiang (2012) Lattice Boltzmann simulation of water-gas flow in 3D porous gas diffusion layers of fuel cells reconstructed from micro-tomography. ***Computers and Mathematics with Applications*** (Accept)

[5] P. Rama, Y. Liu, R. Chen, H. Ostadi, K. Jiang, X. Zhang, **Y. Gao**, P. Grassini, D. Brivio, "Determination of the anisotropic permeability of a carbon cloth gas diffusion layer through X-ray computer micro-tomography and single-phase lattice Boltzmann simulation", ***International Journal for Numerical Methods in Fluids***, 10 Oct 2011, 67(4), 518-530,DOI: 10.1002/fld.2378, ISSN (print): 0271-2091. ISSN (online): 1097-0363

[6]Pratap Rama, Yu Liu, Rui Chen, Hossein Ostadi, Kyle Jiang, **Yuan Gao**, Xiaoxian Zhang, Rosemary Fisher, Michael Jeschke, "Multi-Scale Modelling of Single-Phase Multi-Component Transport in the Cathode Gas Diffusion Layer of a Polymer Electrolyte Fuel Cell", May 2010 ,***ACS Energy & Fuels***, 24 (5), pp 3130–3143, ISSN: 0887-0624

[7] Pratap Rama, Yu Liu, Rui Chen, Hossein Ostadi , Kyle Jiang, **Yuan Gao** , Xiaoxian Zhang, Davide Brivio, Paolo Grassini "A Numerical Study of Structural Change and Anisotropic Permeability in Compressed Carbon Cloth Polymer Electrolyte Fuel Cell Gas Diffusion Layers. " DEC 2010, ***Fuel Cells*** ,DOI:10.1002/fuce.201000037

[8] Rama P, Liu Y, Chen R, Ostadi H, Jiang K, **Gao Y**, Zhang XX (2011) Simulation of Liquid Water Breakthrough in a Nano-Tomography Reconstruction of a Carbon Paper Gas Diffusion Layer. JAN 2011, ***AICHE Journal*** ,DOI:10.1002/aic.12581

Contents

Chapter 1 Introduction

1.1 Polymer exchange membrane fuel cell

Polymer exchange membrane fuel cell (PEMFC) is a device to convert chemical energy to electricity by harvesting the electrons released in oxidation of hydrogen. PEMFC has been regarded as one of the most promising alternative technologies to combustion engine in car industry in the future due to its high efficiency, low emissions, quiet operation, quick start-up, refuelling, and sustainable availability of hydrogen [1]. Over the past few decades, significant efforts and progresses have been made to develop and improve PEMFC for mobile, portable and stationary applications [2]. The main components of PEMFC are cathode, anode, a proton membrane, and two bi-polar-plates - one on the cathode side and the other on the anode side. Figure 1.1 shows the schematic structure of a typical PEMFC.

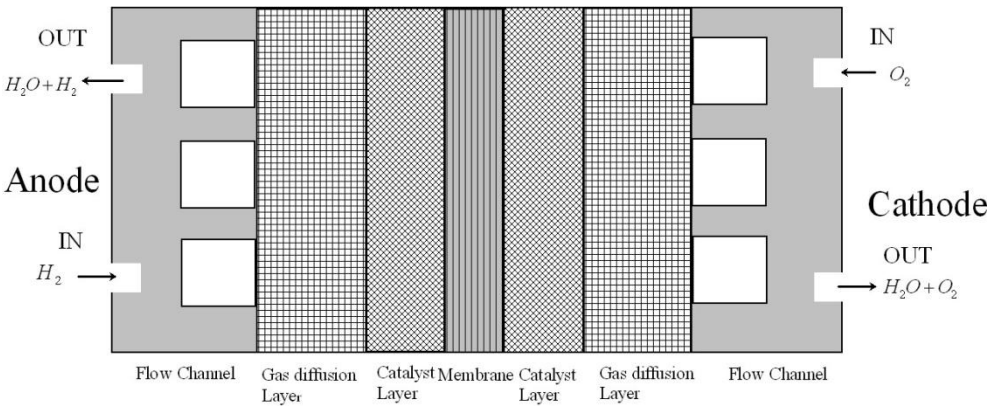

Figure1. 1. Schematic structure of the PEMFC

The polymer electrolyte membrane is an essential component of PEMFC. Its function is to provide a conductive path for the protons and separate the reactant gases at the cathode and anode. When the fuel cell is in operation, pressurized hydrogen flows to the bi-polar plate first, and then diffuses through a gas diffusion layer to the catalyst layer where it is oxidised to protons and electrons with the help of a catalyst. The electrons travel, through the gas diffusion layer, back to the bi-polar plate and then to an external circuit before reaching the cathode, through which the energy is harvested. The protons, in the

meantime, travel through the electrolyte membrane to the cathode; at the cathode, the electrons and protons react with oxygen to form water. To ensure good performance, the PEMFC electrolyte membrane needs to meet the following requirements: high ionic conductivity, adequate to stop diffusion of oxygen from the cathode to the anode, low electronic conductivity to protons, and low-cost. Proton transport in the electrolyte is highly dependent on liquid water in the electrolyte. The standard electrolyte materials used in PEMFC are fully fluorinated Teflon-based family [1, 2].

The polymer membrane is sandwiched between two sheets of gas diffusion layers. The functions of gas diffusion layers (GDL) are i) to act as a gas diffuser to transport gas from gas channel to the catalyst layer where electrochemical reactions take place, and ii) to provide mechanical support to the electrolyte membrane. At the anode, the GDL provides electrical pathway for the electrons to move to the bi-polar plate; and at the cathode, apart from providing pathway for oxygen to move to the catalyst layer, it also needs to drain the liquid water generated at the catalyst layer into the channel. The commonly used gas diffusion layer is carbon-based, either in woven-cloth form, or in non-woven carbon fiber. The GDL used in the cathode often contains hydrophobic materials, such as polytetrafluoroethylene, to prevent water flooding [1]. To fascinate electrochemical reactions, a catalyst layer coated with platinum is often mounted to the anode and cathode GDLs on the side adjacent to the electrolyte membrane.

Gas diffusion layers are highly porous with a porosity >70% and thickness from 100 to 300 μm [3]. The pore size in the GDL is in the range of 2 to 25 μm. These highly porous media allow reactant species to transport from bi-polar plate to the catalyst layers where the electrochemical reactions take place. In addition, the carbon matrix in the GDL is electronically connected to the bipolar plates.

The catalyst layer is in direct contact with the membrane on its one side and the gas diffusion layer on the other. The thickness of the CL is approximately 10 μm. Inside the catalyst layer at the anode, the hydrogen is broken into protons and electrons in oxidizing reaction with the help of a catalyst. In modern PEMFC, both pure platinum and metal are used as catalysts; the catalysts are coated, non-uniformly, on the surface of the carbon-

based materials. The catalyst layers are expensive, which, together with the electrolyte membrane, are the main costs of the PEMFC [3].

Outside of the fuel cell are the bi-polar plates as shown Figure 1.1. Channels are etched on two sides apart from end plates of the plate. Apart from supporting the cell, the bi-polar plates have many other functions: distributing hydrogen and oxygen within the cell, separating the individual cells in fuel cell stack, collecting the current, carrying water away from the catalyst layer at the cathode, humidifying gases at the anode, and keeping the cells cool[4, 5]. In modern fuel cells, the channels on the plate can be etched in different forms, including straight channels, serpentine channel, parallel channel, or pin-type channels. Materials of the bi-polar plates are chosen based on their chemical compatibility, resistance to corrosion, cost, density, electronic conductivity, ability to distribute gas, manufacturability, stack volume/kW, material strength, and thermal conductivity. The commonly used materials are stainless steel, titanium, nonporous graphite, or doped polymers. Several composite materials are also investigated as materials for bipolar plates.

1.2 The working principle of PEM fuel cells

The principle of the PEMFC is to oxidize hydrogen and reduce oxygen [6, 7]. The overall chemical reaction is

$$2H_2 + O_2 = 2H_2O \tag{1. 1}$$

Figure 1.2 shows where the reducing and oxidizing reactions take place. At the anode, the oxidizing reaction breaks the hydrogen into protons and electrons as follows

$$H_2 \rightarrow 2H^+ + 2e^- \tag{1. 2}$$

and at the cathode, the reducing reaction forms water:

$$O_2 + 4H^+ + 4e^- = 2H_2O \tag{1. 3}$$

To ensure above reaction to proceed, the design of the PEMFC must consider: i) the hydrogen and oxygen need to reach the catalysts layers at cathode and anode, respectively, with ease, ii) the electrons released at the anode need to be able to transfer to the bipolar plate first and then to the external circuit, iii) the heat produced in the above electrochemical reaction can be released through transfer to the GDL and then to the flow channels. The pores in the GDL provide pathways for oxygen and hydrogen to flow; they also increase uniformity of gas distribution over the catalyst layers so as to improve electrochemical reactions [8]. The performance of the fuel cells depends on GDL materials. As such, understanding the transport properties of the GDL, such as its porosity, permeability, thermal conductivity, pore distribution and hydrophobicity, is important in fuel cell design.

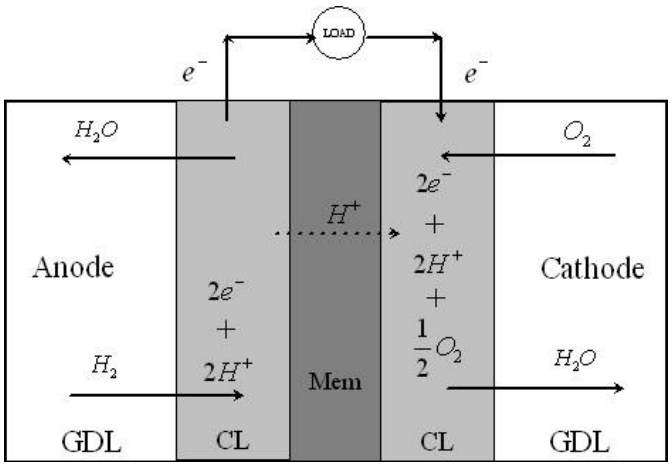

Figure1. 2. Schematic illustration of charge and electron movements in PEMFC

1.3 The gas diffusion layers

As stated above, the GDL is to transfer and distribute the reactant gases from channels in the bipolar plates to the reactive sites in the catalysts layers. In the meantime, the GDL at the anode also needs to move the electrons back to the bipolar plate; the GDL at the cathode to transfer liquid water from the catalyst layer to the channel. Since the cathode GDL needs to transfer oxygen from the channel to catalyst layer and liquid water from catalyst layer to channel, a special design of GDL is needed. This is one of most challenging tasks in PEM fuel cells. To ensure liquid water and oxygen to move

simultaneously in opposite directions, the cathode GDL is usually made heterogeneously hydrophobic in that some regions are hydrophobic and some are hydrophilic. This can force water to flow along a few channels, leaving some space for oxygen to flow though. The requirements for a good GDL material are summarized as follows:

- Distribute reactant gases uniformly to the catalyst layers at both cathode and anode.
- Provide pathways for water removal at the cathode.
- Conduct electrons and heat at the anode.
- Provide mechanical support to the electrolyte membrane.
- Resist compression in fuel cell stack.
- Be porous in both in-plane direction and through-plane direction.
- Be electrically and thermally conductive in both in-plane and through plane directions.
- Be heterogeneously hydrophobic at the cathode to ease gas and liquid water movement in opposite directions.

Commercial GDLs are made into either carbon paper or woven carbon cloth. In this project, we will use both. The carbon cloth GDL is textile, consisting of woven bundles of 200-300 carbon fibrils per yam; carbon paper GDL consists of randomly dispersed carbon fibrils, and the diameter of each individual carbon fibril is around 5-20 μm; the diameter of the bundle is in the range of 400-500 μm [9, 10]. The largest pore diameter in carbon paper and carbon cloth GDL are from 40 μm to 250 μm. The porosity of the GDL depends upon fibril content, the size of the bundles and the woven structure. For the cathode GDL, the side mounted with the catalyst layer is commonly coated by a micro porous layer in order to improve electrical conductivity between catalyst and the GDL. The materials in a GDL influence both electrical conductivity and gas diffusion. The gas flows in the pore space, and the electrons through the solid fibres. A GDL with high porosity is easy for gas to flow, but hard for electrons to move because of the increase in electrical resistance; this is conflict. As such, there is an optimal porosity at which the fuel cell performance peaks. The value of this optimal porosity depends not only on GDL materials but also on its pore geometry. The optimal porosity is an important parameter in fuel cell design.

Figures 1.3 and 1.4 show the scanning electron microscope (SEM) images of a carbon paper and a woven carbon cloth GDLs, respectively, in the in-plane direction (the direction in parallel with the electrolyte membrane). The main difference between them is that the carbon cloth GDL is more porous, less tortuous than that of the carbon paper. Because of these geometrical differences, their performance in fuel cells also varies, such as conducting liquid water and distributing reactant gases into the catalysts layers.

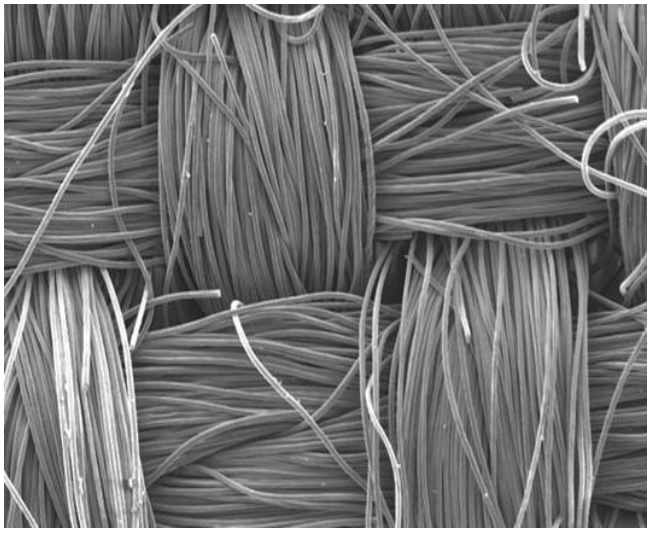

Figure1. 3. SEM image of a woven carbon cloth gas diffusion layer

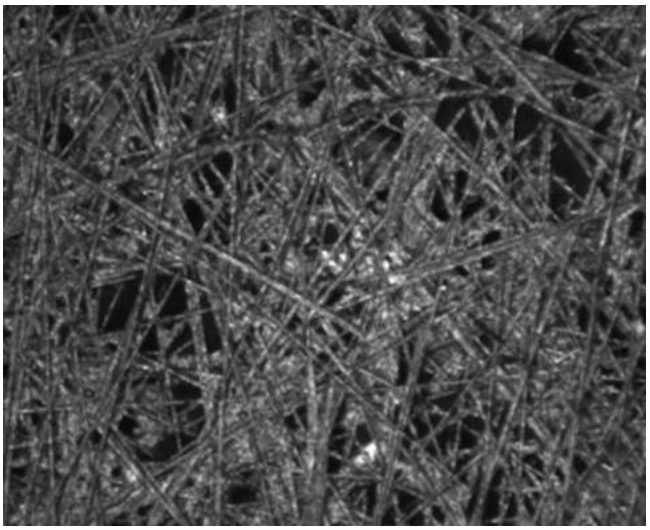

Figure1. 4. SEM image of a nonwoven carbon paper gas diffusion layer

1.4 Fuel cell modelling

At the anode, the oxidizing reaction changes one mole of hydrogen into two moles of protons. Since protons cannot stay alone and have to exist in water as ions, the oxidizing reaction at the anode produces a gas pressure drop, pointing towards the catalyst layer; such pressure drop enhances hydrogen movement. In contrast, the reducing reaction at the cathode changes one mole of oxygen into two moles of water vapour. If the water vapour cannot condense to liquid water timingly, the reducing reaction results in an increase in pressure at the cathode. Such pressure increase could reduce oxygen movement. In practice, to enhance proton movement into electrolyte membrane, water vapour is often supplied with hydrogen. In the meantime, part of the water generated at the cathode can diffuse into electrolyte membrane, facilitating proton movement. However, continuous accumulation of water inside the catalyst layer at the cathode will result in flooding, blocking the pathways for oxygen to move. This is why managing water is a critical issue in PEM fuel cells [6-8].

The performance of fuel cells is controlled by many processes. Because of the opaque nature of the fuel cell components, most flow and electrochemical processes occurring in the fuel cells are invisible. As such, fuel cell modelling has played an important role in improving our understanding of the physical and electrochemical processes. This has helped fuel cell design. Over the past two decades, a variety of models have been developed. Based on the scales each model applies to, they can be classified to macroscopic models and microscopic models.

1.4.1 Macroscopic fuel cell models

What control fuel cells performance are gas flow in the pore space and the electrochemical reactions taking place at the pore space in the catalyst layers. Because of the difficulty of visualising these pore-scale processes, mathematical modelling has been widely used in fuel cells design. The earlier fuel cell modelling used macroscopic approached in which the pore geometries are not explicitly resolved. Instead, their impact on fluid flow is described using averaged parameters, such as permeability for fluid flow, hydrodynamic dispersion for gas diffusion, and electrical resistance for electron

movement. For fluid flow, one of such approaches is based on computational fluid dynamic (CFD). In macroscopic model, gas flow in the channel are often described by the Navier-Stokes equation, and gas flow in the GDL was modelled by the Darcy's law [11-13]. Condensation of the water vapour generated at the cathode makes GDL partially saturated, which could significantly affect oxygen movement. To account for the impact of the condensed liquid water, most macroscopic models assumed that capillary force in GDL is dominant. As such, there is one-to-one relationship between capillary force and water saturation, and the flow of liquid water is driven by capillary force gradient. The simultaneous movement of gas and liquid water was described by the Darcy's law equations, which is widely used in oil industry and soil science to simulate two-phase flow. The Darcy's law for gas flow in the GDL and catalyst layer is

$$\boldsymbol{u}_g = -\frac{\boldsymbol{k}\boldsymbol{k}_{rg}}{\mu_g}\nabla \boldsymbol{p}_g \tag{1. 4}$$

where $\boldsymbol{u}_g$ is gas flux rate, k is absolute permeability of GDL or catalyst layer, k_{rg} is relative permeability of the gas, μ_g is kinematic viscosity of the gas, p_g is gas pressure, and ∇ is gradient operator. Similarly, for liquid-water flow, the Darcy's law is,

$$\boldsymbol{u}_w = -\frac{\boldsymbol{k}\boldsymbol{k}_{rw}}{\mu_w}\nabla \boldsymbol{p}_w \tag{1. 5}$$

where $\boldsymbol{u}_w$ is liquid-water flux rate, k_{rw} is relative permeability of the water, μ_w is kinematic viscosity of the water, p_g is liquid-water pressure.

The content of liquid water in the channels is limited and is often neglected in most macroscopic modelling. The gas flow in the channels is described by the following equation under the assumption that the gas is incompressible.

$$\begin{aligned} &\nabla\cdot\left(\rho_g \boldsymbol{u}_g\right) = 0 \\ &\rho_g\left(\frac{\partial \boldsymbol{u}_g}{\partial \boldsymbol{t}} + \boldsymbol{u}_g\nabla\boldsymbol{u}_g\right) = -\nabla\boldsymbol{p}_g + \mu_g\nabla\cdot\left(\nabla\boldsymbol{u}_g\right) \end{aligned} \tag{1. 6}$$

where ρ_g is the gas density.

Solving Navier-Stoke equation and the Richards's equations gives bulk velocity for both gases and liquid water, but the movement of oxygen at the cathode and hydrogen at the anode is driven not only by bulk velocity, but also by molecular diffusion. Most macroscopic models simulate hydrogen and oxygen movement using the Fick's law when only two species are considered, such as movement of water vapour and hydrogen at the anode.

$$\boldsymbol{J} = -\boldsymbol{D}\nabla\boldsymbol{c} + \boldsymbol{u}_g\boldsymbol{c} \tag{1. 7}$$

where *J* is flux rate of each species, D is diffusion coefficient, and c is the concentration of the species. For multiple species, such as oxygen, water vapour and nitrogen at cathode, the movement of each species is described by the following Maxwell-Stefan equation:

$$\nabla\boldsymbol{c}_i = \sum_{\substack{j=1 \\ j\neq i}}^{n} \frac{\boldsymbol{m}_i\boldsymbol{m}_j}{\boldsymbol{m}^2\boldsymbol{D}_{ij}}\left(\frac{\boldsymbol{J}_j}{\boldsymbol{m}_j} - \frac{\boldsymbol{J}_j}{\boldsymbol{m}_j}\right) \tag{1. 8}$$

where J_i is the flux rate species i, c_i is the concentration of species i, m_i is the molar concentration of species i, m is the total molar concentration, D_{ij} is binary diffusion coefficient between scpecies i and j, and n is the number of the species. Apart from fluid flow, the charger (proton) transport and current flow (electron flow) is also an important issue. However, since the focus of this work is fluid flow, we will restrict the review to fluid flow.

Review of the macroscopic models for a PEM fuel cell with the brief discussion were given by several researchers [14-17]. The complex equations of fluid flow and gas transport means that numerical solutions such as finite element or finite volume methods are needed. Gurau et al compared fluid flows in the fuel cells with and without considering liquid water [18], and revealed that an accumulation of water at the cathode could limit fuel cell performance. Wang and co-worker also studied the impact of liquid water using macroscopic modelling and showed similar results [14, 16]. In a recent work, Siegel et al [19] compared simulation with experimental data in the absence of liquid water, and Mazumder and Cole compared simulation and experimental results in the presence of liquid water [20].

The difficulty in macroscopic models is how to deal with the GDL and catalyst layer. For example, most macroscopic models assumed that the movement of individual species is by diffusion and the diffusion coefficients depend on only porosity. However, research in subsurface hydrology had shown that, if the transport of each species is subjected to both molecular diffusion and convection, the variation of gas velocity in the pore scale could result in hydrodynamic dispersion. Also, the averaged pore size in catalyst layers is less than one micron. As a result, the wall-gas collision could have a significant impact on gas, and the kinetic property of a gas cannot be described by a single viscosity.

1.4.2 Microscopic models

Macroscopic models provide some insight into the impact of operating conditions such as gas supply rate and the shape of the channel geometries on the fuel cells performance, but they are not problem-free. For example, the macroscopic models simulate liquid water movement using water saturation - the averaged water content in a volume. In reality, however, knowing saturation alone is insufficient to determine its impact because the fuel cell performance is controlled not only by saturation, but also by the distribution of the liquid water in the GDL. Also, the electrochemical reactions at both cathode and anode take places in the presence of catalyst coated to the surface of solid materials of the catalyst layer; that is, the accessibility of the hydrogen molecules to the catalyst is not the same. All macroscopic models, however, use a volumetric average concentration to describe the hydrogen, implying that all hydrogen molecules have equal opportunity to access the catalyst layer. The accuracy of such an approximation is an issue remained unknown.

The limitation of macroscopic models is that they use volume-averages to describe all processes, whilst in fuel cells some flow fluid and electrochemical processes occurring at pore scale, such gas-wall interface, cannot be described by the volume-averaged approaches. To bridge this gap, microscopic models (also known pore-scale model) have been developed over the last two decade to simulate pore-scale processes in attempt to help fuel cell design. Different methods have been developed, but based on the ways the pore geometries in a GDL were treated; they can be classified into pore-network models and imaging-based models.

The pore network model is an approach that idealises the pore morphology in the GDL by regular cubic lattice with spherical pores connected by cylindrical throats. The pore-scale model has been used by several researchers to investigate the distribution of liquid water in GDL [21-23], and to obtain the relationship between capillary pressure and water saturation in GDL [24]. Sinha et al [25] investigated the impact of hydrophobicity on liquid water movement in carbon paper GDL, and their results showed that with an increase in hydrophobicity, the distribution of liquid water in GDL become increasingly irregular. In another work, Gostick et al [26] investigated the relationship between capillary force and water saturation for various carbon paper GDL.

The pore network models were developed in the 1950s because of the impossibility of visualizing and quantifying the pore geometry of real porous materials. Its advantage is simplicity, and the simulated results from them can unravel some fundamental transport processes, such as liquid water distribution, which cannot be resolved in macroscopic models. However, they oversimplify the pore structure of the GDL. The advent in imaging technology over the past two decades has overcome this difficulty. For example, x-ray computed tomography has made it possible to visualize the interior structures of opaque materials at a resolution as fine as one micron. Apart from x-ray tomography, neutron imaging is also increasingly used in fuel cells to visualize liquid water movement and distribution. These, together with the development in computational physics, have made direct simulation of fluid flow in real porous materials feasible. One of such approaches is the combinations of imaging technology and lattice Boltzmann equation models. The lattice Boltzmann (LB) equation model was developed in the 1990s in attempts to overcome some drawback of the lattice gas automata for simulating single flow. It was soon found that it can also be derived from the Boltzmann equation in the kinetic theory. The intrinsic kinetic nature of the LB model makes it an ideal choice for simulating microscopic flow.

Compared to pore-network model which idealised the porous morphology of GDL, imaging-based model can simulate fluid flow and mass transport through the real void space in the GDL[27]. The 3D GDL can be either acquired by X-ray computed tomography or by numerical generations. There have been several studies that used LBM model and images obtained from X-ray computed tomography or statistical generation to investigate the transport processes in GDL [23, 28-33]. For example, Mukherjee et al [31]

investigated the effects of porous structures on liquid water transport process. Hao and Cheng [32] explored the effect of GDL wettability on liquid water transport and distribution. Besides, the anisotropic permeability of the GDL images acquired using x-ray tomography was also numerically predicted. Other applications of the microscopic models include multiple gaseous species transport (hydrogen, oxygen and water vapour) [34, 35] and two-phase flow (gas and liquid water) [36, 37].

The microscopic models can simulate detailed fluid flow or electrochemical reactions at micro- to nano-scale, but they cannot be used to simulate the whole cells because of their demand on computational power. Currently, the use of the microscopic models is limited to unravel some processes which cannot be resolved by macroscopic models; the results from the microscopic models can help us to improve macroscopic modelling.

1.5 The objectives

There has been increasing recognition that understanding the pore-scale processes in both GDL and catalyst layers will play an important in improving fuel cell design. The main objective of this work is to use a combination of x-ray computed tomography and numerical modelling to simulate gas flow in GDL and CL with a view to help fuel cell design so as to improve PEMFC efficiency. Both woven and non-woven GDLs with contrasting porous morphology will be used in this research. GDL with averaged pore size greater than 10 μm will be acquired using the x-ray micro-computed tomography at resolutions from 970 nano-metres to 2.0 microns. I will then develop and compare two lattice Boltzmann models for simulating single-phase flow, one is the single-relaxation lattice Boltzmann model, and the other one is the multiple-relaxation lattice Boltzmann model. To test the models, simulated pore-scale velocity in the GDLs was used to calculate their permeability; the simulated permeability is then compared with experiments.

Practical application needs to pack a number of cells into a stack. This will result a compression, with the GDL in the regions between channel ribs and proton exchange membrane subjected to higher compressive pressure than in other regions. To investigate how the compression affects gas flow and hence fuel cells performance, methods will be developed to x-ray image the GDL under different compressive pressure unto 20 KPa.

The reduction of the GDL permeability due to compression in both the in-plane and through-plane directions will be calculated.

Gas flow in catalyst layer is important as it is the place where the electrochemical reactions take place. But it is challenging because the size of the pores is less than one micron and gas flow in the catalyst layer is no longer continuum. As a result, the wall-gas collision must be re-considered, meaning that in the macroscopic models, the absolute permeability of the catalyst layer for different gases varies. To investigate this, we will simplify the pore geometry in catalyst layer into a bundle of tubes whose diameters can be derived from the pore-size distribution of the 3D FIB images.

1.6 Outline of the thesis

This thesis consists of eight chapters.

Chapter 1 introduced the background of the polymer electrolyte fuel cell, reviewed the models that have been developed for fuel cell simulations.

Chapter 2 introduces the x-ray micro CT and nano-CT imaging that was used to obtain the 3D images of the GDLs; it also explains how gray-scale 3D X-ray images are digitized to get the binary structure of GDLs.

Chapter 3 will introduce the lattice Boltzmann numerical modelling, including its development and boundary treatment; it will cover both single-relaxation time (BGK) lattice Boltzmann model and multiple-relaxation time (MRT) lattice Boltzmann model.

Chapter 4 compares the performance of BGK and MRT lattice Boltzmann models for simulating single-phase flow in both carbon paper GDL and a column of glass beads.

Chapter 5 shows the impact of compression on the permeability of GDL using both BGK and MRT lattice Boltzmann model. In particular, we investigate if the BGK model can give reasonable results by carefully choosing the relaxation-time parameter, and if such relaxation-time is independent of media structure and media porosity.

Chapter 6 describes the combination of X-ray image and two-phase MRT model for simulating liquid water intrusion into GDLs.

Chapter 7 presents the mode for simulating gas flow in the catalyst layer by simplifying the pore geometry into a bundle of tubes with different diameters. A lattice Boltzmann model will be developed to simulate gas flow in each tube when the Knudsen number cannot be neglected.

Chapter 8 concludes the project with discussion on the results and view for future work.

Chapter 2 X-ray Computed tomography

X-ray imaging has been used in medicine for several decades. The X-ray computed tomography (CT) was developed based x-ray imaging. The earlier use of the x-ray CT was limited to medicine after it was first invented. Over the past two decades, however, the prices of X-ray CT have come down, and it has been increasingly used in wide range of areas, including in fuel cells.

2.1 The principle of x-ray computed tomography

The theory of the x-ray imaging is that when an x-ray passes through a subject, it reacts with the electrons in what were known as photoelectric effect and Compton effects. Such effects reduce the intensity of the x-ray when it passes through an object.

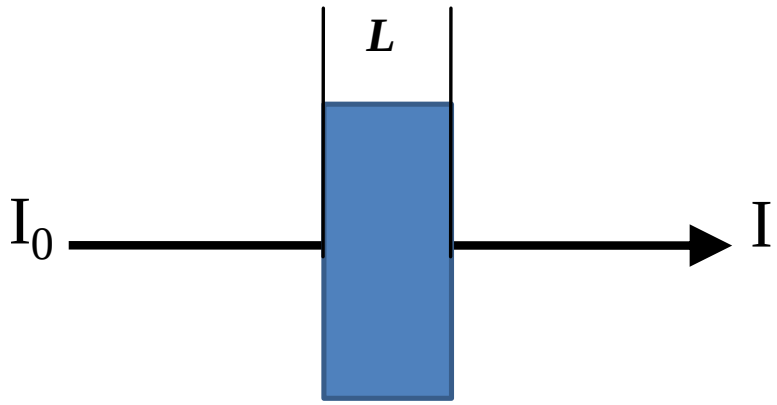

Figure 2. 1 Attenuation of x-ray when it passes through an object

As shown in Figure 2.1, if the intensity of an x-ray beam is I_0, after it passes through an object thick L, the intensity of the x-ray beam will be reduced to

$$I = I_0 \exp(-Lu) \tag{2. 1}$$

where u is a parameter that is characterised by the object. Similarly, when the x-ray passes though a pack of different objects characterised by different u_i as shown in Figure 2.2, its intensity reduces to

$$I = I_0 \exp\left(-\sum_{i=1}^{n} L_i u_i \right) \quad (2.\ 2)$$

where L_i is the thickness of *ith* object and u_i is the associated parameters. Rewriting above equation into the following form

$$p = -\ln\left(I / I_0\right) = \sum_{i=1}^{n} L_i u_i \quad (2.\ 3)$$

p in which is called attenuation coefficient, and n is the number of the objects.

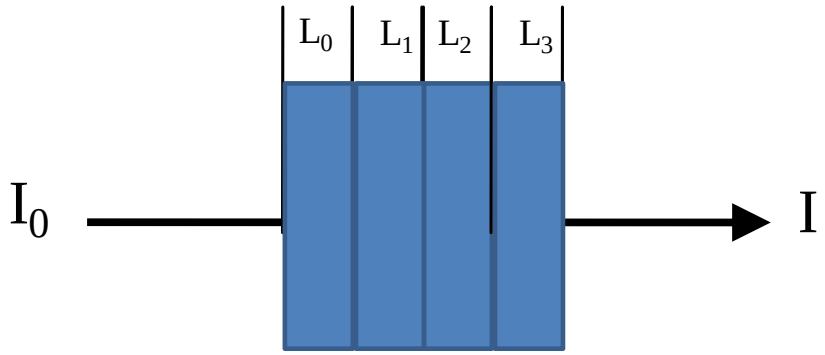

Figure 2. 2 Attenuation of x-ray when it passes though a pack of the objects.

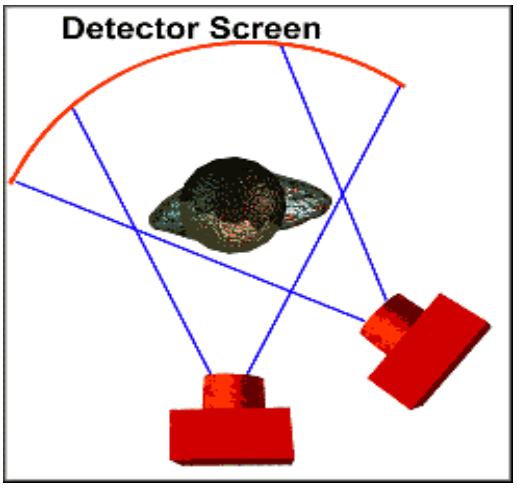

Figure 2. 3 Schematic illustration of acquiring a 2D section using x-ray CT.

If a 2D section comprises of n objects as shown Figure 2.3, scanning the section using x-ray beams from different direction can get a series of attenuation coefficients p_i, which is the function of u_i. Solving p_i can get the distribution of u_i and hence the 2D structure of the section.

Figure 2.4 shows a typical x-ray computed tomography. It consists of an x-ray source, a sampler holder and a detector to measure the x-ray density. The sample holder can rotate and move up and down. The x-ray emitted from the x-ray source is recorded by the detector after it passes through the sample; the sample is then rotated 0.5 or 1 degree to repeat the above procedure until the sample is rotated 360^0. Analysing the recorder x-ray attenuation can get one 2D slice of the sample. The sample is then either moved up or down; the repeating the above procedure can get another 2D slice. Stacking these 2D slices yield a 3D structure of the sample [2, 38-41].

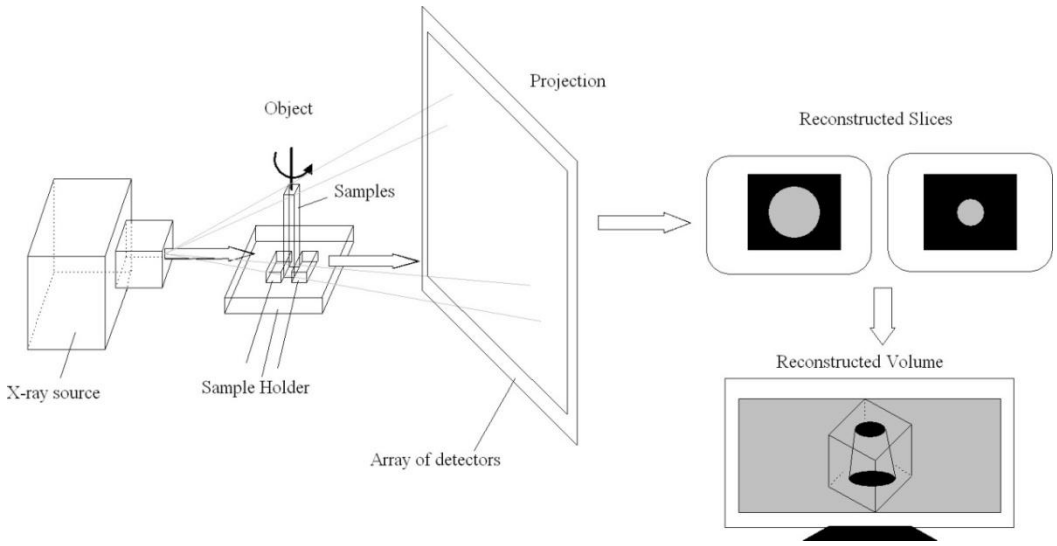

Figure 2. 4 Principle of the micro- tomography system

Figure 2.5 shows a 2D section and a 3D structure of porous medium acquired using x-ray tomography.

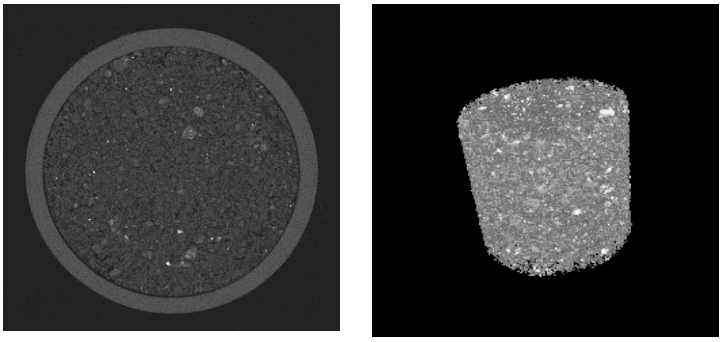

Figure 2.5 The 2D gray-scale slice and the stack of 2D slices that make a 3D structure

In this work, both x-ray micro CT and nano CT were used to reconstruct GDL and CL under different resolution. The 2D slice acquired from the x-ray CT is a grey-scale image with each pixel in it representing by a number from 0 to 255. The slices are then assembled to reconstruct a 3D image [42]. X-ray images can be generated using high resolution micro CT with 2-5 μm resolution or nano CT with 20-50 nm resolution through desktop or synchrotron scanners. Synchrotron scanners provide parallel X-ray beams and therefore result in higher resolution and better image contrasts [43], while in desktop tomography, X-ray sources are not able to generate parallel beams. Instead, they use a point source which produces a small angle cone X-ray beam in the object area as shown in Figure 2.4. In this work, desktop tomography was used.

2.1.1 Image acquisition

The principle of the desktop X-ray μCT (SkyScan 1072, SkyScan Ltd. Belgium) and X-ray nCT (SkyScan 2011, SkyScan Ltd., Belgium) is shown in Figure 2.4. A sample is placed in front of an X-ray source and then rotated step-by-step. Grey scale projections are then generated using an X-ray detector array. SkyScan 1072 system is equipped with an X-ray source of 100 kV (max) and 100 μA (max) and a minimum rotation step of 0.23 degree, resulting in a maximum pixel size of 1.76 μm. The SkyScan 2011 uses an X-ray source of 80 kV (max) and 200 μA (max) and a rotation step of 0.23 deg which gives a maximum pixel size of 200 nm. Although increasing the rotation steps would increase the accuracy of reconstruction, the cost of computational time will be very expensive. Also, increasing the X-ray energy by current would result in a better image contrast, and therefore the images could be taken at the maximum current. However, increasing the X-ray voltage causes X-ray over-transmission, meaning that the projections become over-bright, especially when the X-ray passes through soft materials. Therefore, parameters recommended by many researchers and the machine manufacturer are: X-ray low voltage of 40-50 kV at 100 μA with rotation step of 0.9 degree for the μCT and 25-40 kV at 200 μA with rotation step of 0.5 deg for the nCT systems [44, 45].

The X-ray detector used for both devices is a Hamamatsu X-ray camera, which contains a scintillator and a charge coupled CCD chip. The X-rays are converted to flashes of light by a scintillator screen (gadolinium oxide). The size of CCD chip is smaller than that of the scintillator and can be damaged by long exposure to X-rays. To lessen potential damage, a tapered fibre-optic bundle is used, which is glued to the scintillator screen at one end and the CCD chip at the other. The bundle maintains an exact 1:1 translation of the position from the scintillator to the CCD chip. The camera employed in the SkyScan system has a 1024×1024 pixels CCD chip with a 12 bit depth. The minimum pixel size of a system is defined by the object diameter of the camera and the number of pixels across it. For instance, in the SkyScan 1072, the object diameter is approximately 1.8 mm. The maximum pixel size is 1.8 mm divided by 1024 pixels, which gives a resolution of 1.76 μm.

The 2D gray scale shadow images are then used to reconstruct 2D cross-sectional image slices, which correspond to what would be seen if the sample is cut through the scanning plane. The slice reconstruction is based on the back projection method to be discussed in the next section.

2.1.2 Back projection and 2D slice reconstruction

The X-ray computed tomography is a technique closely related to the X-ray radiation. With the technique, the inner structure of an three-dimensional object can be reconstructed from the two- dimensional projections [43]. An important property of the back projection operation in parallel beam projections is the shift invariance of the image object along the x-ray projection directions. Therefore, all the back projection lines are equivalent. Thus, an equal weight should be assigned to each of the back projection lines during the back projection operation. The measured projection data are back projected into two-dimensional data arrays such that the dimensional mismatch between the image object and its corresponding measured data disappears after the back-projection operation. An empty array of pixels corresponding to all possible object displacement can be initialized in the computer memory. Since the position of the projection from the adsorption points are known, one can mark all possible positions of the absorption points as lines in the computer memory [46-48].

In each rotation step, the lines of possible positions of the point will be added to the area of reconstruction. After many rotation steps, the position of the adsorption point in the reconstructed are will be localized.

By the back projection method, thin grey scale slices of the sample correspond to what would be seen if the sample was cut through the scanning plane, were produced. The thickness of each slice is equal to the pixel size of the projections, e.g., in an image with 1.76 μm pixel size in the projection images, the thickness of a slice is 1.76 μm.

2.1.3 Digital 3D reconstruction

The 3D reconstruction is a standard process and the 3D image could be achieved either in grey scale or binary image by assembling the 2D slices together. However, a binary 3D reconstruction process based on binary slices is much less time consuming than grey scale image processing. Therefore, in this work we only use the 3D binary images. There are

two well-known algorithms that can be employed to carry this out: 'marching cubes ' and 'double time cubes'. 'Marching cubes', which was developed by Lorensen and Cline [49], is a surface building process based upon an explicit hexahedral voxel model. 'Double time cubes' is smoother as the number of facet triangles is half the number of the 'marching cubes' method and is developed by Bouvier [50]. The SkyScan reconstruction software, namely, CTAN, uses the 'double time cubes' method.

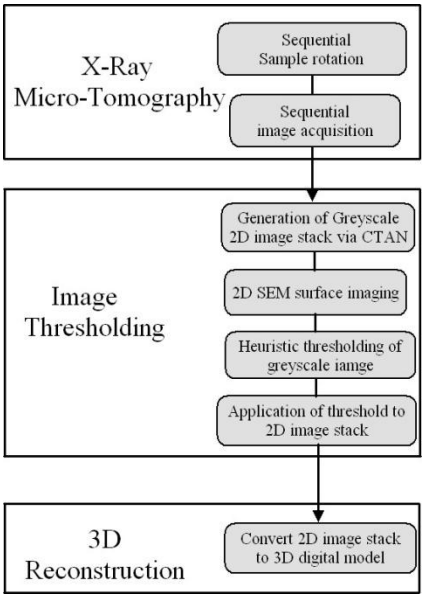

Figure 2.6 Principal procedure of generating binary 3D structure

As previously discussed, for pore analysis and 3D reconstruction, representative binary slices are required. Therefore, it is necessary to threshold the greyscale slices acquired from X-ray tomography in order to produce binary images [51-53]. For a general binary image, structural and transport parameters including porosity, surface area, pore size distribution, porosity, characteristic lengths, structural degree of anisotropy, permeability, tortuosity and effective diffusivity could be obtained through 3D digital images. The principal of X-ray micro-tomography process is shown in Figure 2.6.

2.2 Threshold method for non-woven GDL images

This section describes the method for fine-tuning the threshold of tomography images for a non-woven GDL. First, the influence of small threshold variations on determining the properties of the GDL is discussed. Then porosity and average fibre diameter of the GDL, obtained from a series of threshold X-ray images, were compared to reference values of porosity and average fibre diameter achieved from a density experiment and SEM images,

respectively. Among a number of the images obtained by different thresholds, the optimal threshold was chosen, in which the porosity and average fibre diameter of the resultant digital model are closest to the reference values.

In this work, a $1\times1\times0.3\ mm^3$ carbon paper GDL HP_30_35 sample supplied by Technical Fibre Products is scanned using an X-ray source of SkyScan 2011 with 25 kV, 200 μA without filter, 2 sec exposure time, 3 frames in average and a rotation step of 0.5 degrees. 371 shadow images with 680 nm pixel size are acquired within 40 minutes. The shadow images are then processed using modified Feldkamp filtered back projection method to reconstruct the 2D greyscale slices. Figure 2.7 shows the 3D images

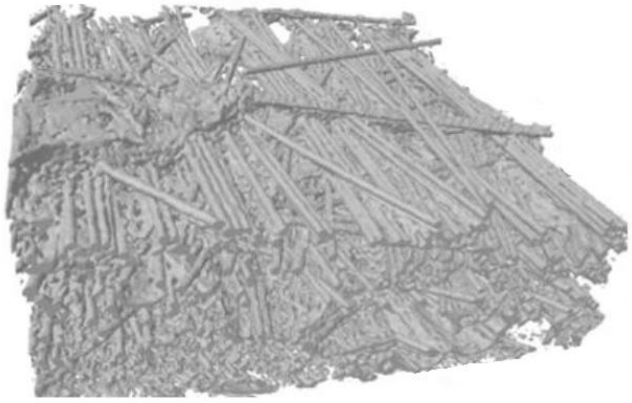

Figure 2. 7 The reconstructed image of a carbon paper GDL

2.3 Threshold method for woven GDL images

To understand the effect of threshold variation on the properties of reconstructed porous woven material, GDL samples with 5-10 μm filament size have been scanned in SkyScan 1072 with pixel size of 1.76 μm. A Carbon cloth GDL SCCG-5N sample was scanned using an X-ray source of SkyScan 1072 with 50KV, 100 μA without filter, 2 sec exposure time, 3 frames in average and a rotation step of 0.9 degrees. 207 shadow images with 1.76 μm pixel size were acquired within 55 minutes. The 2D greyscale image slices were produced in 256 grey scales and using Otsu's thresholding algorithm to chose 2D slice. Then, the set of 2D greyscale slices were threshold again in 12 grey levels with a step of 0.4% variation around the starting point. For investigation of threshold variation, the 5%

threshold towards the higher threshold was applied [54]. During modelling, two parameters need to be identified: (1) average fibre diameter and (2) continuity of the fibres. The high resolution binary SEM image of a particular feature was used to compare the average fibre diameter and continuity. Figure 2.8 shows 3D structure of the woven GDL.

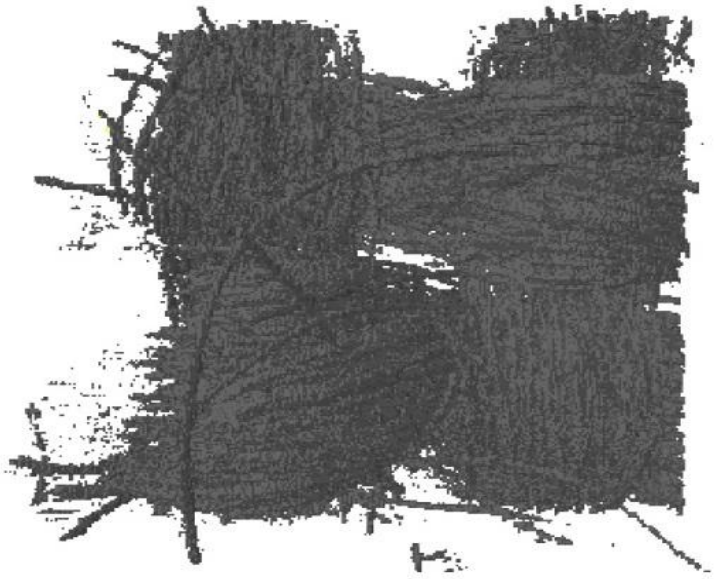

Figure 2. 8 The reconstructed image of carbon cloth GDL

2.4 From binary image to fluid flow simulation

It has been proven that when a study is carried out using X-ray micro CT/nano CT data for porous non-woven GDL, the key structural parameters are affected by small variations in threshold. It is found that a variation of more than 5% in threshold makes a significant visual difference to the resultant binary images. While a variation of less than 5% is difficult to be recognized visually, it can have a significant effect on the overall structural properties of 3D binary image. Therefore, having some easily measurable references will greatly assist in finely tuning the threshold for the 3D binary representative image. Reference values were considered to be porosity and average fibre diameter which can be achieved from density experiments and SEM images respectively. Therefore, between the threshold images, the optimal threshold was chosen in which the porosity and average fibre diameter of the resultant digital model are closest to the reference values.

For the woven GDL, a small range of 5% in threshold variation shows in influence of about 10% in fibres size. In order to overcome such modelling problems two parameters

have been identified: average fibre diameter; continuity of the fibres. A high resolution binary SEM image of a particular feature was used to compare the average fibre diameter and continuity. Then by using the 3D reconstructed surface from micro CT and comparing the continuity and average fibre diameter with the SEM image, finely tuned threshold value was found. This method is relatively fast and more trustable, rather than the common visual threshold tuning or Otsu's algorithm without any pre-knowledge in the micro/nanostructure. The carbon cloth employed in this study has a nominal thickness of 377 μm under a compression of 11.37 Kpa , warp-weft of approximately 24 threads /cm and a density of 316 kg/m^3. The material does not contain a micro-porous layer (MPL).

The 3D digital image is then used directly with the LB model without further modification to simulate flow through its heterogeneous porous structure.

Chapter 3 Lattice Boltzmann model for single-phase flow

3.1 Introduction

The lattice Boltzmann (LB) method was originally developed as an improvement to the lattice gas (LG) method [55] for simulating incompressible in the l990s. Since then it has been applied in many areas to simulate various fluid and transport phenomena. Recent reviews on the LB method and its application in different areas were given in [27, 56-58]. LB method is appealing because of its simplicity and flexibility. It was believed that it has the potential to overcome some of the problems encountered by the conventional continuum-based CFD methods, such as dealing with complex geometrical boundary conditions and microscopic forces.

The LB model have three components: evolution equation that controls the ways the particle distribution functions colloid and move from one place to another, a spatial lattice in which the particle distribution function move, and a local equilibrium distribution function that decides what flow processes that the lattice Boltzmann models simulate. These three main components and other related issues are described in this chapter.

Fluid motion can be described at different scales based on the ratio between the mean free path of the fluid molecules and a representative physical length scale in which the fluid flows. The mean free path is the length that a molecule travels before experimenting collision with other molecules. The physical scale is a length that characterizes the size of the system. This ratio is also known as the Knudsen number in kinetic theory.

If the Knudsen number is sufficiently large, the fluid can be assumed to be continuous where the fluid motion can be described using macroscopic variables such as bulk velocity and density. If the Knudsen number is small, the fluid cannot be treated as a continuous medium, and alternative approaches must be sought to simulate its movement.

The size of pores in porous media could vary in several orders of magnitudes. In some small pores the Knudsen number are small and fluid flow in them cannot be described by the continuous approach. Also, in practical application, the individual pores are not explicitly resolved, and the whole pore media are treated as continuum media. Hence,

based on the scales that a model deals with, one can classified them into three scales: microscopic scale, mesoscopic scale and macroscopic scale.

Microscopic scale: At microscopic level, the interaction between fluid elements requires the description of each fluid particle based on the classical Newton's law of motion and the influence of microscopic forces. Such flow is often simulated using the molecular dynamic models.

Mesoscopic scale: Between the microscopic and macroscopic scale is mesoscopic scale. At this scale, the behaviour of individual molecules is replaced by the average behaviour of a number of particles from which the statistical mechanics description emerges. The mesoscopic method is based on statistical mechanics. For porous media, the flow at this scale is represented as a network of micro-pores traversed by the fluid flow.

Macroscopic scale: At the macroscopic level, the individual fluid particles are replaced by continuum fluid elements where the principles of mass, momentum, and energy conversation are applied to a representative volume element (REV). This approach leads to the fundamental partial differential equations for fluid motion, and the differential equations can be solved by numerical methods, such as finite difference method (FDM), finite volume method (FVM), or finite element method (FEM). At the macroscopic scale or above, the internal structure of the porous media is ignored and all microscopic and mesoscopic processes are averaged out, and the impact of the pore geometry is described by bulk parameters such as permeability for fluid flow, hydrodynamic dispersion coefficient for gas diffusion, water content for liquid water flow. Scales above macroscopic scale are usually described by a heterogeneous assembly of macroscopic units, with locally varying transport properties.

For fluid flow, the widely used macroscopic equation to describe fluid movement is the Darcy's law, which can be described as follows

$$Q = \frac{k}{u}\nabla P \tag{3. 1}$$

where Q is the flow rate across a unit area within a unit time, driven by the pressure gradient $\nabla \boldsymbol{P}$, μ is the dynamic viscosity of the fluid, and k is absolute permeability of the medium.

The LB model can be applied to simulate fluid flow at all above the scales, but the main research reported in the literature focused on mesoscopic scale, that is, the flow phenomena through the pore geometry. Figure 3.1 shows the relationship between the lattice Boltzmann model and the processes at the three scales.

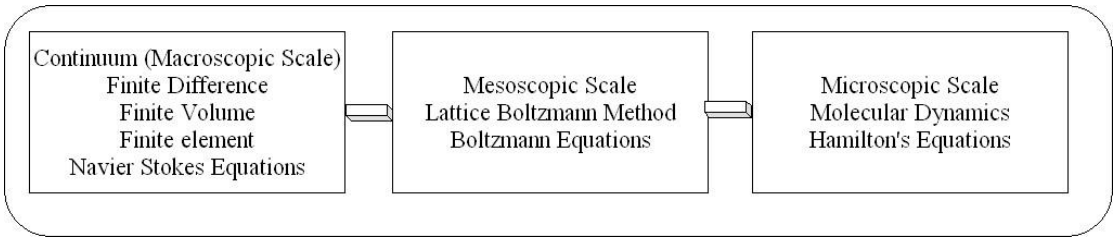

Figure 3.1 Relation between modelling at the three scales

Most work on fluid flow in GDLs were based on macroscopic models by volumetrically averaging the conservation equations of gas flow over an representative elementary volume (REV), losing the detailed processes occurring at pores scale [59-62]. In fuel cells, the electrochemical reactions occur only in the presence of the catalysts that are coated at gas-solid interface. The volume-average approach may not be able to accurately describe such surface-based reactions. Therefore, understanding the pore-scale processes is especially important for improving fuel cell performance. Recently, there has been an increase in the use of lattice Boltzmann method to simulate various pore-scale transport processes in GDLs [29, 63].

The earliest version of the lattice Boltzmann equation (LBE) model was proposed by McNamara and Zanetti [64] in an attempt to eliminate the noise of the lattice gas automata. In their work, the Boolean particles in the LGA were replaced by a floating point variable, which changes from 0 and 1.

The three components of the LBE model are the lattice, evolution equation, and the equilibrium distribution function. The lattice is the discretization of the space through which fluid moves; the evolution equation controls how the fluid particles react with each other and move in the space; the equilibrium particle distribution functions describe the equilibrium state at which the fluid distribution functions will reach once reaching steady state; depends on the system to be simulated.

Two commonly used LB methods for pore-scale simulation of fluid flow in porous media is the single-relaxation time LB model [65], and the multiple-relaxation time (MRT) LB model [66]. The MRT lattice Boltzmann model provides more stable solution as it uses different relaxation time to relax different entities, but increases the computational costs. Pan et al. [67] compared the MRT lattice Boltzmann model and single-relaxation lattice Boltzmann model, and concluded that the later model gives rise to a permeability that increases with the value of the relaxation time. This is due to that the location of the fluid-solid boundary recovered by the bounce-back method for solving the non-slip boundary depends on the relaxation time in the single-relaxation time model [68]. However, it was proven by He et al. [69] that when the relaxation time is unity, the bounce-back method can accurately locate the fluid-solid boundary, hence give accurate results as demonstrated in previous work by our group and others [70, 71]. Since the viscosity in LB models depends not only on the relaxation time but also on the time step and size of the cubic voxels, by fixing the relaxation to be unity, the viscosity of any fluids can be recovered by adjusting the value of the time step. Thus it is misleading to state the single-relaxation time LB model gives rise to viscosity-dependant permeability [67] .

We will examine the accuracy of the two LB models by comparing the permeability calculated by them with experimental measurement for a pack of glass beads, and then apply them to simulate gas flow in the GDLs with different porosities. The relationship between the anisotropic permeability and the porosity for both media will then be investigated.

3.2 The Lattice

For simulating fluid flow that recovers the Navier-Stokes equation at macroscopic scale, the lattice must have enough symmetry [55]. In the literature, several lattices have been developed. Based on the dimension and the number of directions that the fluid particles move, the commonly used lattices can be described by $D_X Q_Y$, where X indicates the dimensions, and Y is the number of directions along which the fluid particles move [72]. For example, D3Q19 means a 3D lattice in which the fluid particles move in 19 directions with 19 velocities. In what follows, we assume that δx is the side length of a single lattice, and δt is a time step. In the LBE lattice, the space is discretisized into a number of cubes in 3D, and squares in 2D; the fluid particles can move into one of its adjacent neighbouring lattice during the period of one time step [55].

In two dimensions, the space over which the fluid flow is discretisized into a number of squares [73]. The fluid particles in one square can only move into one of its nine neighbouring squares during one time step. Apart from square lattice, hexagonal lattice was also used, but hexagonal lattice has become less common over the past two decades [55]. Figure 3.2 shows the D2Q9 lattice model, where the circles represent the centre of the lattice, and the fluid particle moves in nine directions with nine velocities. Assuming that both lattice unit and the time step are unit, the nine normalised velocities c_i are shown in the Table 3.1, in which f_i is the particle distribution function moving with the ith velocity.

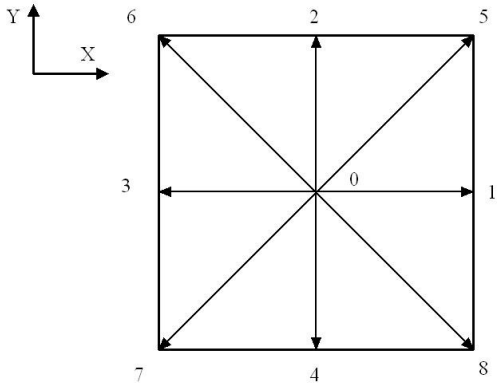

Figure 3.2 The 9-velocity lattice pattern

Table 3.1 The nine attice velocities in D2Q9

	f_0	f_1	f_2	f_3	f_4	f_5	f_6	f_7	f_8
c_{ix}	0	1	0	-1	0	1	-1	-1	1
c_{iy}	0	0	1	0	-1	1	1	-1	-1

For 3D flow, there are several cubic lattice models, and the commonly used are D3Q15, D3Q19 and D3Q27 [74]. All the three lattice models can recover the Navier-Stokes equations at macroscopic scale. Since D3Q15 and D3Q19 lattice models are more efficient, they are often used in the literature. Figure 3.3 and 3.4 shows the D3Q15 and D3Q19 lattice models, respectively.

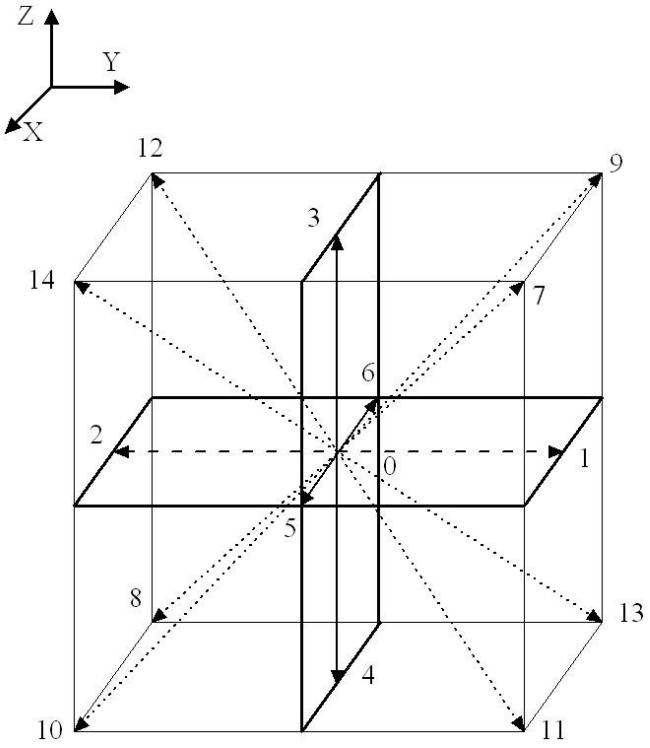

Figure 3.3 The 15-velocity lattice pattern in 3D

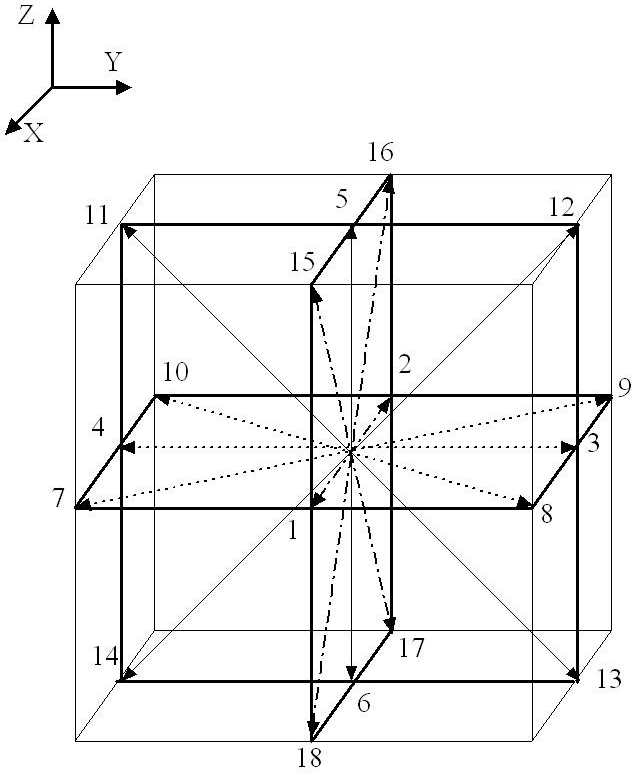

Figure 3.4 The 19-velocity lattice pattern in 3D

For simulating fluid flow through the pore geometry in a porous medium, D3Q19 is more convenient and was thus used in this research. For each velocity, a particle distribution

function f_i is defined for it. Therefore, in the D3Q19 model, there are 19 particle distribution functions, including a resting particle distribution function that moves with zero velocity, f_0. The other particle distribution functions are: seven moving at speed of 1 ($f_2, f_3, f_4, \ldots f_7$), and the remaining moving with speed $\sqrt{2}$ ($f_8, f_9, f_{10}, \ldots f_{18}$) as shown in Figure 3.4. The value of each lattice velocity c_i is shown in Table 3.2, in which both lattice unit and time step are assumed to be unity.

Table 3.2 The 19 lattice velocities in the D3Q19 model

	f_0	f_1	f_2	f_3	f_4	f_5	f_6	f_7	f_8	f_9	f_{10}	f_{11}	f_{12}	f_{13}	f_{14}	f_{15}	f_{16}	f_{17}	f_{18}
c_{ix}	0	1	-1	0	0	0	0	1	-1	1	-1	1	-1	1	-1	0	0	0	0
c_{iy}	0	0	0	1	-1	0	0	1	-1	-1	1	0	0	0	0	1	-1	1	-1
c_{iz}	0	0	0	0	0	1	-1	0	0	0	0	1	-1	-1	1	1	-1	-1	1

At each lattice, the macroscopic fluid density and momentum can be calculated by summing up the associated momentums of all the particle distribution functions. For example, fluid density from zero moment and bulk velocity from first-order moments as follows:

$$\rho(x,t) = \sum_{i=0}^{18} f_i(x,t) \tag{3. 2}$$

$$\rho(x,t)u(x,t) = \sum_{i=0}^{18} c_i f_i(x,t) \tag{3. 3}$$

where ρ is density and $u(x,t)$ the bulk averaged velocity of all the particles at time t and at the lattice centred at x.

3.3 The Evolution Equation

In discrete form, the lattice Boltzmann equation describes the evolution of the fluid particle distribution function as follows:

$$f\left(x+v\delta_t,v,t+\delta_t\right)-f\left(x,v,t\right)=-\frac{1}{\tau}\left(f\left(x,v,t\right)-f^{M}\left(x,v,t\right)\right) \tag{3. 4}$$

which is equivalent to

$$f\left(x+v\delta_t,v,t+\delta_t\right)=(1-\frac{1}{\tau})\left(f\left(x,v,t\right)+\frac{1}{\tau}f^{M}\left(x,v,t\right)\right) \tag{3. 5}$$

where $\tau=1/\omega\delta_t$ is a dimensionless parameter, and is also known as the relaxation time. Applying this equation to all fluid particle distribution functions gives the following equation:

$$f_i\left(x+c_i\delta t,t+\delta t\right)=\left(1-\frac{1}{\tau}\right)f_i\left(x,t\right)+\frac{1}{\tau}f_i^{eq}\left(x,t\right) \tag{3. 6}$$

where

$$f_i^{eq}\left(x,t\right)=f^{eq}\left(x,c_i,t\right)$$

The evolution of the fluid particles consists of two steps: (1) the streaming step in which a particle moves from one node to one of its nearest neighbouring node with one of the 19 lattice velocities, (2) the collision step in which the particles at the same lattice collide with each other and then change their masses. Depending on the fluid phenomena to be simulated, different collisions can be constructed. For simulating fluid flow, the collisions need to conserve mass, momentum and energy.

3.4 The Equilibrium Equation

In kinetic theory, the equilibrium function is the Fermi-Dirac distribution, which is often expanded as a Taylor series as a function of macroscopic velocity in terms up to its second order [75]. In the lattice Boltzmann method, for recovering the Navier-Stokes equations, applying the Taylor expansion to the Maxwell Boltzmann distribution gives the equilibrium distribution functions. The local equilibrium distribution function has the following form:

$$f^M(x,v,t)=\frac{\rho}{(2\pi RT)^{D/2}}e^{-\frac{v^2}{2RT}}\left(1+\frac{v\cdot u}{RT}+\frac{(v\cdot u)^2}{2(RT)^2}-\frac{u^2}{2RT}\right) \tag{3. 7}$$

where R is the gas constant, and T is absolute temperature. Applying this to the D3Q19 model gives [76], in which f_i^{eq} is given by the following equation .

$$f_i^{eq}(x,t)=\rho W_i\left(1+c_i\cdot\frac{u}{RT}+\frac{(c_i\cdot u)^2}{2(RT)^2}-\frac{u^2}{2RT}\right) \tag{3. 8}$$

where W_i is weighting coefficient. For simulating fluid flow, the equilibrium distribution functions need to satisfy:

$$\sum_i f_i^{eq}(x,t)=\int f^M(x,v,t)dv=\rho \tag{3. 9}$$

$$\sum_i c_{ia}c_{i\beta}f_i^{eq}(x,t)=\int v_a v_\beta f^M(x,v,t)dv=\rho RT\delta_{a\beta} \tag{3. 10}$$

$$\sum_i c_{ia}c_{i\beta}c_{i\gamma}c_{i\delta}f_i^{eq}(x,t)=\int v_a v_\beta v_\gamma v_\delta f^M(x,v,t)dv \tag{3. 11}$$

$$\sum_i c_{ia}c_{i\beta}c_{i\gamma}c_{i\delta}f_i^{eq}(x,t)=\rho(RT)^2\left(\delta_{a\beta}\delta_{\gamma\delta}+\delta_{a\gamma}\delta_{\beta\delta}+\delta_{a\delta}\delta_{\beta\gamma}\right) \tag{3. 12}$$

Using the lattice velocities c_i in the D3Q19, the parameters W_i can be obtained in such a way that equations 3.9 -3.11 are satisfied and the symmetry of the lattice is maintained. That is,

$$\sum_{i=0}^{18}W_i=W_0+6W_1+12W_2=1 \tag{3. 13}$$

$$\sum_{i=0}^{18}c_{ia}^2W_i=2W_1+8W_2=RT \tag{3. 14}$$

$$\sum_{i=0}^{18}c_{ia}^4W_i=2W_1+8W_2=3(RT)^2 \tag{3. 15}$$

$$\sum_{i=0}^{18}c_{ia}^2c_{i\beta}^2W_i=4W_2=(RT)^2 \tag{3. 16}$$

This gives,

$$f_0^{eq}(x,t) = \rho W_0\left(1-\frac{3}{2}\frac{u^2}{c^2}\right) \tag{3. 17}$$

$$f_i^{eq}(x,t) = \rho W_i\left(1+3\frac{c_i\cdot u}{c^2}+\frac{9}{2}\frac{(c_i\cdot u)^2}{c^4}-\frac{3}{2}\frac{u^2}{c^2}\right) \tag{3. 18}$$

where

$$\begin{aligned} &W_0 = 1/3 \\ &W_a = 1/18 \quad for \quad a = 1,...6 \\ &W_a = 1/36 \quad for \quad a = 7,...18 \end{aligned} \tag{3. 19}$$

$$c^2 = 3RT \tag{3. 20}$$

$$RT = \frac{1}{3} \tag{3. 21}$$

3.5 Single relaxation time lattice Boltzmann model

The earlier lattice Boltzmann model is based on the Bhatnagar-Gross-Krook (LBGK) approach, also known as single relaxation lattice Boltzmann model, which uses a single relaxation time parameter to describe the collision between particles [77]. The single relaxation time lattice Boltzmann model can be described as follows:

$$f_i(x+e_i,t+1) - f_i(x,t) = -\frac{1}{\tau}\left(f_i(x,t) - f_i^{eq}(x,t)\right) \tag{3. 22}$$

where $f_a(\boldsymbol{x}_i,t)$ is particle distribution function at time t and location x_i, $f_a^{eq}(\boldsymbol{x}_i,t)$ is the equilibrium distribution function, τ is dimensionless relaxation time, Δt is time step. For the D3Q19 model, the lattice velocity c_a is given as follows:

$$\boldsymbol{c}_a = \begin{cases} (0,0,0) & a = 0 \\ (\pm1,0,0)c/\Delta t, (0,\pm1,0)c/\Delta t, (0,0,\pm1)c/\Delta t & a = 1,...,6 \\ (\pm1,\pm1,0)c/\Delta t, (\pm1,0,\pm1)c/\Delta t, (0,\pm1,\pm1)c/\Delta t & a = 7,...,18 \end{cases} \tag{3. 23}$$

where c is the side length of the cubic lattice. The equilibrium distribution function for D3Q19 model is given by

$$\begin{aligned} f_a^{eq} &= \omega_a \rho \left[1 - \frac{3}{2}\frac{u^2}{c_s^2} \right] \quad a = 0 \\ f_a^{eq} &= \omega_a \rho \left[1 + 3\frac{c_a \cdot u}{c_s^2} + \frac{9}{2}\frac{(c_a \cdot u)^2}{c_s^4} - \frac{3}{2}\frac{u^2}{c_s^2} \right] \quad a = 1,...,18 \end{aligned} \tag{3. 24}$$

where $c_s = \sqrt{1/3}c/\Delta t$ is sound speed, and $w_0 = 1/3$, $w_{1\sim6} = 1/18$, $w_{7\sim18} = 1/36$. The bulk fluid density ρ and velocity $\boldsymbol{u}$ are calculated from the distribution functions as follows :

$$\begin{aligned} \rho &= \sum_{a=0}^{18} f_a \\ \rho \mathrm{u} &= \sum_{a=0}^{18} f_a c_a \end{aligned} \tag{3. 25}$$

The above model simulates fluid flow with the kinematic viscosity given by $\mu = (\tau - 0.5)c^2/3\Delta t$, and pressure by $p = c^2 \rho / 3\Delta t^2$.

3.6 Multiple Relaxation time lattice Boltzmann model

The BGK LBE model has some drawbacks, especially in simulating fluid flow in porous media, including unable to recover fluid-solid boundary and lack of stability. To overcome these drawbacks, multiple relaxation time (MRT) LBE model had been developed and widely used over the past decade [78].

In the MRT model, fluid particle distribution functions were transformed into moments, and the relaxations were performed in moments rather than directly to the particle distribution function as in BGK model. As such, different moments can be relaxed using different relaxation time parameters. The lattice of the MRT model is the same as that of BGK model.

The MRT model can be written as follows:

$$f_i(x + c\Delta t, t + \Delta t) - f_i(x,t) = -\Omega \left[f_i(x,t) - f_i^{eq}(x,t) \right] \tag{3. 26}$$

where Ω is the collision matrix.

The difference between BGK and MRT model is that, in MRT model an equal number of moments $\left\{m_\beta \middle| \beta = 0,1,...,b\right\}$ of the distribution functions f_i are constructed. The collision is executed in the moment space to achieve different moments relax at different rates. The velocity space V spanned by $\left\{ f_i \middle| i = 0,1,...,b\right\}$ and the moment space M spanned by $\left\{m_\beta \middle| \beta = 0,1,...,b\right\}$ are transferred through a linear mapping $M : \left| m \right\rangle = M \left| f \right.$ and $\left| f \right\rangle = M^{-1} \left| m \right\rangle$. Hence, equation (3.26) can be transformed to the following form

$$f_i \left(x + c\Delta t, t + \Delta t \right) - f_i \left(x,t \right) = -M^{-1} S \left[m\left(x,t \right) - m^{eq} \left(x,t \right) \right] \tag{3. 27}$$

where S is a diagonal collision matrix that determines different relaxation rates for different moments, and m^{eq} is the equilibrium of m. The construction of the transformation matrix M, the moments m and their equilibrium m^{eq} and the diagonal collision matrix S, are lattice based. The details of the MRT lattice Boltzmann model for D2Q9, D3Q15, and D3Q19 were given in Lallemand & Luo [79, 80].

The mapping between velocity and moment spaces can be performed by the linear transformation:

$$\begin{aligned} m &= Mf \\ f &= M^{-1} m \end{aligned} \tag{3. 28}$$

The transformation matrix $M_{ij} = \phi_{ij} \quad i, j = 0,...,b-1$ is constructed from the orthogonal basis vectors,

$$\phi_{0,a} = 1 \quad \phi_{1,a} = e_a^2 - c^2 \quad \phi_{2,a} = 3\left(e_a^2 \right)^2 - 6e_a^2 c^2 + c^4$$

$$\phi_{3,a} = e_{ax} \quad \phi_{5,a} = e_{ay} \quad \phi_{7,a} = e_{az}$$

$$\phi_{4,a} = \left(3e_a^2 - 5c^2 \right) e_{ax} \quad \phi_{6,a} = \left(3e_a^2 - 5c^2 \right) e_{ay}$$

$$\phi_{8,a} = \left(3e_a^2 - 5c^2 \right) e_{az}$$

$$\phi_{9,a} = 3e_{ax}^2 - e_a^2 \quad \phi_{11,a} = e_{ay}^2 - e_{az}^2$$

$\phi_{13,a} = e_{ax}e_{ay} \quad \phi_{14,a} = e_{ay}e_{az} \quad \phi_{15a} = e_{ax}e_{az}$

$\phi_{10,a} = \left(2e_a^2 - 3c^2\right)\left(3e_{ax}^2 - e_a^2\right) \quad \phi_{12,a} = \left(2e_a^2 - 3c^2\right)\left(e_{ay}^2 - e_{az}^2\right)$

$\phi_{16,a} = \left(e_{ay}^2 - e_{az}^2\right)e_{ax} \quad \phi_{17,a} = \left(e_{az}^2 - e_{ax}^2\right)e_{ay} \quad \phi_{18,a} = \left(e_{ax}^2 - e_{ay}^2\right)e_{az}$.

The matrix M for the D3Q19 model is

$$\begin{vmatrix}
1 & 1 & 1 & 1 & 1 & 1 & 1 & 1 & 1 & 1 & 1 & 1 & 1 & 1 & 1 & 1 & 1 & 1 & 1 \\
-30 & -11 & -11 & -11 & -11 & -11 & -11 & 8 & 8 & 8 & 8 & 8 & 8 & 8 & 8 & 8 & 8 & 8 & 8 \\
12 & -4 & -4 & -4 & -4 & -4 & -4 & 1 & 1 & 1 & 1 & 1 & 1 & 1 & 1 & 1 & 1 & 1 & 1 \\
0 & 1 & -1 & 0 & 0 & 0 & 0 & 1 & 1 & -1 & -1 & 0 & 0 & 0 & 0 & 1 & -1 & -1 & 1 \\
0 & -4 & 4 & 0 & 0 & 0 & 0 & 1 & 1 & -1 & -1 & 0 & 0 & 0 & 0 & 1 & -1 & -1 & 1 \\
0 & 0 & 0 & 1 & -1 & 0 & 0 & -1 & 1 & 1 & -1 & -1 & 1 & 1 & -1 & 0 & 0 & 0 & 0 \\
0 & 0 & 0 & -4 & 4 & 0 & 0 & -1 & 1 & 1 & -1 & -1 & 1 & 1 & -1 & 0 & 0 & 0 & 0 \\
0 & 2 & 2 & -1 & -1 & -1 & -1 & 1 & 1 & 1 & 1 & -2 & -2 & -2 & -2 & 1 & 1 & 1 & 1 \\
0 & 0 & 0 & 0 & 0 & 1 & -1 & 0 & 0 & 0 & 0 & 1 & 1 & -1 & -1 & 1 & 1 & -1 & -1 \\
0 & 0 & 0 & 0 & 0 & -4 & 4 & 0 & 0 & 0 & 0 & 1 & 1 & -1 & -1 & 1 & 1 & -1 & -1 \\
0 & -4 & -4 & 2 & 2 & 2 & 2 & 1 & 1 & 1 & 1 & -2 & -2 & -2 & -2 & 1 & 1 & 1 & 1 \\
0 & 0 & 0 & 0 & 0 & 0 & 0 & 1 & 1 & -1 & -1 & 0 & 0 & 0 & 0 & -1 & 1 & 1 & -1 \\
0 & 0 & 0 & 0 & 0 & 0 & 0 & 0 & 0 & 0 & 0 & 0 & 0 & 0 & 0 & 1 & -1 & 1 & -1 \\
0 & 0 & 0 & 0 & 0 & 0 & 0 & 1 & -1 & -1 & 1 & -1 & 1 & 1 & -1 & 0 & 0 & 0 & 0 \\
0 & 0 & 0 & 0 & 0 & 0 & 0 & 0 & 0 & 0 & 0 & -1 & -1 & 1 & 1 & 1 & 1 & -1 & -1 \\
0 & 0 & 0 & 1 & 1 & -1 & -1 & 1 & 1 & 1 & 1 & 0 & 0 & 0 & 0 & -1 & -1 & -1 & -1 \\
0 & 0 & 0 & -2 & -2 & 2 & 2 & 1 & 1 & 1 & 1 & 0 & 0 & 0 & 0 & -1 & -1 & -1 & -1 \\
0 & 0 & 0 & 0 & 0 & 0 & 0 & 0 & 0 & 0 & 0 & -1 & 1 & -1 & 1 & 0 & 0 & 0 & 0 \\
0 & 0 & 0 & 0 & 0 & 0 & 0 & -1 & 1 & -1 & 1 & 0 & 0 & 0 & 0 & 0 & 0 & 0 & 0
\end{vmatrix}$$

The vector m^{eq} is the equilibrium moments and can be obtained as follows:

$m_0^{eq} = \delta\rho \quad m_1^{eq} = e^{eq} = -\sigma|C|$

$m_3^{eq} = \rho_0 u_x \quad m_5^{eq} = \rho_0 u_y \quad m_7^{eq} = \rho_0 u_z$

$m_9^{eq} = 3p_{xx}^{eq} = \frac{1}{2}\sigma|C|\left(2n_x^2 - n_y^2 - n_z^2\right) \quad m_{11}^{eq} = p_{zz}^{eq} = \frac{1}{2}\sigma|C|\left(n_y^2 - n_z^2\right)$

$m_{13}^{eq} = p_{xy}^{eq} = \frac{1}{2}\sigma|C|\left(n_x n_y\right) \quad m_{14}^{eq} = p_{yz}^{eq} = \frac{1}{2}\sigma|C|\left(n_y n_z\right) \quad m_{15}^{eq} = p_{xz}^{eq} = \frac{1}{2}\sigma|C|\left(n_x n_z\right)$

$$m_2^{eq} = m_4^{eq} = m_6^{eq} = m_8^{eq} = m_{16}^{eq} = m_{17}^{eq} = {}^{eq}_{18} = 0$$

The gradient C in the above equations is computed by

$$C = \frac{3}{c^2 \Delta t} \sum_i w_i e_i \phi\left(t, x + e_i \Delta t\right) \tag{3. 29}$$

The normalized gradient is $n_a = C_a / |C|$. The moments $\{m_k, k = 0,3,5,7\}$ are conserved during the collision. The matrix S is a diagonal collision matrix, consisting of relaxation rates $\{s_{i,i}, i = 1,...b-1\}$ .They are called the eigen-values of the collision matrix $M^{-1}SM$. For simulating fluid flow, the values of the each relaxation parameters can be chosen as follows:

$$\begin{aligned} s_1 = s_2 = s_9 = s_{10} = s_{11} = s_{12} = s_{13} = s_{14} = s_{15} = -s_v \\ s_4 = s_6 = s_8 = s_{16} = s_{17} = s_{18} = -8\frac{(2 - s_v)}{(8 - s_v)} \end{aligned} \tag{3. 30}$$

The relationship between the relaxation parameters and the kinematic viscosity of the fluid is given by

$$\mu = \frac{c^2}{3\Delta t}\left(\frac{1}{s_v} - \frac{1}{2}\right)$$

Other relaxation parameters do not affect fluid viscosity, but they might affect solution stability. The stability can be improved by tuning other relaxation time parameters.

3.7 Boundary treatment

The boundary comes into effect during the streaming step [81-83]. We discuss two types of boundaries that will be encountered in simulating fluid flow in porous media and in fuel cells: prescribed pressure boundary and prescribed velocity boundary. In practice, the LBE models simulate fluid flow based on particle distributions functions. As a result, the boundary treatment in LBE model is to find all the particle distributions on the boundary, which do not exist, so as to honour the prescribed boundary conditions.

3.7.1 Static solid walls

The solid walls in fluid flow are usually treated as a boundary where the fluid velocity is assumed to be known. There are two types of static solid boundaries: slip boundary and non-slip boundary.

3.7.1.1 No-slip Boundary

Fluid-solid interface is often treated as non-slip boundary where the fluid velocity is assumed to be zero. Such boundary is usually solved by the bounce-back method. The bounce back method was derived from the lattice gas automata method for solving no-slip boundary [77, 84]. In bounce-back method, the distribution functions at a lattice site adjacent to a solid boundary might not be able to be obtained from the neighbouring solid site and hence need to be specified through the boundary condition. In the bounce- back method, the distribution function moving towards the solid boundary are simply bounced back to the node where the particle distribution function come from at the end of each time step [85, 86].

When fluid particles hit a solid wall, they are reflected 180^o and then move at the same speed, but in the opposite direction. The bounce-back method can be applied either at wall lattice sites or halfway along the links between the fluid lattice and solid lattice sites as shown in Figure 3.5. Consequently, the momentum of all particles at the solid wall sums to zero. This is physically appropriate when a solid wall is sufficiently rough to prevent any net fluid motion along it. The bounce-back method is a simple and popular method for solving no-slip boundary in lattice Boltzmann simulations. For the bounce-back method to be second-order accurate, it often locates the not-slip boundary between the last fluid and first solid lattice sites as shown in Figure 3.5. The exact location recovered by the bounce-back method might depend on the geometry of the system, the relaxation parameter τ of the and lattice Blotzmann models being used [86, 87] and even the magnitude of external force. For complicated curved solid boundary, more robust boundary treatment methods might be needed [88, 89].

Boundary treatment is an issue in the lattice Boltzmann model that progress is still being made. For curved boundary, sophisticated second-order boundary treatment methods have been developed, which can accurately model no-slip boundary [90, 91]. For simulating fluid flow in porous media, however, the bounce back still remains the most popular

method due to its simplicity, and that the solid-fluid boundary is often approximated by zig-zag interfaces. In the following simulations, all the solid-fluid interfaces will be solved by the bounce-back method.

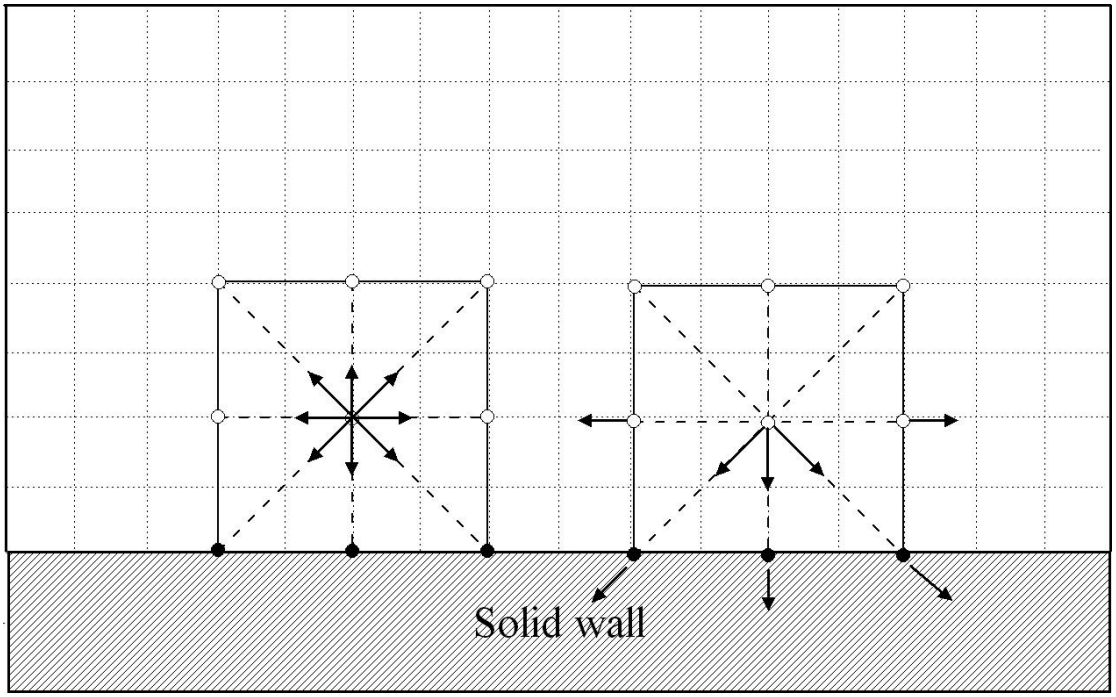

Figure 3.5 Lattice vectors at a fluid node (centre point, left) before streaming and after streaming

3.7.1.2 Slip Boundary

When a solid wall is smooth enough with negligible friction, fluid velocity along it might not be zero. In this case, it should be treated as a slip boundary as shown in Figure 3.6.

On the slip boundary, the tangential momentum balance of the fluid flow on the wall needs to be maintained. There is no momentum exchange with the wall along the tangential direction. The method for treating the slip boundary can be written in the following matrix form:

$$\begin{bmatrix} f_2 \\ f_5 \\ f_6 \end{bmatrix} = \begin{pmatrix} 0 & 0 & 1 \\ 0 & 1 & 0 \\ 1 & 0 & 0 \end{pmatrix} \begin{bmatrix} f_4 \\ f_7 \\ f_8 \end{bmatrix} \tag{3. 31}$$

where the $f_2 = f_4$ implies that the velocity component in the direction normal to the wall is zero.

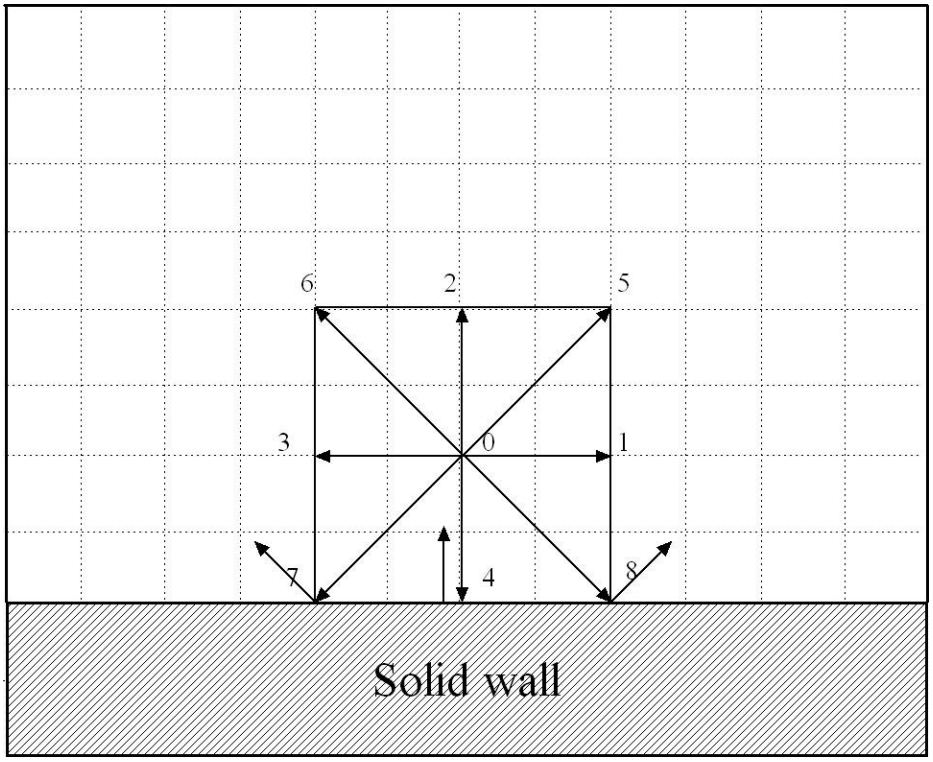

Figure 3.6 Slip boundary

3.7.2 Prescribed pressure boundary

Prescribed-pressure boundary is another boundary encountered for fluid flow in fuel cells. Many other applications need also to treat the prescribed-pressure boundaries, such as the inlets and outlets in open channel flow. In lattice Boltzmann model, the prescribed pressure boundary can be easily solved by assuming that equilibrium particle distribution functions are the same as the associated particle distribution functions as follows:

$$f_a(x_1, j) = f_a^{eq}\left[\rho(x_1, j), u(x_1, j)\right] \tag{3. 32}$$

where x_1 is the location of the inlet boundary.

For flow where it is not the pressure but the pressure gradient is specified, the specified pressure-gradient boundary can be solved in a similar way. For example, for channel flow, the outlet boundary is often treated as a boundary where the pressure gradient is zero. Since the pressure in LB model is linear function of fluid density, zero pressure-gradient boundary can be solved as follows:

$$f_a(x_L - 1, j) = f_a(x_L, j) \tag{3. 33}$$

where x_L is the location of the outlet boundary.

Another method for solving the prescribed-pressure boundary is the method proposed by Zou and He [92].

In LB model, the pressure is related to fluid density as $p = c^2 \rho$. A prescribed pressure boundary is equivalent to a prescribed fluid density boundary. It is assumed that prescribed densities ρ_{inlet} and ρ_{outlet} are imposed at the inlet and outlet of a domain to generate a pressure drop as shown in Figure 3.7.

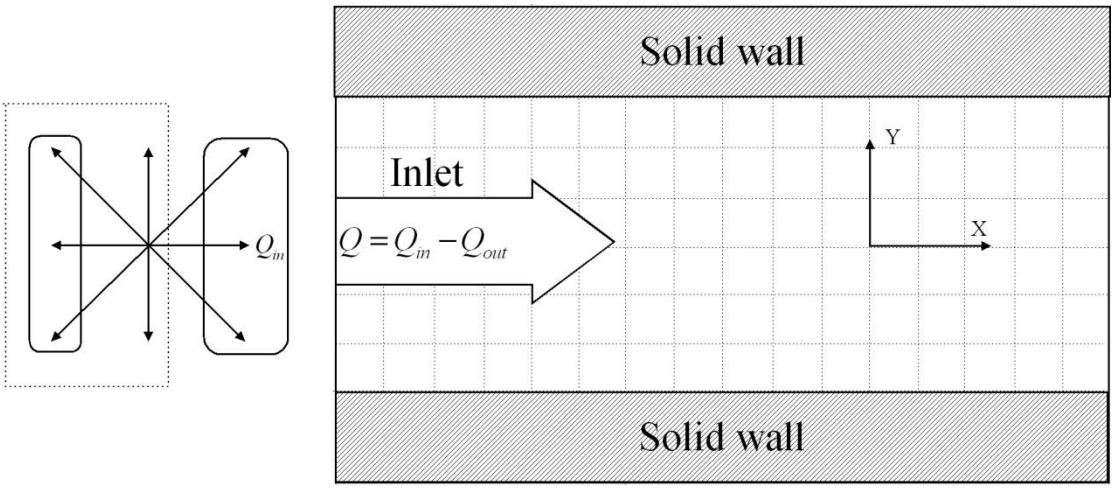

Figure 3.7 Sketch for prescribed pressure boundary treatment

Prescribed pressure was applied at the inlet and the outlet boundaries, both assumed to be perpendicular to the *z* direction as an illustrative example shown in Figure 3.7. In the LB model, the fluid pressure is related to fluid density in $\boldsymbol{p} = \boldsymbol{c}^2 \rho$. A prescribed pressure boundary is therefore equivalent to a prescribed density boundary, and was solved in bounce-backing the non-equilibrium distribution function using the method proposed by

[93]. As shown in Figure 3.7, the inlet boundary is perpendicular to the directions with the lattice velocities of $\boldsymbol{c}_5, \boldsymbol{c}_{11}, \boldsymbol{c}_{12}, \boldsymbol{c}_{15}, \boldsymbol{c}_{16}$, and the distribution functions f_5, f_{11}, f_{12}, f_{15}, f_{16} come from outside of the domain and are thus unknown; they hence have to be determined by the known distribution functions to satisfy the specified boundary conditions. For the prescribed pressure boundary, the unknown distribution functions at the inlet boundary shown in Figure 3.7 should satisfy the following constraints:

$$f_5 + f_{11} + f_{12} + f_{15} + f_{16} = \rho_{in} - (f_0 + f_1 + f_2 + f_3 + f_4 + f_6 + f_7 + f_8 + f_9 + f_{10} + f_{13} + f_{14} + f_{17} + f_{18}) \quad (3.\ 34)$$

If the velocity component in the z direction is u_z, the expression of the momentum in the z direction gives:

$$f_5 + f_{11} + f_{12} + f_{15} + f_{16} = \rho_{in} u_z + (f_6 + f_{13} + f_{14} + f_{17} + f_{18}) \quad (3.\ 35)$$

where ρ_{in} is the fluid density at the inlet boundary. From the above two equations we have,

$$\rho_{in} = \frac{1}{1-u_z}(f_0 + f_1 + f_2 + f_3 + f_4 + f_7 + f_8 + f_9 + f_{10}) + 2(f_6 + f_{13} + f_{14} + f_{17} + f_{18}) \quad (3.\ 36)$$

in which f_5, f_{11}, f_{12}, f_{15}, f_{16} remain unknown. To close the system, we assume that the bounce-back rule is still correct for the non-equilibrium part of the particle distributions normal to the boundary, that is,

$$f_i = f_i^{eq} + (f_{i'} - f_{i'}^{eq}) \quad (3.\ 37)$$

where $f_{i'}$ is the particle distribution function in the i' direction opposite to the lattice velocity $\boldsymbol{c}_i$, that is, $\boldsymbol{c}_i = -\boldsymbol{c}_{i'}$. From the above equation it suffices to determine all the unknown distribution functions. However, in order to keep the moments in the x and y directions correct, these distribution functions are modified as follows:

$$f_i^* = \frac{f_i - (j_x / c_{ix} + j_y / c_{iy})}{2} \quad i = 5,11,12,15,16 \quad (3.\ 38)$$

where $j_x = \sum_{a=0}^{18} f_a c_{ax}$ and $j_y = \sum_{a=0}^{18} f_a c_{ay}$ to ensure that the moment in the z direction remains unchanged by adding j_x / c_{ix} and f_y / c_{iy} to the moments in the x and y directions,

respectively. This makes the velocity components in the x and y directions zero as required at the prescribed pressure boundaries.

When simulating gas flow in GDLs, in order to reduce the influence of solid fibre on inlet and outlet boundaries, four more layers of lattices, which are free of solid, were added to each of the inlet and outlet boundaries to function as the inlet and outlet reservoirs used in most column experiments is soil sciences. The other four sides of the samples were treated as periodic boundaries.

3.8 Relation between LBM units and physical units

The LBM simulations are normally run using dimensionless units. As such, the simulated results should be converted to physical units. Since the viscosity in the LB model depends on, not only on the relaxation time parameters, but also on time step and the side length of the cubic lattice, the transformation between physical units and lattice units is not straightforward. For length, velocity, density, viscosity and pressure, the corresponding conversion factors are as follows, in which the subscripts L and P denote the variables in lattice unit and physical unit, respectively:

$$x_P = dx \cdot x_L \tag{3. 39}$$

$$u_P = \frac{dx}{dt} u_L \tag{3. 40}$$

where x_P is the length in the physical unit and x_L is the length in the lattice unit, dx is the length scaling factor, and dt is the time scaling factor. Similarly, fluid density, viscosity and fluid pressure in LB and physical units are transformed through as follows in (3.41)-(3.43).

$$\rho_P = \frac{dm}{dx^3}\rho_L = \frac{m}{dx^3}\rho_L \tag{3. 41}$$

$$v_P = \frac{dx^2}{dt}v_L \tag{3. 42}$$

$$p_P = \frac{dm}{dxdt^2}p_L = \frac{m}{dxdt^2}p_L \tag{3. 43}$$

As an illustrative example, we take flow in a pile to demonstrate the unit transformation. The length and diameter of the pipe are L=150cm and D=50 cm, respectively.

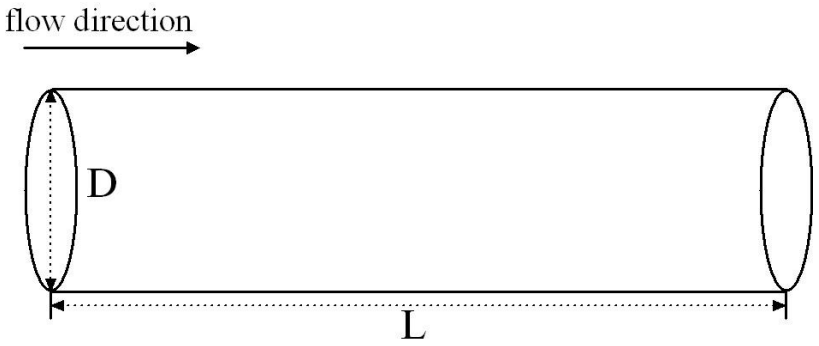

Figure 3.8 A cylinder for demonstrating lattice unit and physical unit transformation

The first is to calculate the lattice numbers. If the cylinder is divided into a number of cubes, and the side length of each cube is $dx = dy = dz = 1cm$

The lattice numbers in the x and y and z directions are

$$N_x = N_y = \frac{Diameter}{dx} = \frac{50}{1} = 50$$

$$N_z = \frac{z}{dz} = \frac{150}{1} = 150$$

with the z pointing to the axial direction.

For a given relaxation time parameter, the value of the time step *dt* is determined by fluid viscosity. As an illustrative example, we assumed the simulated fluid is hydrogen. The relations between the lattice kinematic viscosity and the physical kinematic viscosity is

$$\mu_P = \frac{dx^2}{dt}\mu_L$$

where u_P and μ_L are viscosity in the physical and lattice unit, respectively.

The dynamic viscosity of hydrogen is $8.76\times10^{-6} Pa\cdot s$ or Ns/m^2 or kg/ms , and its density is $0.09kg/m^3$. The kinematic viscosity is :

$$\mu_P = 97.3\times10^{-6} m^2/s = 97.3mm^2/s = 0.973cm^2/s$$

If the hydrogen was simulated with a relaxation time parameter τ=3.5, the value of the viscosity in the lattice unit is then μ_L=1.0. Therefore, the size of the time step should be

$$0.973cm^2/s = \frac{1.0cm^2}{dt}\times1.0$$

$$dt = 0.973s$$

The relationship between the density in physical and lattice units are is

$$\rho_P = \frac{m}{dx^3}\rho_L$$
$$\rho_{H_2} = 0.09kg/m^3$$

where m is the mass of hydrogen in a single lattice. If the fluid density in the lattice unit is 1, the mass of the hydrogen in one cube can then be calculated from

$$0.09kg/m^3 = \frac{m}{1cm^3}\times1.0$$
$$0.09kg/m^3 = 90\times10^{-6} g/cm^3$$
$$90\times10^{6} g/cm^3 = \frac{m}{1cm^3}\times1.0$$
$$m = 90\times10^{6} g$$

The pressure in the LB model is linearly related to fluid density as follows

$$p_P = \frac{dm}{dxdt^2}p_L = \frac{m}{dxdt^2}p_L$$

When fluid density in the lattice unit is 1, the pressure in the lattice unit is,

$$P_L = \frac{\rho_L}{3} = \frac{1.0}{3} = \frac{1}{3}$$

Therefore, the pressure in physical unit is;

$$
\begin{aligned}
p_P &= \frac{90\times10^6\, g}{1cm\cdot(0.973)^2\,(s)^2}\times\frac{1}{3} \\
&= \frac{90\times10^6\, g}{0.95cm(s)^2}\times\frac{1}{3} \\
&= \frac{90\times10^6\, g}{0.95\times10^{-2}\, ms^2}\times\frac{1}{3} \\
&= 31.6\times10^8\, g/ms^2 \\
&= 31.6\times10^2\, kPa
\end{aligned}
$$

Chapter 4 Comparison of single relaxation and multiple relaxation time LB models for pore-scale simulation and permeability calculation

4.1. Introduction

Chapter 3 introduced the single relaxation (BGK) and the multiple relaxation (MRT) model for simulating single-phase fluid flow at low Reynolds and low Mach numbers under an assumption that the fluid is weakly compressible and in isothermal condition. Although both BGK and MRT models have been tested against analytical solutions by other researchers, directly testing its accuracy for simulating fluid flow in porous media proves to be difficult because of the difficulty of measuring flow velocity and pressure distribution at pore scale. Instead of direct test, in this chapter we will validate the two models for estimating the permeability of a pack of glass beads. After the validation, we apply them to simulate gas flow in the GDLs with different porosities.

As reviewed in Chapter 1, most practical fuel cell models are based on macroscopic approaches in which the details of pore geometry are not explicitly resolved. Instead, their impact on gas flow is described by a parameter, permeability, by volume–averaging the pore-scale flow process [59-62]. As such, estimating the permeability of GDL is a requirement in macroscopic modelling. Modelling gas flow at pore scale can provide a way to calculate permeability of the GDL.

In fuel cells, the electrochemical reactions occur only in the presence of the catalysts that are scattered at gas-solid interface in the catalyst layer. Knowing how and where the gas flows from the GDL to the catalyst layer is important to understand and hence improve fuel cell performance. The volume-average approach cannot accurately describe such surface-based electrochemical reactions. Therefore, understanding the pore-scale processes is especially important for improving fuel cell design. Because of the opaque nature of most porous materials, however, the earlier work on pore-scale model was usually to idealize the void space into some simple geometry.

Permeability is an important transport property of porous materials and is influenced by microscopic structure at scales of a few microns or less. The ability to predict the

permeability of a porous medium and understanding the impact of the pore structure is therefore imperative, and has been investigated in many areas. Thanks to the development in imaging technologies over the past few decades, it is now possible to visualize the interior structure of an opaque material at a scale as fine as one micron. This, in a combination with the breakthrough in computational methods, has made direct simulation of fluid flow through the real void space in a porous medium (and hence to calculate its permeability) feasible. The LB method is one of such models. LB model is simple and flexible to deal with complicated boundary and microscopic forces, and hence has been exploited over the past few years to calculate the permeability of porous materials used in a wide range of fields, such as hydrology, oil recovery, and fuel cells industry [30, 94]. For example, the permeability of a porous medium can be estimated from its structure generated from 2D thin sections [95]. The limitaiton of the 2D thin section is that it applies only to homogenous matrails. Over the past few years, there has been an increase in the use of the 3D images aquired by X-ray computed micro-tomography to calculate the permeability. For example, Zhang et al. [96] and Fredrich and Digiovanni [97] calcaulted the change of permeaility with the size of supporting volume, finding that the size of represeative volme element (REV) for porosity differs from the REV for permeability.

The purpose of this chapter is to test the two LBM models – BGK model and MRT model for pore-scale simulation. X-ray CT images of glass beads are used to verify the model, and the verified models are then used to simulate fluid flow in 3D images of GDLs at a resolution of 1.7 microns; the simulated pore-scale velocity is then used to estimate the permeability of the GDL in both through-plane and in-plane directions. When gas flows through the gas-supply channel the gas pressure drops. As a result, the gas flow in the GDL is not always perpendicular to the channel and membrane. Because of its structure, the GDL is anisotropic in that its ability to conduct gas in the through-direction differs from that in the in-plane direction. Measuring experimentally the in-plane permeability is difficult because the thickness of the GDL is only a few hundreds of microns. Therefore, there is an increase over the last few years in using numerical models to estimate the permeability. In this work, I will use the combination of imaging technology and the developed LB models to calculate the anisotropic permeability of GDL. Similar work was also done by Clague et al. [98], who calculated the permeability of statistically generated fibrous media using the LB model. Whiles their work provides some insight into the

anisotropic nature of the GDL, but the numerically generated GDLs used by them are only statistically similar to real GDLs; they are not geometrically same as or even similar to the real ones.

4.2 The Darcy's law and anisotropic permeability

Darcy investigated experimentally water flow in a sand column. He found that water flow rate through the column is proportional to the water level difference, ΔH, between the two ends of the column as follows

$$q = K\frac{\Delta H}{L} \tag{4. 1}$$

where q is flow rate, L is the height of the column, K is hydraulic conductivity. Equation (4.1) is known as Darcy's law, and has been widely used to describe fluid flow in porous materials. For gas and water flow in GDL, equation (4.1) can be modified into the following general form:

$$\boldsymbol{q} = \frac{\boldsymbol{k}}{\mu}\left(\nabla \boldsymbol{P} - \rho \boldsymbol{g}\right) \tag{4. 2}$$

where ρ is the density of fluid, μ is kinematic viscosity of the fluid, k is abolute permeability, g is gravitational acceleration, and P is pressure. The permeability is the function of pore geometry in a porous medium. The second term inside the bracket on the right-hand side of Equation (4.2) is due to gravity, and is only present for flow in the vertical direction.

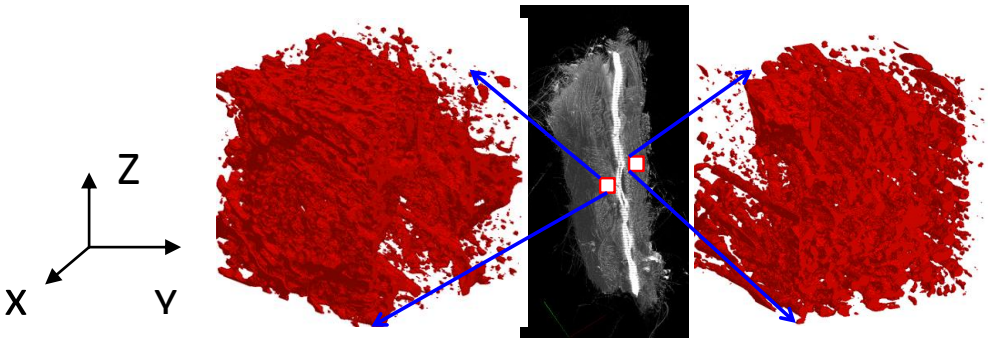

Figure 4.1 The domain of GDL for LBM simulation; the white strip in the centre is the polymer electrolyte membrane

The size of a fuel cell is approximately 20cm in the in-plane direction (direction parallel with the electrolyte membrane), and the thickness of the GDL is less than 1 mm. This is too big for LB model which simulates gas flow at micron scale. In our LB simulation, we only chose a small part of the GDL as shown in Figure 4.1; its size is in the *x*, *y* direction (in-plane direction) and *z* direction (through-plane direction) depends on simulations are the details will be given in what follows. Two illustrative 3D image of the simulated GDL are also shown in Figure 4.1.

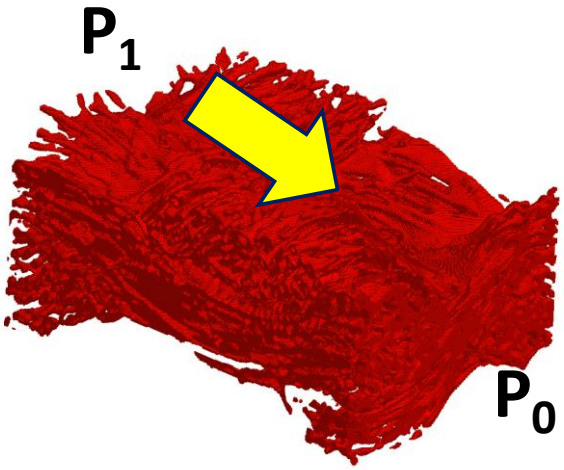

Figure 4.2 A 3D X-ray CT image of GDL used in the LBM simulation

In LBM simulations, a pressure drops is applied to the two sides of the image to drive the gas flow as shown in Figure 4.2, and the other four sides were treated as periodic boundaries as described in Chapter 3. Once flow was deemed to have reached steady state, the permeability of the medium was calculated based on the Darcy's law as follows:

$$\boldsymbol{q} = \frac{\boldsymbol{k}}{\mu}\nabla \boldsymbol{P} \tag{4. 3}$$

where $\boldsymbol{q}$ is volume-average flow rate in the image, k is the absolute permeability in the flow direction, ∇P is pressure gradient across the image in the flow direction. From the above Darcy's law, the permeability can be expressed as follows:

$$\boldsymbol{k} = \frac{\mu \cdot \boldsymbol{q}}{\nabla \boldsymbol{P}} \tag{4. 4}$$

In the LB model, the kinematic viscosity is related to the time step size, the size of the voxel and the value of the relaxation-time. In the MRT model, the kinematic viscosity is related to the relaxation time parameters as follows

$$\mu = \frac{c^2}{3\Delta t}\left(\frac{1}{s_9} - \frac{1}{2}\right) = \frac{c^2}{3\Delta t}\left(\frac{1}{s_{13}} - \frac{1}{2}\right) \tag{4. 5}$$

And in the BGK model, the viscosity is related to the relaxation-time parameter as follows:

$$\mu = \frac{\delta x^2}{\Delta t}\left(\frac{1}{\tau} - \frac{1}{2}\right) \tag{4. 6}$$

where δx is the size length of each voxel in the x-ray image and Δt is time step.

The relaxation parameters in both BGK and MRT models represent the rate at which the fluid particle distribution functions approach their values at equilibrium state. Consequently, the larger the relaxation parameters are, the more rapid the flow will settle to equilibrium. However, in solving the solid-gas interface using the bounce-back method in the BGK model, the location of the solid-wall boundary varies with the relaxation parameter. As a result, the calculated permeability might vary unrealistically with fluid viscosity. Pan et al [99] evaluated the solid-wall boundary treatments using different LB models, concluding the that the BGK model is not suitable for estimating media permeability. To further test the performance of BGK, and the improvement and the cost of the MRT model, we simulated gas flow in various X-ray images using both BGK and MRT models.

When a pressure gradient is applied in a direction in the 3D micro-structure, say in the z direction, the fluid flows not only in the z direction, but also in the x and y directions; the average flow rate in each of the three directions was characterized by a permeability component. Overall, the permeability of an anisotropic GDL is a second-order tensor with six different components; each component can be calculated as follows:

When a pressure gradient ∇P is applied in the x direction:

$$k_{xx} = \frac{\mu q_x}{\nabla P}; k_{xy} = \frac{\mu q_y}{\nabla P}; k_{xz} = \frac{\mu q_z}{\nabla P} \tag{4. 7}$$

When the pressure gradient ∇P is applied in the y direction:

$$k_{yy} = \frac{\mu q_y}{\nabla P}; k_{yx} = \frac{\mu q_x}{\nabla P}; k_{yz} = \frac{\mu q_z}{\nabla P} \tag{4. 8}$$

When the pressure gradient ∇P is applied in the z direction:

$$k_{zz} = \frac{\mu q_z}{\nabla P}; k_{zx} = \frac{\mu q_x}{\nabla P}; k_{zy} = \frac{\mu q_y}{\nabla P} \tag{4. 9}$$

In the above equations, the kinematic viscosity μ was calculated from Equation (4.5) for MRT model, and Equation (4.6) for the BGK model. If L_i is the length of the simulated domain in the ith direction, and the flow rate q_x, q_y, q_z are calculated by

$$q_x = \frac{c^3 \sum_i u_{i,x}}{L_x L_y L_z}, q_y = \frac{c^3 \sum_i u_{i,y}}{L_x L_y L_z}, q_z = \frac{c^3 \sum_i u_{i,z}}{L_x L_y L_z} \tag{4. 10}$$

where $u_{i,x}$, $u_{i,y}$ and $u_{i,z}$ are the three fluid velocity components in the x, y and z directions respectively in the *ith* voxel, and c=δx/Δt. Because the permeability is a symmetrical second-order tensor, it has $k_{xy} = k_{yx}, k_{xz} = k_{zx}$ and $k_{yz} = k_{zy}$. The physical interpretation of each component is straight forward: k_{ij} represents the ability of a medium to conduct fluid in the ith direction when a pressure drop is applied in the jth direction.

The BGK model is often criticized for giving rise to a viscosity-dependant permeability due to the dependence of fluid-solid location on the relaxation time when using the bounce-back method to resolve non-slip boundary [33, 67]. However, as proven in [100], when the relaxation time is unity, the location of the fluid-solid interface can be accurately recovered. Since the viscosity in LB models depends on both time step and the relaxation time for a given lattice, there are two ways to calculate fluid viscosity. One is to

fix the time step, and a change in fluid viscosity is calculated by changing the relaxation time; this could result in viscosity-dependant permeability. In contrast, one can fix the relaxation time, and the change in viscosity is honoured by changing the time steps; this would not lead to viscosity-dependant permeability. Since the fluid-solid location is accurately resolved using $\tau = 1$, in the simulations, we fix the relaxation time to be unity, and the viscosity of any fluid was recovered by adjusting the time step. Since BGK model is more efficient and simpler than MRT model, especially when $\tau = 1$ in which the cost for calculating collision can be saved, our previous work using both BGK model and MRT model reveal that the former should be more competitive than the latter for pore-scale simulation of fluid flow at steady state [70, 101]. To demonstrate this, we compared the accuracy and efficiency of the BGK and MRT models for simulating gas flow in the three samples shown in Figure 4.4. All the simulations were run in a Dell Precision T5400 workstation with Intel CPU E5420. To make a fair comparison, once the following criterion was satisfied in both BGKLB and MRTLB simulations, the flow was deemed to have reached steady state and the simulations were terminated.

$$\frac{\sum_{i=1}^{N}\left|u\left(x_i, t+100\right)-\left(x_i, t\right)\right|}{\sum_{i=1}^{N}\left|u\left(x_i, t\right)\right|} < 10^{-5}$$

where N is the number of the fluid voxel in the simaulted image, $u(x_i, t)$ is the gas velocity at time t in the ith voxel.

4.3 Performance of the BGK model

All the simulations presented in this section used the unity relaxation time parameter, that is, τ=1.0. We first validate the model against measurements from pack of glass beads and then apply it tie simulate gas flow in carbon GDLs.

4.3.1 Test of the model

We tested the BGK model against water flow in a column of glass beads. The images were provided by Chen et al [102]. The size of each voxels is six microns. Three images with different porosity were simulated. The size and porosity of each image is listed in Table 4.1, and Figures 4.3(a-c) shows the three images.

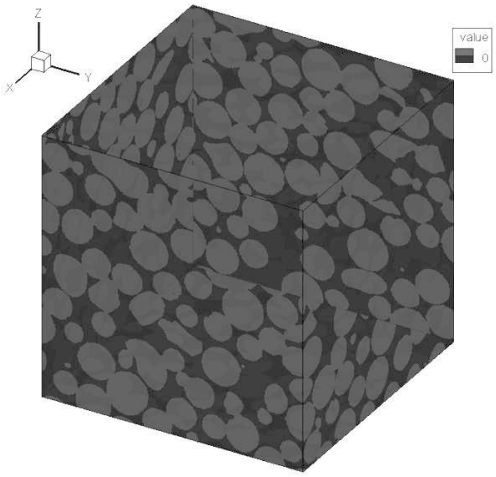

Figure 4.3a The 3D image (299×299×299) with porosity of 0.263

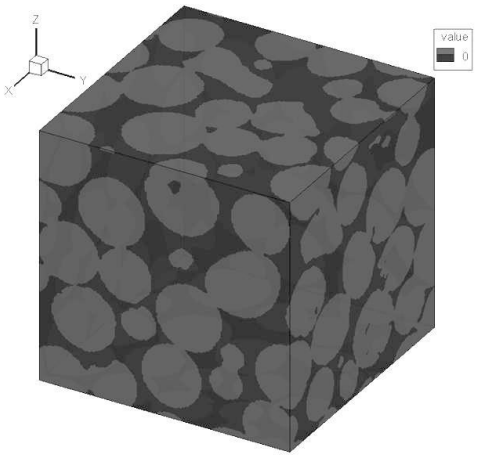

Figure 4.3b The 3D image (160×160×160) with porosity of 0.263

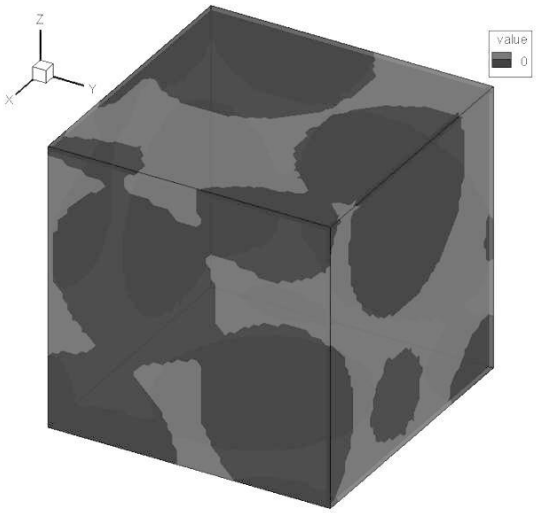

(c)

Figure 4.3c The 3D image (60 ×60 ×60) with porosity of 0.263

Table 4. 1: Size and porosity of each of the three glass beads images

Image	a	b	c
Size (voxels)	299 × 299 × 299	160 × 160 × 160	60 × 60 ×60
Size (mm^3)	1.8 × 1.8 × 1.8	0.96 × 0.96	0.36 × 0.36 × 0.36
Porosity	0.263	0.394608	0.662861

Figure 4.4 shows the relationship between the porosity and simulated permeability of the glass beads for porosity in the range from 0.2 to 0.6. As anticipated, the permeability increases with the porosity. We compare the simulated permeability with the experimental measurement of Chen et al [102], and the results show a close agreement. Fitting the change of permeability with the porosity to the K-C equation reveals that with an increase in porosity, the K-C equation becomes less accurate because this equation was derived for low-porosity granular media.

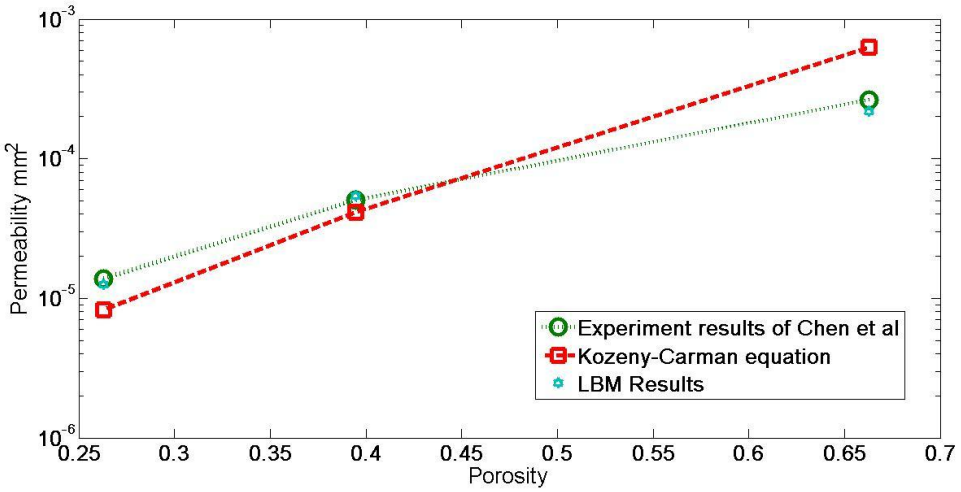

Figure 4. 4 Comparison of the simulated permeability with the measurement of Chen et al [102] and the predictions of Kozeny Carman Equation

To evaluate the ability of LB model for calculating the permeability tensor of the glass beads, fluid flow through the three samples was simulated. For each sample, the pressure gradient was applied in each of the three directions. Figures 4.5-4.7 show the simulated permeabilty when the pressure gradient is applied in the x, y and z directions, respectively. The permeability in both the principal direction and off-principal direction was calculated, and the results show that for glass beads, the permeability in the principal flow direction is one to two order of magnitude higher than that in the off-principal directions. But the permeability in the three principale directions are very close beucase the glass beads are istropic and uniform.

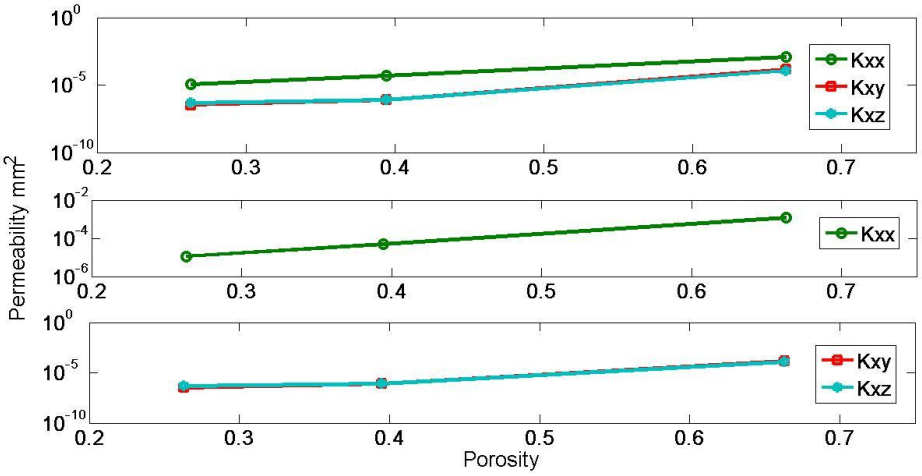

Figure 4. 5 The simulated permeability components when fluid flows in the x direction

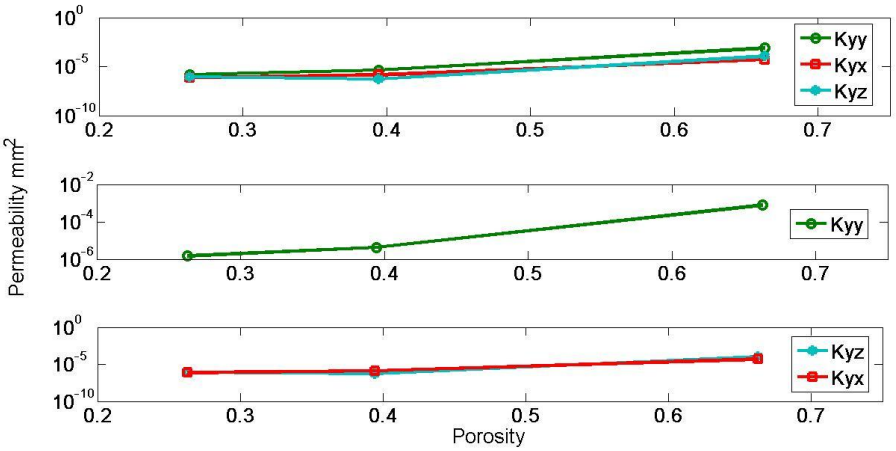

Figure 4. 6 simulated permeability components when fluid flows in the y direction

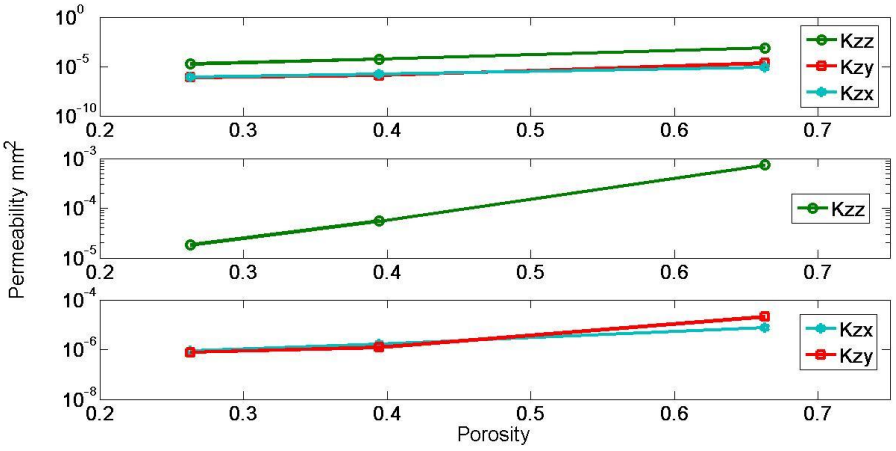

Figure 4. 7. The simulated permeability components when fluid flows in the z directions

4.3.2 Permeability and tortuosity of GDL

The GDL investigated this work carbon paper. Figure 4.8a shows the SEM image of the carbon paper, and Figures 4.8 (b), (c) and (d) show the microstructure of the reconstructed GDLs with size of $50\times50\times150$ voxels, of $89\times150\times154$ voxels, and of $177\times150\times154$ voxels, respectively. The details of each sample are given in Table 4.2. The side length of each voxel is 1.7 microns.

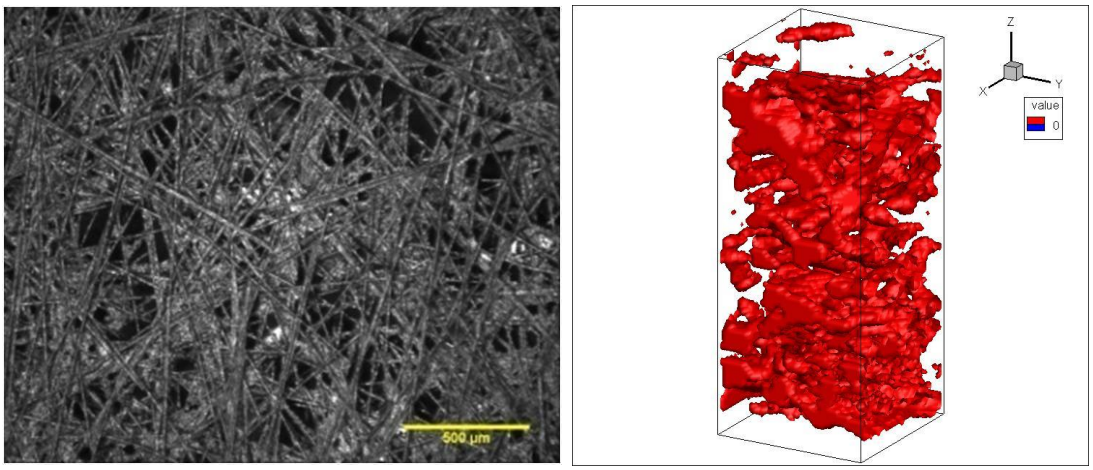

(a) (b)

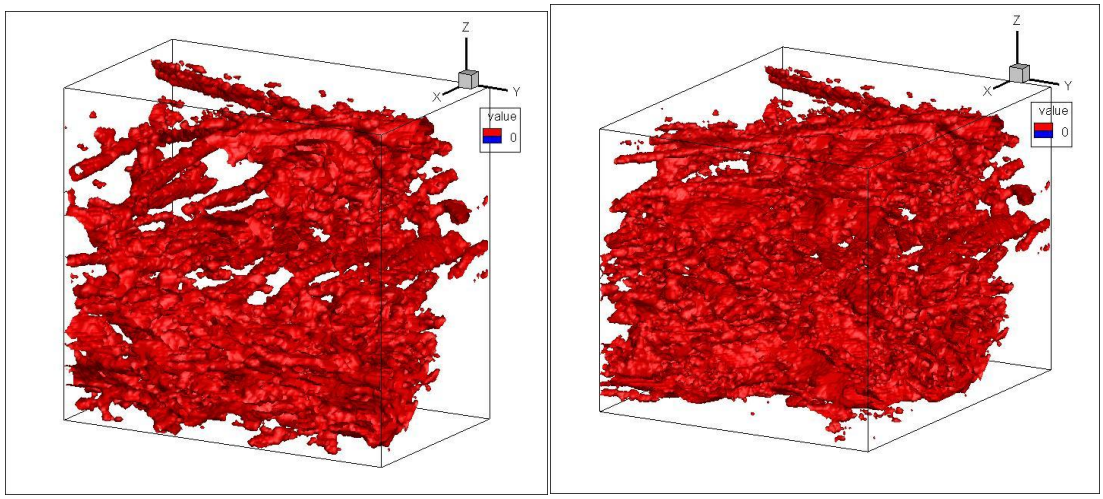

(c) (d)

Figure 4. 8 Micro-structure of the GDLs made by carbon paper: SEM image (a), 3D geometry of the reconstructed X-ray image of Sample 1 (b), Sample 2 (c), and Sample 3 (d)

Table 4. 2 The size and porosity of each of the three simulated GDL samples

GDL	Image size in voxels			Image size in μm			Pixel size	Porosity
	X	*Y*	*Z*	*X*	*Y*	*Z*		
Sample 1	50	50	120	87	87	211.2	1.76	0.766163
Sample 2	89	150	141	156.64	264	248.16	1.76	0.830897
Sample 3	177	150	142	311.52	264	249.92	1.76	0.863899

Most macroscpic fuel cells models take porosity and permeability of GDL as input paramters. These parameter have sinigicant imapct on fuel cell perforamce as they control fluid flow and electrical conductance. For a given material, it is easy to meaures its porosity. Therefore it is not surprise that there has been a great interest in the possibility of using GDL's porosity to predict its permeability [103-106]. However, most available work in the literature was for homogeneous media. The anisotropic natuer of GDLs is a key factor that needs to be considered in selecting porous materials for fuel cells, particularly for cells desiged with interdifitated flow field. For a selected material, understanding the relationship between its permeability and porosity would be helpful to optimize the coating microstructures of the GDL [107].

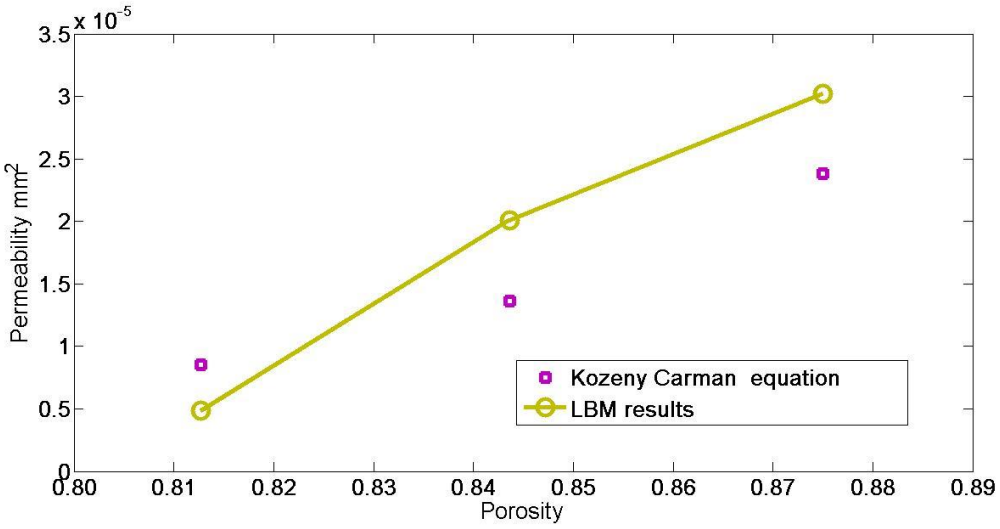

Figure 4. 9 Comparison of the simulated permeability and the predictions of Kozeny-Carman equation for the Gas Diffusion Layers (GDLs)

Figure 4.9 shows the simulated permeability of GDLs in comparison with that fitted by the K-C equation; the agreement is good. Again, the permeability increases with the porosity. For fuel cell performance, this means that with an increase in porosity, the fuel cells can produce more electrons and is unlikely to be flooded by its by-product, liquid

water [108]. However, if the electrons can become current depends on the electrical conduction of the GDL and the electrodes.

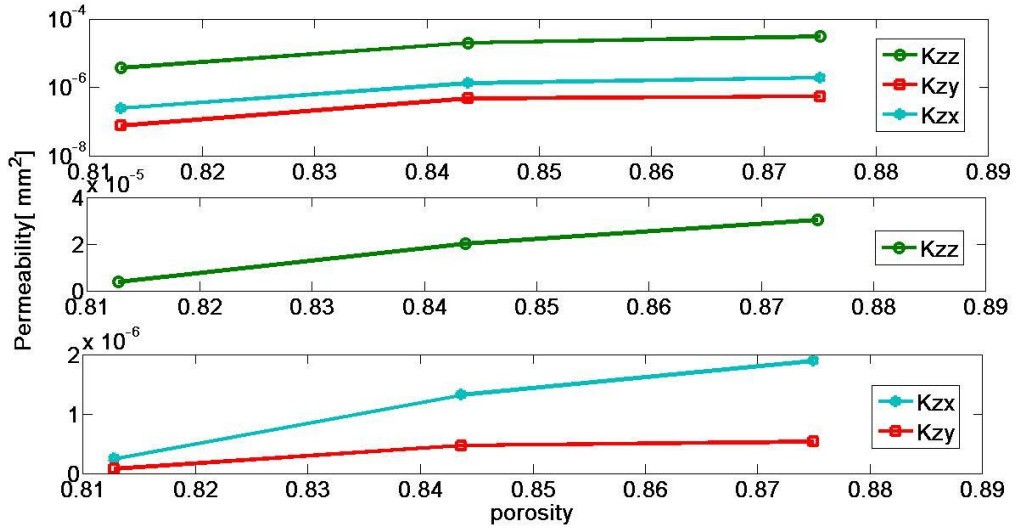

Figure 4. 10 The simulated permeability components when fluid flows in the z direction

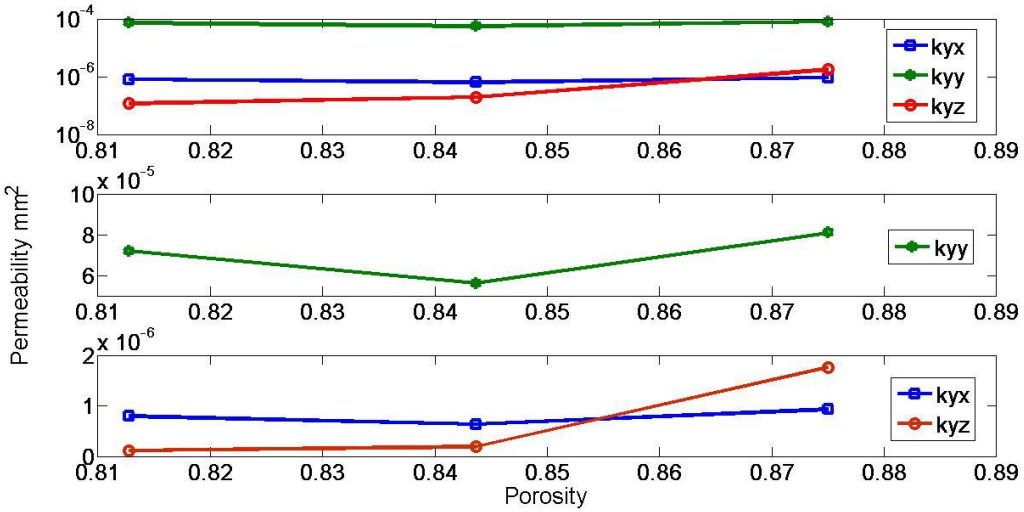

Figure 4. 11 The simulated permeability components when fluid flows in the y direction

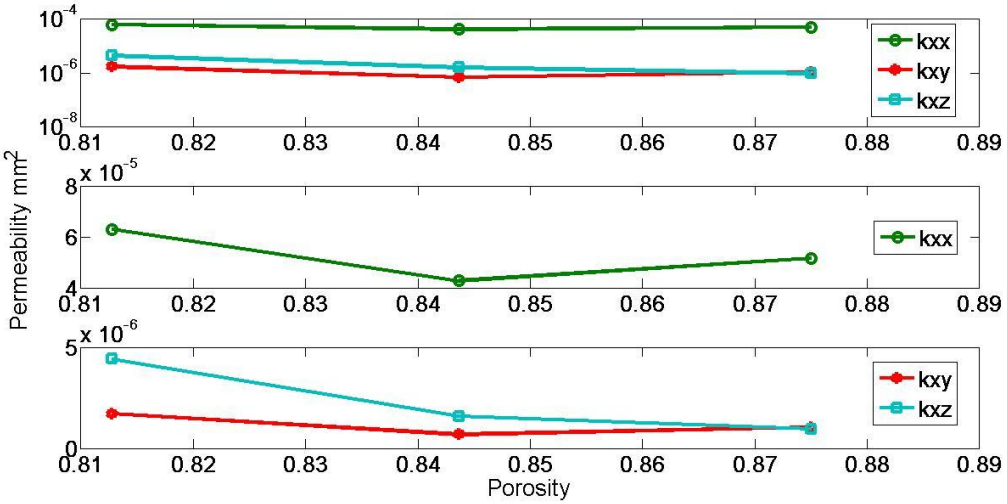

Figure 4. 12 The simulated permeability components when fluid flows in the x direction

For the carbon paper GDL, we simulated the three samples with porosity of 0.81, 0.84 and 0.87, respectively. Figures 4.10-4.12 show the simulated permeability for each sample when the pressure gradient was applied in the three different directions. The result shows that for the carbon GDL, its permeability in the principal direction is one to two orders of magnitude higher than that in the off-principal directions. This is because the principal directions in the x-ray images were aligned with the direction of the geometrical features of the GDLs with the *z* direction pointing to the through-plane direction.

When gas flows in the through-plane direction from the gas-supply channel towards the catalyst layer, the permeability in the principal direction and in the two off-principal directions is $3.02\times10^{-5} mm^2$, $0.189\times10^{-5} mm^2$ and $0.0533\times10^{-5} mm^2$ respectively. The degree of the anisotropy of the GDLs is calculated as the ratio between the permeability in the principal direction with that in the off-principal directions [109]. The results indicated that the degree of anisotropy of the carbon paper GDL is influenced by the local structure.

4.4 Performance of the MRT model

In contrast to the BGK model, there is no limitation to the relaxation time parameters in the MRT model, and the computational cost of MRT model is independent of the relaxation time parameters. Similarly, we test the model against the glass beads first and then apply to the GDLs.

4.4.1 Test of the model against glass beads

To validate the MRT model, we simulated fluid flow through the glass bead column. The simulation results was compared with the measured permeability given in Chen et al [102].

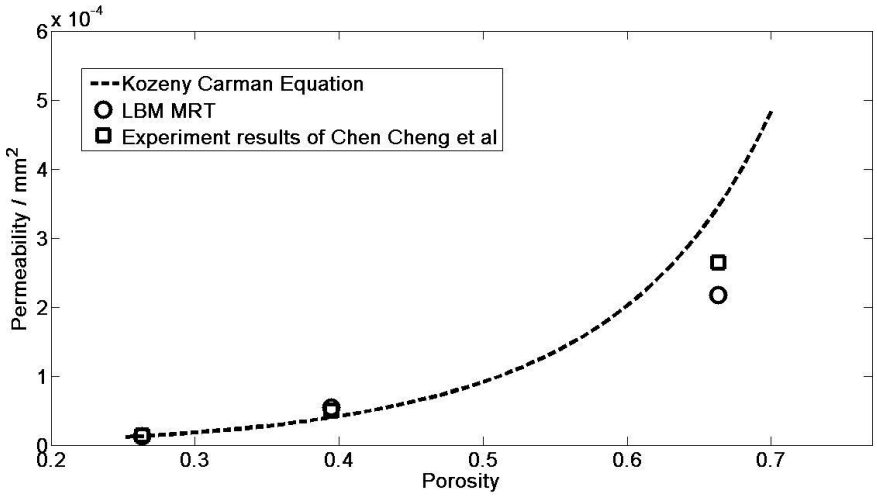

Figure 4.13 Comparison of the simulated permeability with the experimental measurement reported in Reference [102] and the K-C equation prediction.

The relationship between the porosity and permeability obtained from the MRT simulations was evaluated for the images using sub-domains with dimension of $0.96\times0.96\times0.96\,\mathrm{mm}^3$. The increase of the permeability with porosity in the range from 0.2 to 0.6 is shown in Figure 4.13. We also compared the simulated permeability with the experimental measurements reported in Chen et al [102], and the results show a good agreement. The permeability predicted using Kozeny-Carman (K-C) equation is also shown in the figure.

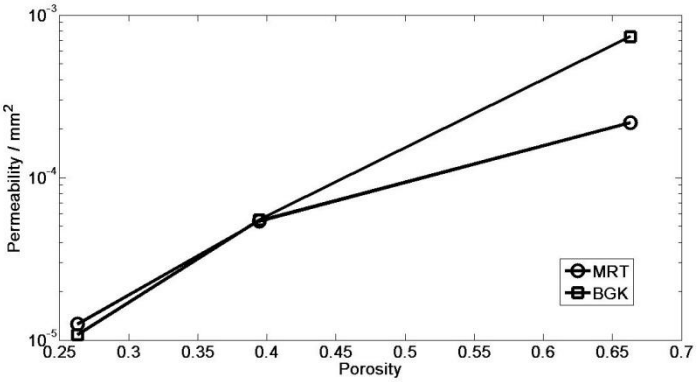

Figure 4. 14 Comparison of the permeability calculated by BGK and MRT models

Figure 4.14 compares the permeability calculated by the BGK and MRT models, both using unity relaxation parameter. It is evident that the two models gave very close results

when the porosity is low. With an increase in porosity, however, the permeability calculated by the BGK model becomes higher than that by the MRT model; this is because with an increase in porosity, the pores become bigger and the velocity increases. As a result, the errors of the BGK model in resolving the solid-fluid boundary might have become increasingly significant.

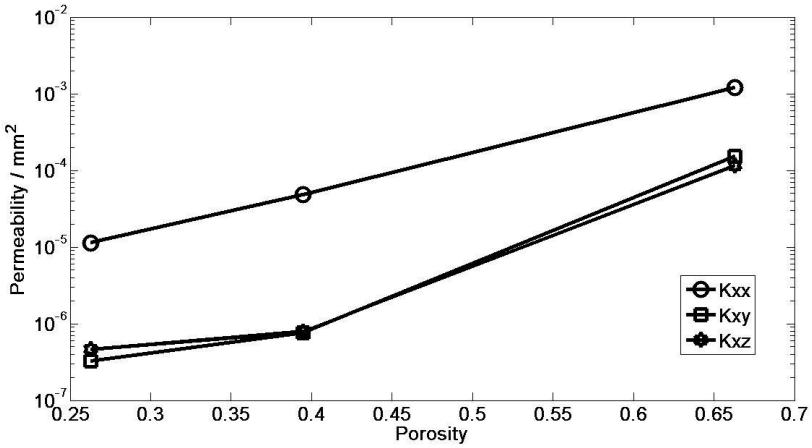

Figure 4. 15 The simulated permeability components when fluid flows in the x direction.

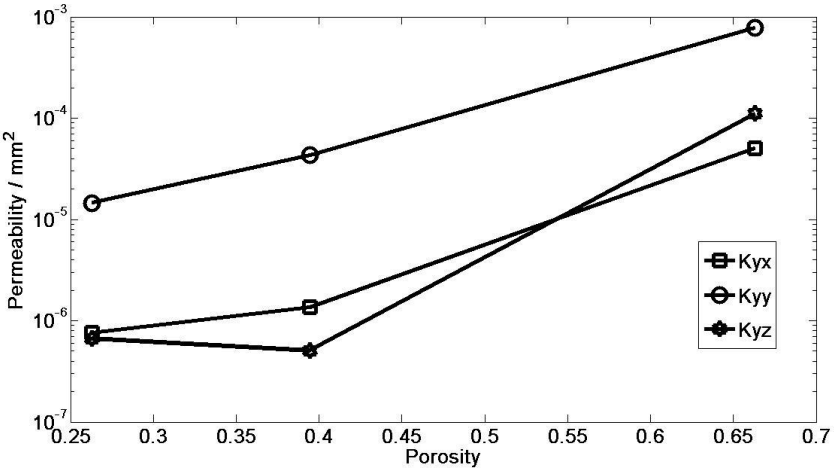

Figure 4. 16 The simulated permeability components when fluid flows in the y direction.

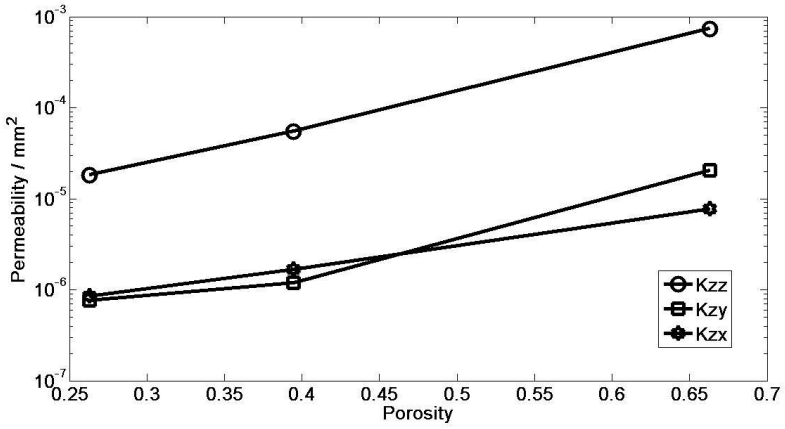

Figure 4. 17 The simulated permeability components when fluid flows in the x direction.

Figures 4.15-4.17 show the simulated anisotropic permeabilty when the pressure gradient is applied in the three principal flow directions. The permeability in the principal direction is one to two order higher in magnitude than that in the off-principal directions. For all the three samples, the permeability in the three principal directions are very close. This was expected as the packing of glass beads investiagted in this paper is quite uniform and there is no obvious structural anisotropy.

4.4.2 Permeability of the carbon paper GDL

The microstructures of a carbon paper GDL were shown in the above figure. The MRT model is used to calculate the velocity and pressure distribution. The simulated velocity at pore scale is used calculate the anisotropic permeability. They are then compared with the BGK results.

4.4.3 Velocity and pressure distribution

Flow in both the in-plane and through-plane directions was simulated by applying a constant pressure gradient in the in-plane and through-plane directions, respectively. As an illustration, Figure 4.18 shows the 3D velocity and pressure distributions in the GDL obtained from the MRT model for Sample 1. It can be seen that due to the heterogeneous structure of GDL, the flow field in it is complicated. The velocity field shows that the main flow paths were through larger pores because of their less resistance. Figure 4.19 shows the fibrous structure and the iso-surfaces of the velocity at different simulation times before the flow reached steady state.

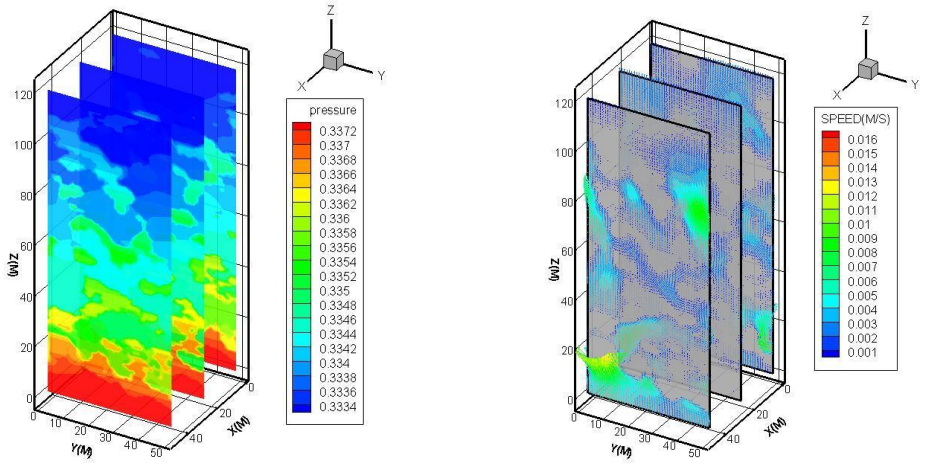

(a) (b)

Figure 4. 18 The Simulated pressure slices in the GDL (a), and the velocity slices (b).

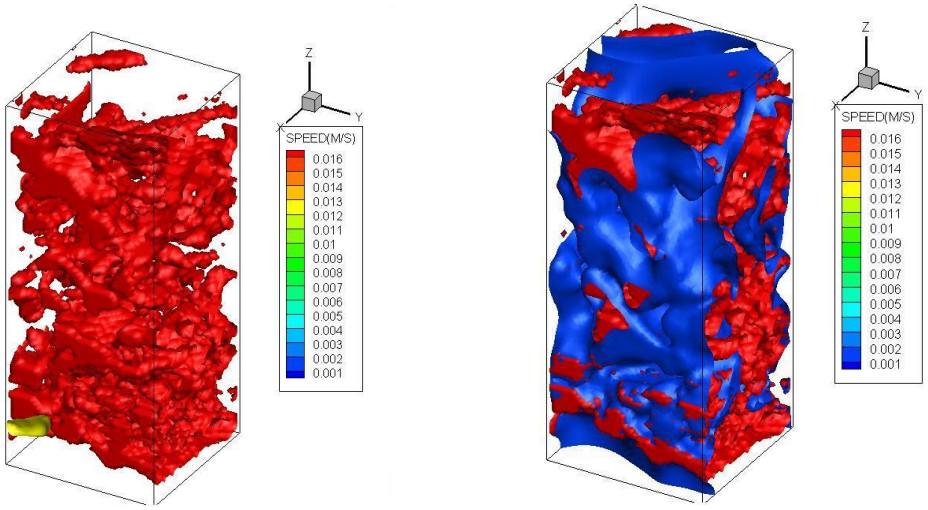

(a) (b)

Figure 4. 19 The iso-surfaces of the simulated velocity after 1000 time steps (one step is approximately two seconds), 10000 time steps (b).

4.5 Permeability- porosity relationship

The value of the permeability of a porous medium depends on its pore geometry. In practice, the permeability is often expressed as a function of some easy-to-measure physical properties, such as porosity and tortuosity. Although the porosity and the connectedness of the pores in a porous medium control the ability of the medium to transfer fluids, the relationship between them is difficult to derive because of the

complexity of the pore geometry. Most formulae used to estimate the permeability from the porosity are empirical; one of such formulae is the Kozeny-Carman (K-C) equation [104], which relates the permeability of a medium to its porosity, specific surface and tortuosity as follows:

$$k = \varphi^3 / bs^2 \upsilon^2 \tag{4. 11}$$

where b is a geometric constant, φ is porosity defined as the pore volume in an unit volume of medium, s is the specific surface defined as the solid-void interface area in an unit volume of medium, and υ is the tortuosity defined as the ratio between the length of mean fluid flow path in the flow direction and the real distance that the fluid particles has travelled.

The K-C equation was originally derived for granular porous media with low porosity. As such, it might fail to predict the permeability of fibrous media, such as the GDLs. Tomadakis and Robertson [110] proposed a modified formula to predict the permeability of carbon paper GDLs with randomly overlapping fibre structures as follows:

$$K = C \frac{\varphi^3}{\left(\ln \varphi\right)^2} \tag{4. 12}$$

where $C = 8.9504 \times 10^{-13}$ for the channel-membrane direction (in-plane direction) in the GDLs and $C = 6.2805 \times 10^{-13}$ for the through-plane direction (perpendicular to the in-plane direction) in GDLs [33].

Most carbon GDLs are made either by pressing chopped carbon fibres into a paper or by weaving a bundle of fibres into a cloth. Tomadakis and Robertson [110] used the earlier random walk simulation results by Tomadakis and Sotirchos [111], in conjunction with an electrical conduction-based theory, to derive the following equation for the dimensionless viscous permeability of random fibrous media.

$$\frac{k}{r^2} = \frac{\varepsilon}{8 \ln^2 \varepsilon} \left(\frac{\varepsilon - \varepsilon_p}{1 - \varepsilon_p} \right)^a \left(1 + \frac{\alpha \varepsilon}{\varepsilon - \varepsilon_p} \right)^{-2} \tag{4. 13}$$

where r is the fibre radius, ε is the porosity, ε_p is the percolation threshold (i.e., the porosity value below which the medium is no longer permeable), and α is an Archie's law parameter. For structures of morphology similar to that of GDLs, Tomadakis and

Sotirchos [111] derived ε_p equal to 0.11, and α equal to 0.521 for the in-plane and 0.785 for the through-plane flow. The predictions of Equation (4.13) are in very good agreement with numerous experimental measurements of the viscous permeability of fibrous media [111], and have also been validated experimentally by other researchers, including the studies of Gostick et al [112]. Tomadakis and Robertson [110] also showed that for random non-overlapping fibre structures, the popular Kozeny-Carman relation is in the form of

$$\frac{k}{r^2} = \frac{\varepsilon^3}{4K_c(1-\varepsilon)^2} \tag{4. 14}$$

where K_c is the Kozeny constant, which depends on both the porosity and the geometry of the pore channels. Therefore the value of K_c is adjusted based on experimental or simulation measurements.

Figure 4.20 compares the simulated through-plane permeability (in the z direction) with the predictions by Equations (4.13) and (4.14). Good agreement is observed with the equation derived by Tomadakis and Robertson [110]. Good agreement is also obtained with the Kozeny-Carman equation when using a best-fit value of K_c =6.5. The fibre diameter in our studies is $7.5\mu m$. The simulated permeability in the x and y directions (in-plane) is considerably higher than the theoretical predictions. The reason for this deviation was demonstrated by Gostick [26]; this could be due to the spatial correlation of pores sizes. Introducing a spatial correlation of pores into the model could increase the permeability by more than 20% because when pores are correlated in a direction, the permeability in this direction is likely to increase because of formation of channels.

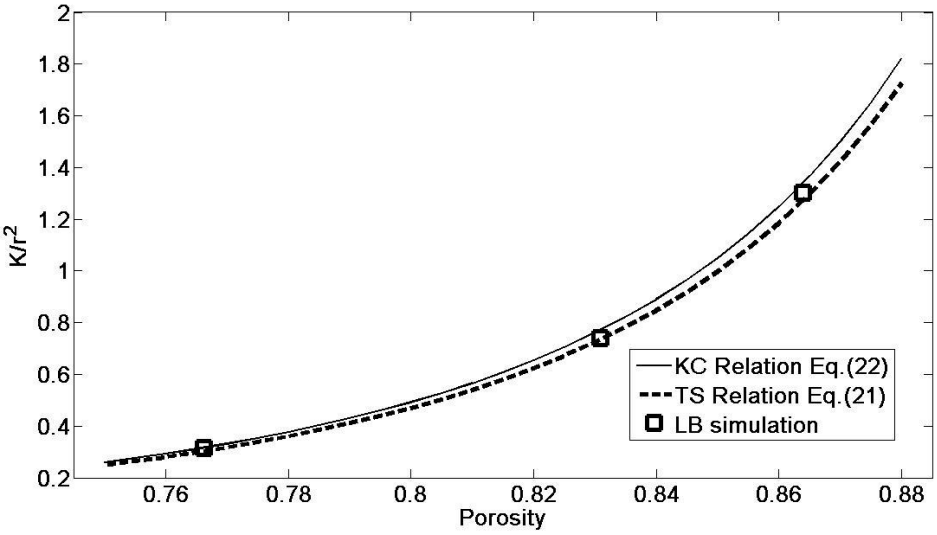

Figure 4.20 The comparison of simulated dimensionless permeability with the predictions of T-S equation and K-C relation.

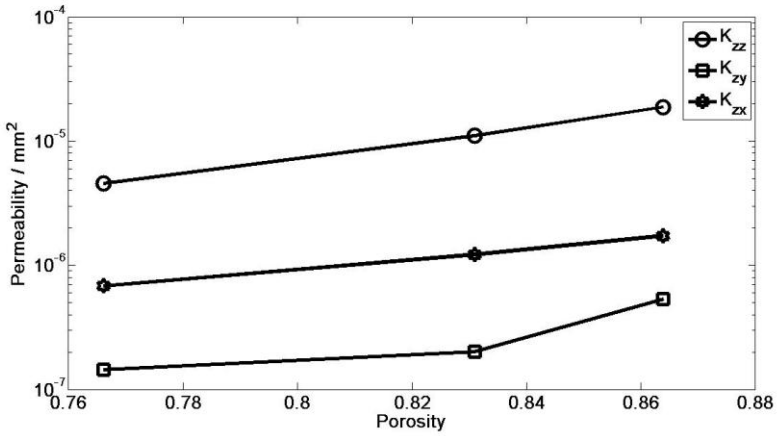

Figure 4. 21 Change of permeability with porosity when fluid flows in the z direction.

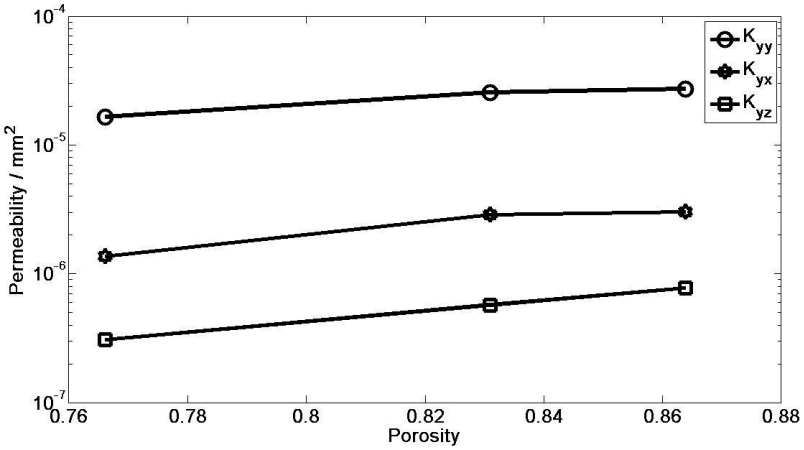

Figure 4. 22 Change of permeability with porosity when fluid flows in the y direction.

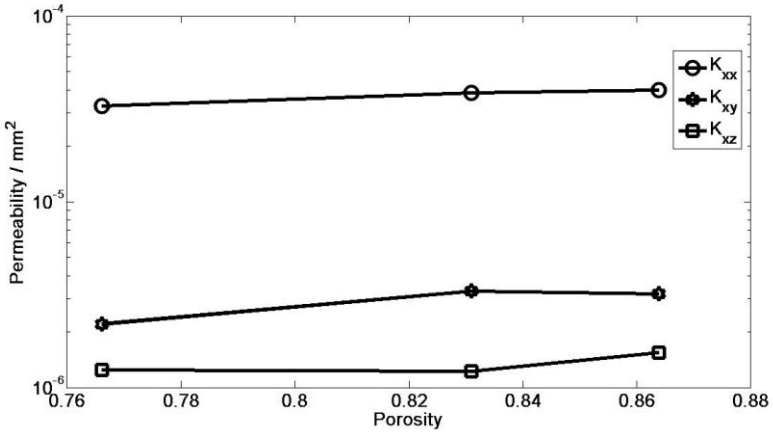

Figure 4. 23 Change of permeability with porosity when fluid flows in the x direction.

Figures 4.21-4.23 show the simulated permeability when the pressure gradient was applied to each of the three principal directions, respectively. The figure shows that the permeability in the flow direction is in the range of 10^{-12} to $10^{-11} m^2$, consistent with the result of Gostick et al [112]. For both in-plane and through-plane directions, the simulated permeability in the principal directions is approximately two orders higher in magnitude than that in the off-diagonal directions, indicating that when a pressure difference is applied to the mean flow direction, the fluid also flows in other two directions but at a much slower rate. Figures 4.22 and 4.23 also indicated that the simulated permeability in the two in-plane directions (the x and y directions) are comparable for the high-porosity samples, but higher than the permeability in the through-plane direction due to the anisotropic structures of the GDL. For the low porosity sample, the principal permeability components in the x and y directions differ; this could be due to the size of the sample which is not big enough to be representative. In all the simulations, the value of the permeability in the off-principal directions is approximately two-order smaller in the magnitude than the permeability in the principal direction. This is expected because the principal directions in the simulations (the mean pressure directions) are in parallel with the in-plane and through-plane directions.

4.6 Comparison of the BGK and MRT models

Figures 4.24-4.26 compare the permeability calculated by BGK and MRT models for Sample 1. All the BGK simulations used a unity relaxation time parameter, which represents a best compromise between computational cost and solution accuracy. The difference between the permeability calculated by the two models in the in-plane direction is considerable, whilst the permeability calculated by them in the through-plane direction is comparable. This might be due to that the flow rate in the through-plane direction is slower than the flow rate in the in-plane directions as shown in the figures. As a result, the errors of the BGK model in solving fluid-solid boundary in the through-plane direction are not as significant as in the in-plane direction.

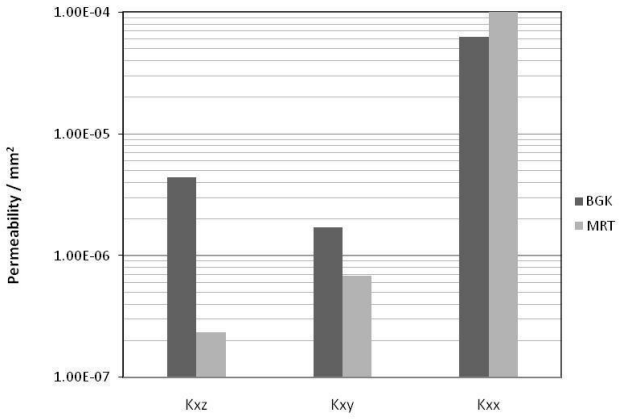

Figure 4.24 Comparison of the simulated permeability components by BGK and MRT models when flow is in the x direction

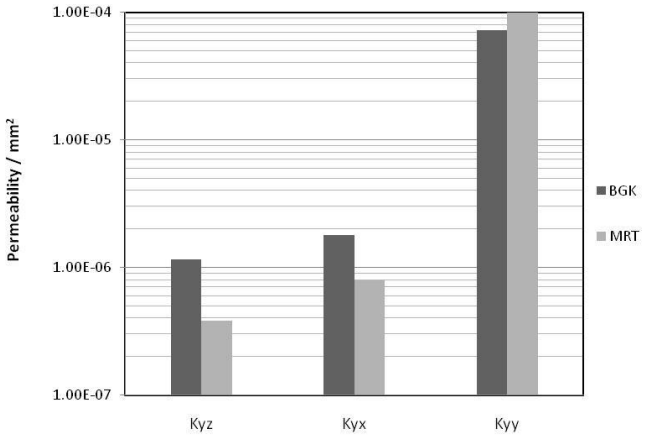

Figure 4.25 Comparison of the simulated permeability components by BGK and MRT models when flow is in the x direction

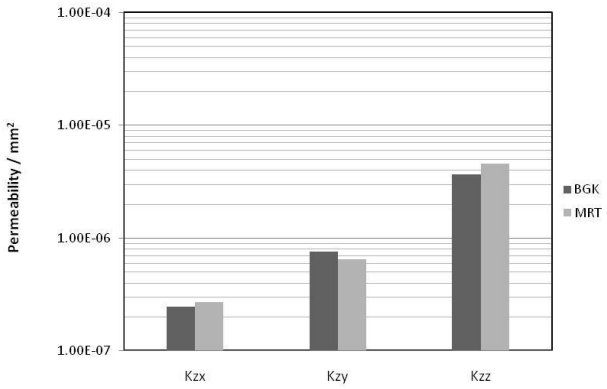

Figure 4.26 Comparison of the simulated permeability components by BGK and MRT models when flow is in the z direction

4.7 Comparison of BGK and MRT permeability calculated using different viscosities

The attractiveness of the BGK model, coupled with the bounce-back method to treat the fluid-solid boundary, is its simplicity and computational efficiency. The drawback is its inaccuracy for calculating the location of the fluid-solid interface. Such errors vary with the relaxation time parameter. Since the relaxation time is related to gas viscosity, the BGK model could give rise to a permeability which changes with gas viscosity.

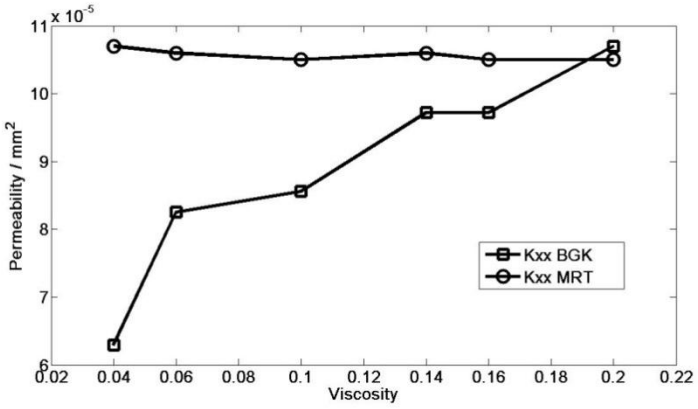

Figure 4.27 Comparison of the permeability computed by BGK and MRT models using fluids with different viscosities when fluid flows in the x direction

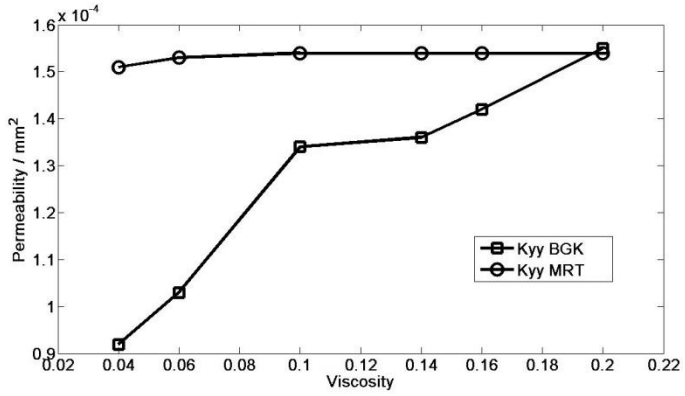

Figure 4.28 Comparison of the permeability computed by BGK and MRT models using fluids with different viscosities when fluid flows in the y direction.

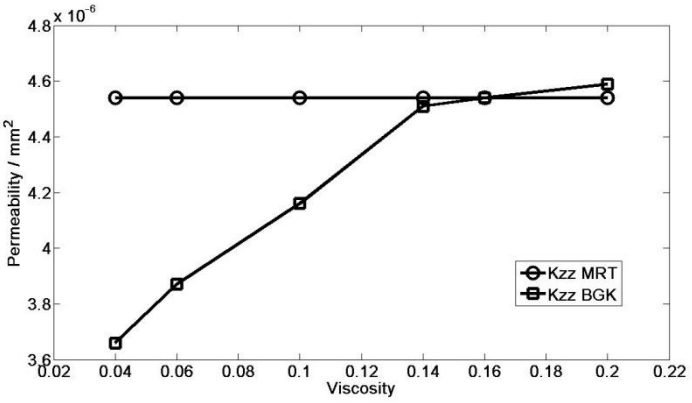

Figure 4.29 Comparison of the permeability computed by BGK and MRT models using fluids with different viscosities when fluid flows in the z direction.

To prove that the MRT model overcomes this problem, Figures 4.27 -4.29 compares the permeability simulated using fluids with different viscosity by the BGK and MRT models. For both models, the dimensionless viscosities of $\mu=(\tau-0.5)/3$=0.04, 0.06, 0.10, 0.14, 0.16 and 0.20 were used. The results show that the permeability calculated by the MRT model with different viscosities is almost the same, whilst the permeability calculated by BGK model increases unrealistically with fluid viscosity. The reason why the permeability calculated by the MRT model is independent of fluid viscosity is because it accurately solved the solid-fluid boundary.

4.8 Tortuosity

One important feature of porous media is their tortuosity. In this work, the tortuosity is defined as the ratio of the length of the path along which the fluid particles move to the

averaged distance that the fluid particles travel in the pressure-gradient direction. Since the GDL is anisotropic, its tortuosity also varies with flow direction and is calculated based on the method used by Nabovati et al [113]. When the pressure drop was applied in the *x* direction, the tortuosity in the *x* direction is

$$\tau_x = \frac{\sum_i u_{ave}(\boldsymbol{x}_i)}{\sum_i |u_x(\boldsymbol{x}_i)|} \tag{4. 15}$$

when the pressure drop was applied in the *y* direction, the tortuosity is

$$\tau_y = \frac{\sum_i u_{ave}(\boldsymbol{x}_i)}{\sum_i |u_y(\boldsymbol{x}_i)|} \tag{4. 16}$$

when the pressure drop was applied in the *z* direction, the tortuosity is

$$\tau_z = \frac{\sum_i u_{ave}(\boldsymbol{x}_i)}{\sum_i |u_z(\boldsymbol{x}_i)|} \tag{4. 17}$$

In the above equations, u_{ave} was calculates from

$$u_{ave}(\boldsymbol{x}_i) = \sqrt{u_x(\boldsymbol{x}_i)^2 + u_y(\boldsymbol{x}_i)^2 + u_x(\boldsymbol{x}_i)^2} \tag{4. 18}$$

We calculated the tortuosity in each direction based on the pore-scale velocity simulated using the MRT model. The decrease of the tortuosity with porosity is shown in Figure 4.30. Whilst the tortuosity in all the three directions decreases as the porosity increases, the tortuosity in the z direction decreases faster than that in the x and y directions.

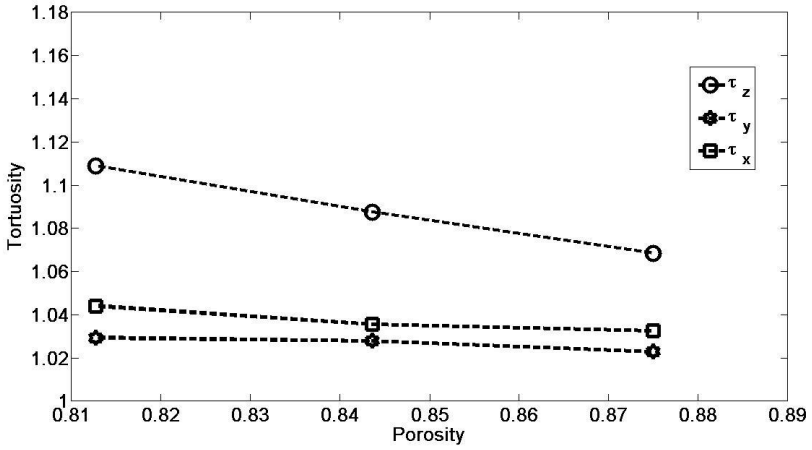

Figure 4.30: The change of tortuosity with porosity in all the three directions

4.9 Conclusions and discussion

In this chapter we used a combination of X-ray computed tomography and the lattice Boltzmann method to investigate the anisotropic permeability of a pack of glass beads, carbon paper and carbon cloth gas diffusion layers. The results indicated that the calculated permeability for the glass beads was close to the measurement. For both media, the change of the calculated permeability with porosity can be well described by the Kozeny-Carman equation.

Most GDLs are anisotropic in that their ability to conduct gas in the in-plane direction differs from that in the through-plane direction. Knowing such anisotropy is essential to understand how the gas flow from the gas channels to the catalyst layers, and hence to improve fuel cell performance. The 3D micro-structures of the GDL were obtained using an x-ray computed tomography at a resolution of 1.76 μm, and the gas flow through the micro-structure was simulated by single-relaxation time and the multiple-relaxation time lattice Boltzmann models. The anisotropic permeability was calculated from the simulated velocity field by applying a pressure gradient in the through-plane and the in-plane directions respectively. To validate the methodology, we applied it to simulate fluid flow in a column packed with glass beads, and the results show close agreement with the experimental measurements.

The multiple-relaxation time lattice Boltzmann method can overcome the inaccuracy of single-relaxation time lattice Boltzmann model in solving for the solid-fluid boundary. To

demonstrate the improvement, we compared the permeability calculated by both BGK and MRT models using different viscosities and show that the permeability calculated by the BGK model using different fluids increases with fluid viscosity. In contrast, the permeability calculated by the MRT model using different fluids is almost constant.

Table 4. 3 Efficiency of the MRT and BGK models

	CPU time(s)		**Permeability ($\tau = 1$)**	
	BGK	**MRT**	**BGK**	**MRT**
Sample 1	0.036×10^{5}	0.15×10^{5}	5.78×10^{-6}	7.72×10^{-6}
Sample 2	0.108×10^{5}	0.864×10^{5}	1.90×10^{-6}	1.81×10^{-6}
Sample 3	0.216×10^{5}	1.512×10^{5}	3.02×10^{-6}	3.20×10^{-6}

In terms of calculating permeability, the single-relaxation time method might be more competitive by using unity relaxation time. The performance of the two methods is compared in Table 4.3 and the permeability of Sample 1 to 3 is chosen from the above figure. The MRT model needs almost five times the CPU time as the BGK model, but the calculated permeability by the two methods is very close. Here, we like to address that it is pointless to compare the absolute accuracy of the two methods as both the experimentally measured permeability and the images of acquired by the x-ray computed tomography bear errors and such errors are impossible to quantify.

The simulated results for the GDL revealed that in both the in-plane and through-plane directions, the gases move only along a few channels due to the heterogeneous structure of the GDL. The calculated permeability shows strong anisotropy in that the permeability in the in-plane direction is considerably larger than the permeability in the through-plane direction. The permeability calculated for the GDL with different porosity can be fitted by the K-C equation using a curve-fitting parameter. We also compared the simulated permeability to the predictions of the T-S equation [110] that does not need fitting-parameters, and the results show a good agreement for the through-plane permeability. In the in-plane direction, however, the simulated permeability is higher than the predictions of the T-S equation because of a possible spatial correlation of the pores in our GDLs. We also calculated the tortuosity of the GDL in the all three directions; the results indicated that in all the directions the tortuosity inversely increases with the porosity; however, the tortuosity in the through-plane direction decreases faster than in the in-plane tortuosity.

The methodology and results presented in this chapter provide an alternative to investigate gas flow in the GDLs and the catalyst layers. As imaging technology becomes increasingly accessible, combining it with numerical simulations will enable us not only to estimate the macroscopic transport parameters such as permeability and diffusivity of the GDLs, but also to understand the detailed flow paths at micron scale when the gases move from the gas channels to catalyst layers, which remains unknown but is important to understand the impact of heterogeneous pore structures on fuel cell performance. This will help fuel cell design and improve the fuel cell performance.

Chapter 5 Impact of compression on GDL permeability

5.1 Introduction

Previous chapters introduced the mechanisms of PEM fuel cells. The output of the power of a single cell is limited, and to increase its power, a number of cells are often stacked to make a fuel cells assembly in practical applications. In a fuel cell assembly, each membrane electrode assembly (MEA), which consists of GDLs, catalysts layer and the electrolyte membrane, is sandwiched by the two bi-polar plates. The MEA is then subsequently bolted together under a certain clamping pressure to seal gas leakage and reduce the interfacial resistances between GDLs and catalyst layers, catalyst layer and membrane, and GDLs and the bipolar plates. This will result in a compression to the MEA. Since the catalyst layer and the membrane have much higher electrical modulus (typical 100 MPa) than the GDLs (typical 10 MPa), their elastic deformation can be neglected.

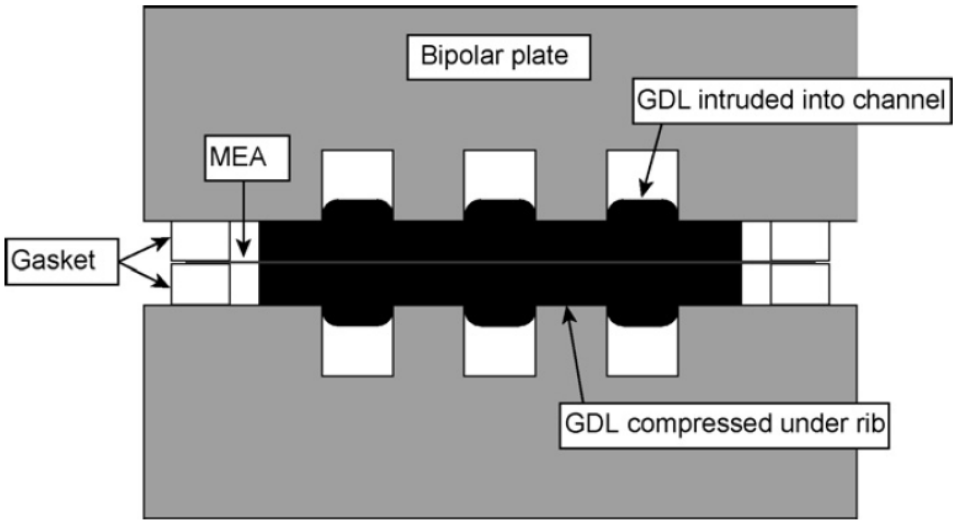

Figure 5.1 Schematic illustration of GDL compression (Courtesy to Iwao Nitta 2007).

Figure 5.1 shows MEA compression in a fuel cell assembly. The compressive pressure to which the MEA is subjected depends on the gaskets. During clamping, the GDL under the rib will be compressed to the thickness of the gasket, whereas the GDL under the channel remains almost uncompressed. This inhomogeneous compression makes the transport properties of the GDL vary, with the ability of the GDL under the rib to conduct gases considerably reduced [114]. Such heterogeneity could make the reactant gases flow not

only in the through-plane direction but also in the in-plane direction from one channel to another. The impact of such compression on gas flow and the consequent fuel cell performance has attracted increased attention over the past few years [115]. For example, the work of Bazylak et al.[116]showed that GDL degradation due to compression could lead to preferential water flow, and their scanning electron microscopy clearly showed that the compression results in breakup of fibres and deterioration of hydrophobic coating. For the impact of compression on fuel cell performance, the study of Escribano [117] revealed that a 20% decrease in the compression of the GDL allows to decrease strongly the local pressure in the active zone while increasing significantly the performance at high current density. The compression of GDL is not uniform, with the area between channel-rib and the membrane being subjected to higher compressive pressure than other areas. The work of Nitta et al [118] indicated that such an inhomogeneous compression could lead to a significant variation in the ability of GDL to conduct both gases and charges. Lee et al, investigated the effect of bolt torque on cell performance for a range of commercially available GDL with the thickness from 203 to 508 μm [119]. Their results showed that the internal pressure increased with GDL thickness for a given bolt torque. Cells configured with the thinnest GDL and thickest GDL experienced internal pressures between 1.6-2.0 MPa and between 8.4-9.7 MPa, respectively. Ge et al. identified the existence of a threshold level of compression which results in optimal cell performance for woven and non-woven GDLs [115]. Lin et al used different gasket thicknesses to control compression and concluded that a compression ratio of 59-64% for two woven GDLs of 320 μm and 460 μm thicknesses resulted in optimal cell performance [120]. Lee et al, investigated inhomogeneous compression across the footprint area of a single cell using a 500 μm thick GDL and measured average pressures of 13.2-47.7 MPa [121]. Chi et al. carried out a numerical investigation to calculate the effect of GDL compression ratios in the range of 36.0-60.5 % on temperature, saturation and oxygen distribution across the footprint of the GDL by accounting for its compressed porosity [122]. Their results indicated that high compression ratios could increase saturation, reduce current densities and invoke greater temperature differences. The study of Zhou et al also demonstrated that GDL compression can reduce contact resistance and hinder the transport of reactants and liquid water [123]. The ex-situ investigation of Bazylak et al [116] demonstrated that highly compressed region of the GDL will experience the most

aggressive morphological change and result in a loss of hydrophobicity. In general, compression improves electrical and thermal conductivity, but reduces fluid permeability.

The compression could also make the GDL more anisotropic in that its ability to transfer fluids in the through-plane direction differs significantly from the in-plane direction. Therefore, understanding the change of the anisotropic permeability of GDLs under different compression is important to improve our understanding of how compression could affect gas flow and the consequent fuel cell performance. This has received increasing attention over the past few years.

The earlier experimental measurement of GDL permeability focused on uncompressed GDL [124], and over the past few years there has been an increased interest in the impact of compression on GDL permeability. For example, Gostick et al [112] investigated the reduction of permeability due to compression in both in-plane and through-plane directions; they found that compressing a GDL to a half of its original thickness in the through-plane direction could reduce its permeability by one order in magnitude. Similar results were also found for relative permeability of GDL to both gas and liquid water when GDLs are partially filled with liquid water [125]. Other research on the impact of compression on GDL permeability includes the work of Mathias et al [6] and Gurau et al [126].

The previous work on compression focuses on its impact on averaged flow, which is characterised by GDL permeability. As stated before, in fuel cell design, knowing the averaged flow transport processes might not be sufficient as the electrochemical reactions take place at pore scale and at solid-void interfaces where the catalysts are present. Therefore, a detailed knowledge of fluid flow paths at pore scale in the GDL is also important and can offer more help in fuel design.

Technology had been developed by our research group to visualise the change of pore geometry of GDL when it is subjected to compressive pressures from 0.1 Mpa and 20 MPa. The objective of this chapter is to investigate how the compression will change the GDL permeability in both through-plane direction and in-plane direction, and the detailed fluid flow paths in the GDLs. Also, we demonstrated in Chapter 3 that the BGK lattice Boltzmann model could give a good result if the relaxation time parameter was carefully

chosen. Another objective of this chapter is to see if such an optimal relaxation time parameter for the BGK is a constant and independent of pore structures in the GDLs.

5.2 X-ray imaging of compressed GDLs

The tested GDLs are woven cloth. The x-ray computed tomography used in this project cannot visualize in-situ structural change of the GDL during compression. In order to capture the structure of the GDL when it was compressed, the pore geometry needs to be permanently set in that state using an inert compound prior to X-ray tomography.

A special technology is then developed. The GDL was first compressed under the desired pressure. The compressed GDL was then saturated with polydimethylsiloxane (PDMS) and then heat-treated at 333 K while under the compression to set it in its compressed state. PDMS is a silicone-based organic polymer which has s specific density of 1.03 at room temperature and cures at the above temperature to form a flexible elastomer. Both sides of the sample are covered with protective thin aluminium sheets before being flat-pressed to ensure that the samples can be easily removed after curing. The weight is preselected in order to achieve a given uniform compression pressure which is representative of those experienced in operational fuel cell stacks. As the current study focuses on a range of compressive loads, a corresponding number of PDMS-set samples are generated for digital reconstruction. Figure 5.2 shows a flat pressed 1×1 cm^2 GDL sample cured under a weight of 10 kg.

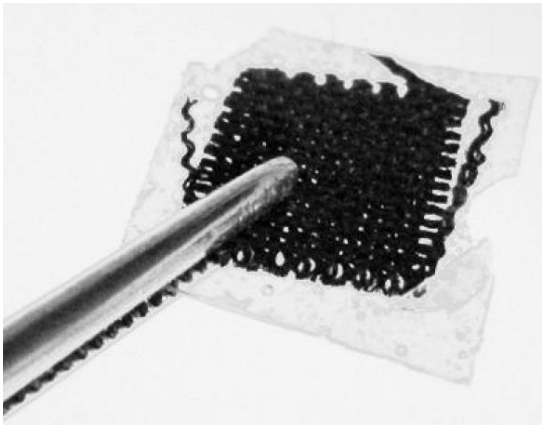

Figure 5.2 Compressed carbon cloth GDL sample cured with PDMS

After the sample preparation, the other four procedures for imaging the sample are the same as that explained in Chapter 2, which involves x-ray micro-tomography, image

processing, digital reconstruction and material selection. The thickness of the GDL reduced from 372 um to 147 um when the compressive pressure increases from 0.1 MPa to 20 MPa, and the associated porosity decreased from 60% to 36%. There is little change in the thickness when pressure increased from 0.l MPa to 1.0 MPa, indicating that the GDL can withstand compression in this range. Also, when pressure increased to 100 MPa, there is a significant change in structure, and the fibrils might have been broken.

As a comparison, Figure 5.3 show the 3D image of the reconstructed uncompressed GDL with size of $693.2\times519.9\times372.6$ μm^3. For lattice Boltzmann simulation, the original image was further divided to 4 regions, which are shown in Figures 5.3 (b)–(e). The size of the each region is listed in Table 5.1. In Figure 5.3 and what follows, the through-plane direction is assumed to be the z direction.

Figure 5.4 (a) shows the compressed GDL image under compressive pressure of 0.3 MPa. Its size is $693.2\times519.9\times242.6$ μm^3. Again, the reconstructed image was divided into four regions, and the details of each region are listed in Table 5.2. Similarly, Figure 5.5 Figures 5.6 show the compressed GDL image under compressive pressure of 20 MPa and the four divided regions, and the details of each region is given in Table 5.3.

Table 5. 1 The size of each of the four regions for the uncompressed 3D GDL

GDL	**Image size in voxels** (Lattice unit)			**Image size** (μm)			**Pixel size** (μm)	**Porosity** ε_0
	X	*Y*	*Z*	*X*	*Y*	*Z*		
Whole size	400	300	215	693.2	519.9	372.6	1.733	0.810193
Region 1	100	300	215	173.3	519.9	372.6	1.733	0.791788
Region 2	100	300	215	173.3	519.9	372.6	1.733	0.819372
Region 3	100	300	215	173.3	519.9	372.6	1.733	0.838417
Region 4	100	300	215	173.3	519.9	372.6	1.733	0.791195

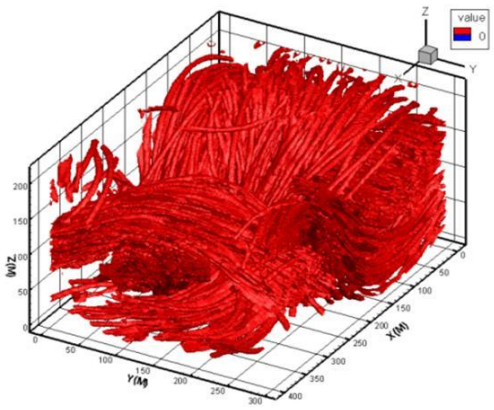

(a)

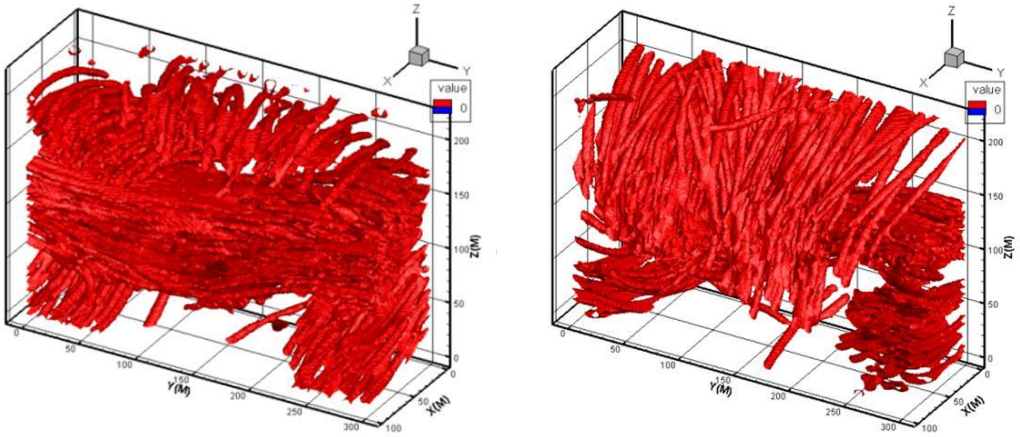

(a) (c)

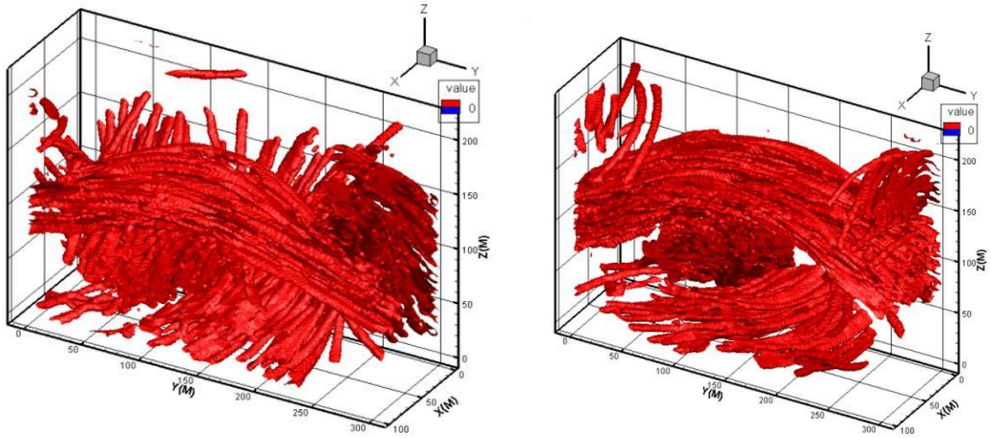

(d) (e)

Figure 5.3 The uncompressed GDL (a), and the four sub-regions (b-e) used for simulations.

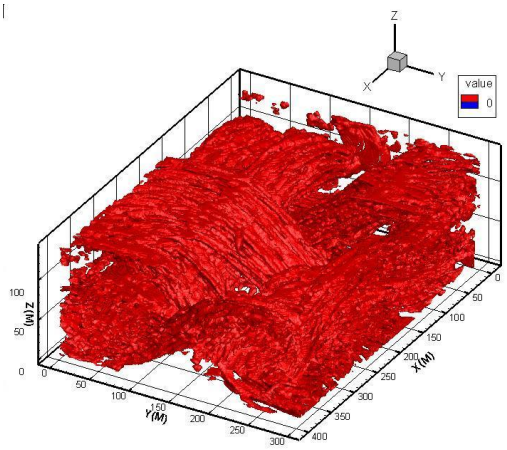

(a)

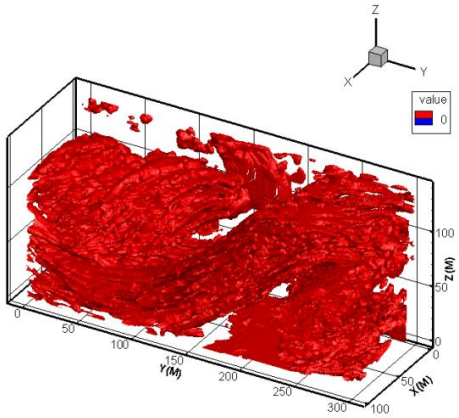

(b)

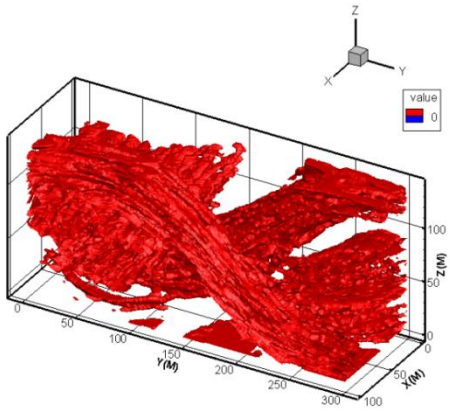

(c)

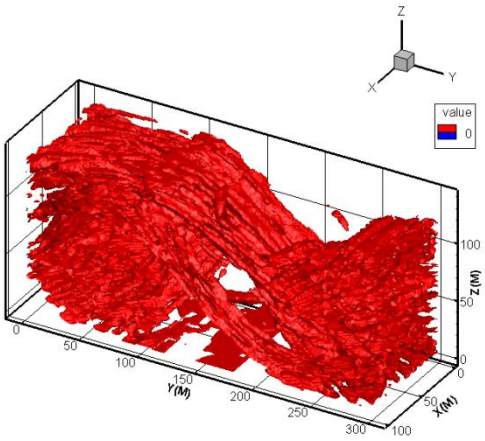

(d)

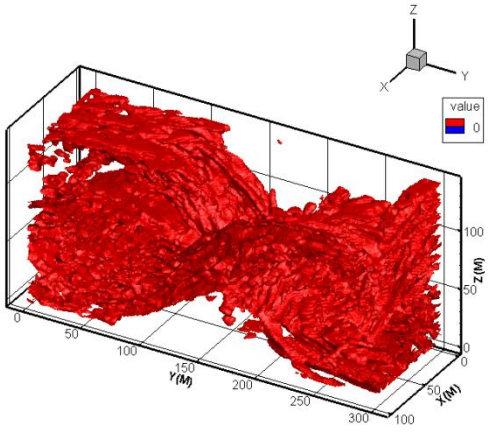

(e)

Figure 5.4 The compressed GDL image under 0.3MPa (a), and the regions (b-e) for simulations.

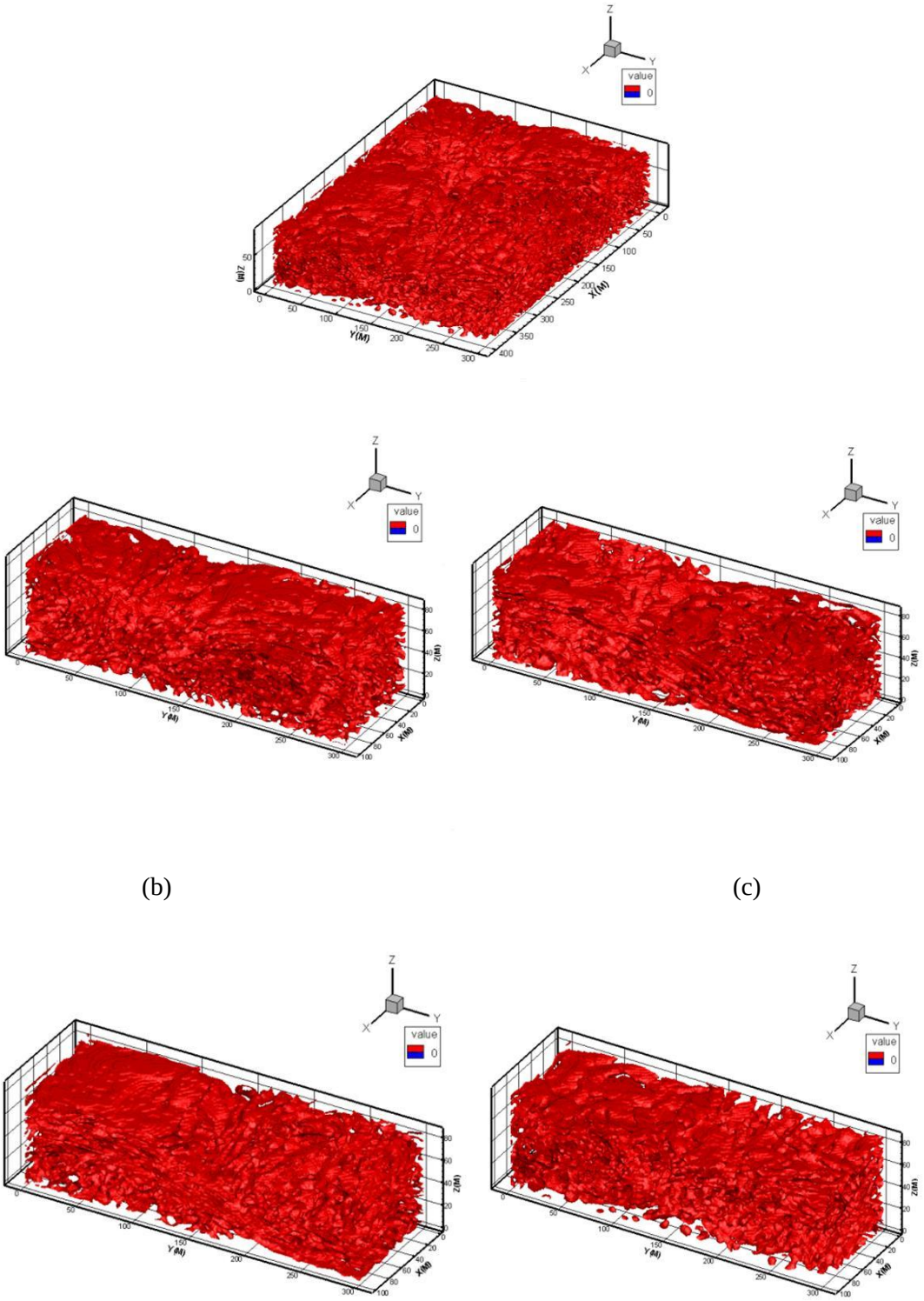

(b) (c)

(d) (e)

Figure 5.5 The compressed GDL image under 20MPa (a), and the regions (b-e) for simulations.

Table 5. 2: The size of each of the four regions for the compressed 3D GDL under 0.3Mpa

GDL	Image size in voxels Lattice unit			Image size (μm)			Pixel size μm	Porosity ε_c
	X	*Y*	*Z*	*X*	*Y*	*Z*		
Whole size	400	300	140	693.2	519.9	242.6	1.733	0.680524
Region 1	100	300	140	173.3	519.9	242.6	1.733	0.638144
Region 2	100	300	140	173.3	519.9	242.6	1.733	0.696367
Region 3	100	300	140	173.3	519.9	242.6	1.733	0.676409
Region 4	100	300	140	173.3	519.9	242.6	1.733	0.711175

Table 5. 3: The size of each of the four regions for the compressed 3D GDL under 20Mpa

GDL	Image size in voxels Lattice unit			Image size (μm)			Pixel size (μm)	Porosity ε_c
	X	*Y*	*Z*	*X*	*Y*	*Z*		
Whole size	400	300	80	693.2	519.9	138.6	1.733	0.51835775
Region 1	100	300	80	173.3	519.9	138.6	1.733	0.521873
Region 2	100	300	80	173.3	519.9	138.6	1.733	0.52337
Region 3	100	300	80	173.3	519.9	138.6	1.733	0.527903
Region 4	100	300	80	173.3	519.9	138.6	1.733	0.520285

5.3 Change of anisotropic permeability with compressive pressure

We simulated gas flow in the above uncompressed and compressed GDLs using both MRT and BGK lattice Boltzmann models. Similar to the simulations presented in Chapter 4, fluid flow is driven by a pressure gradient in one direction of the image. The permeability in this direction was then calculated once flow was deemed to have reached steady state. The permeability in other directions can be calculated similarly.

We simulated the anisotropic permeability of both uncompressed and compressed GDLs using the BGK and MRT models with different relaxation-time parameters. The results are similar; for illustration, we only show the results of Region 1 shown in Tables 5.1 -5.3. Since the relaxation-time parameter in both BGK and MRT is related to viscosity, in what

follows we will use the term of viscosity instead of relaxation-time parameter in discussing the results.

Compression results in a decrease in porosity. This in turn reduces the permeability in both in-plane direction and through-plane direction. In fuel cell assembly, the thickness of the compressed GDL is the same as the thickness of the gasket, and it is hence easy to estimate its reduced porosity due to the compression. In practice, therefore, it is interesting to see if the reduced permeability due to the reduced porosity can be predicted using the empirical formulae introduced in Chapter 4 in both the through-plane and in-plane directions. We fit the simulated permeability of the compressed and uncompressed GDLs to the empirical formulae: the traditional Kozeny –Carman relation and the newly derived relation by Tomadakis and Robertson [110].

Figure 5.6 compares the calculated and predicted permeability in the z direction (though-plane direction), and Figure 5.7 compares the simulated and predicted permeability in the x and y directions (in-plane directions). They agree well. The Kozeny constant K_c in Equation (4.14) is chosen to be 6.8 for K_{zz} and 2.2 for K_{yy} and K_{xx} ; the values of ε_p and α in Equation (4.13) are equal 0.11 and 0.021 for the through-plane direction and in-plane direction, respectively, and 0.11 and 0.685 for the through-plane and in-plane direction, respectively. There are some deviations between the simulations and the predictions; this is possibly due to a slight change in the fibre diameter because of the compression. Such change is neglected in the empirical formulae.

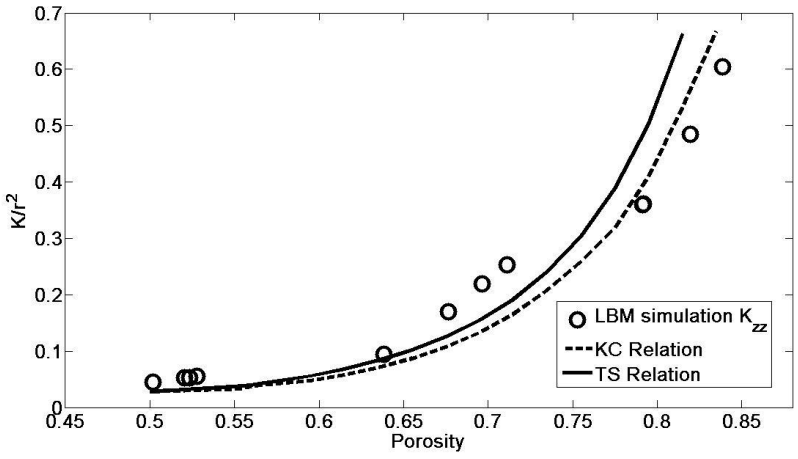

Figure 5.6 Change of the simulated permeability by MRT with porosity with the predictions of TS- and the K-C relations in the through-plane direction

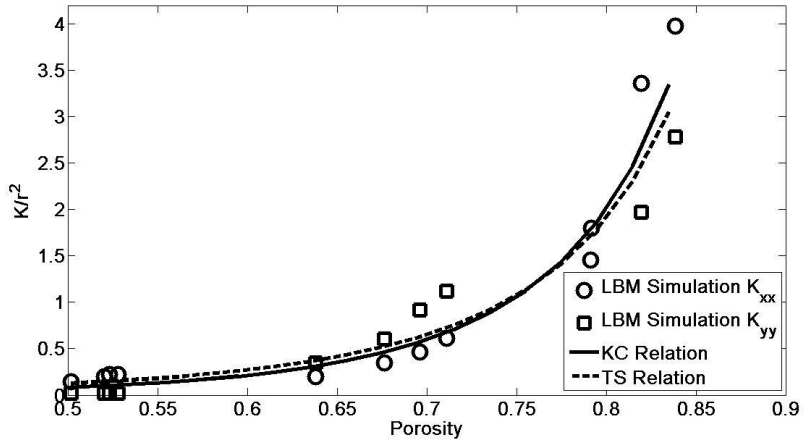

Figure 5.7 Change of the simulated permeability by MRT with porosity with the predictions of TS- and the K-C relations in the in-plane direction

5.4 Comparison of the BGK and MRT models

The BGK lattice Boltzmann model cannot accurately solve the fluid-soil boundary using the bounce-back method. Although this can be improved using more sophisticated boundary treatment methods, it is computational costly and not suitable for simulating flow in porous media. An alternative is to keep the bounce-back method, and improve the accuracy by carefully choosing the relaxation time parameter. Theoretically, for fluid flow between two parallel plates, the locations of the two plates can be accurately solved when the relaxation time parameter is unity. For flow in the complicated void space, however, this many change. That is, the relaxation time parameter that gives accurate solution might depend on the pore geometry. To investigate this, we simulated gas flow in each image shown in the above figures using different relaxation time parameters for both BGK and MRT models.

Figure 5.8 shows the permeability of the uncompressed GDL in the three directions calculated by the BGK and MRT models using gases with different viscosity. Porosity of the GDL is 0.791. The permeability calculated by the MRT model remains almost constant regardless of the viscosity. In contrast, the permeability calculated by BGK increases with gas viscosity. The BGK permeability is lower than the MRT permeability when using low fluid viscosity but higher when using high fluid viscosity. At viscosity of

0.15, equivalent to $\tau = 0.95$, the BGK model gives the same permeability as the MRT model.

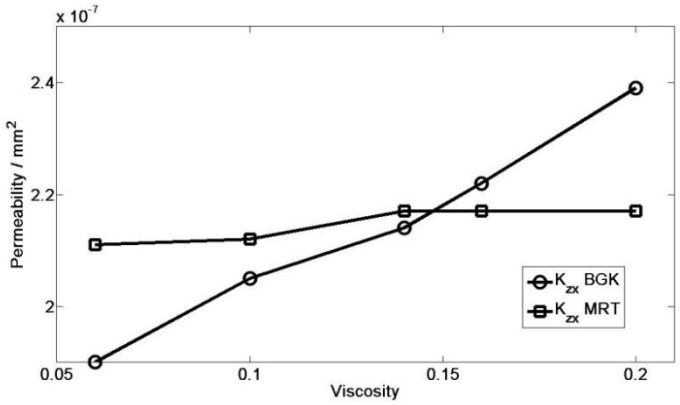

(a)

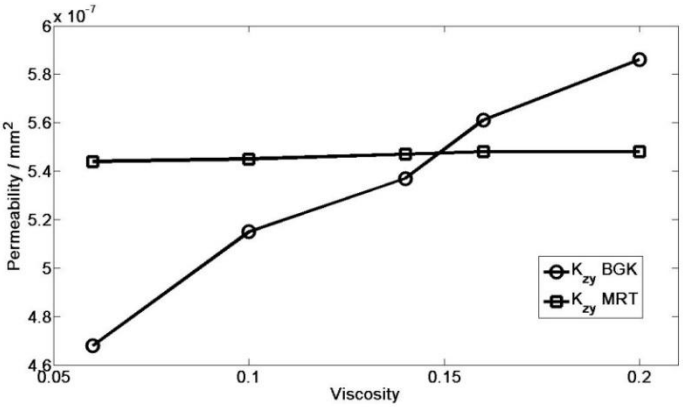

(b)

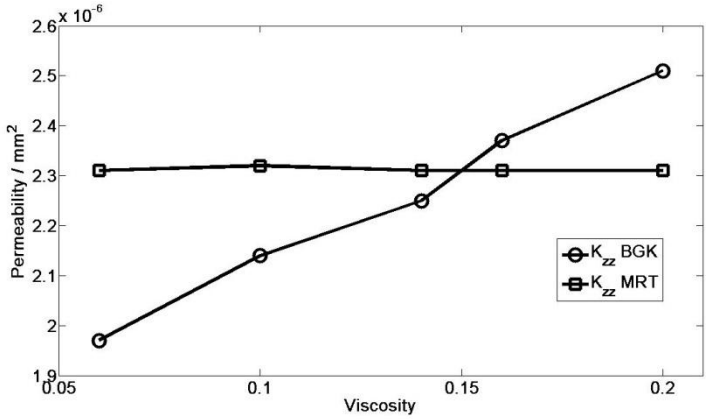

(c)

Figure 5.8 Comparison of the permeability simulated by BGK and MRT models using different relaxation parameters for the uncompressed GDL when flow is in the x direction (a), in the y direction (b), and in the z direction (c).

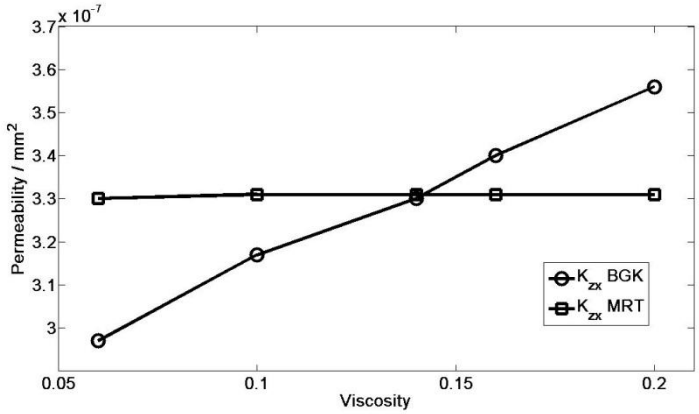

(a)

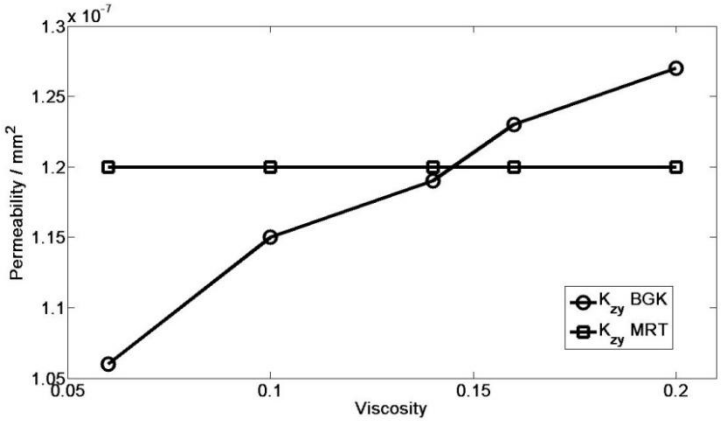

(b)

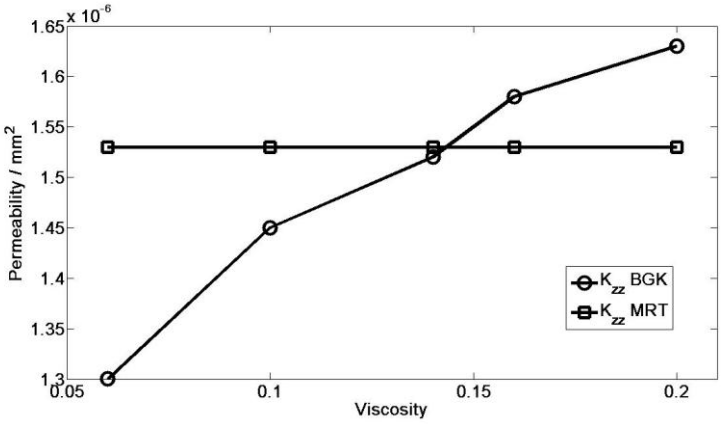

(c)

Figure 5.9 Comparison of the permeability simulated by BGK and MRT models using different relaxation parameters for the compressed GDL under 0.3Mpa when flow is in the x direction (a), in the y direction, and in the z direction (c).

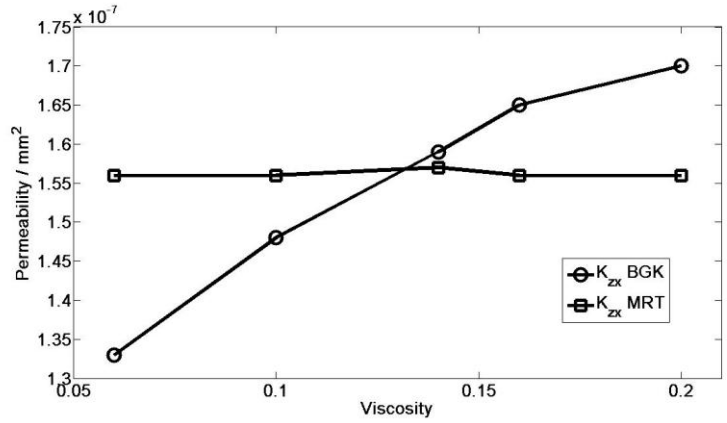

(a)

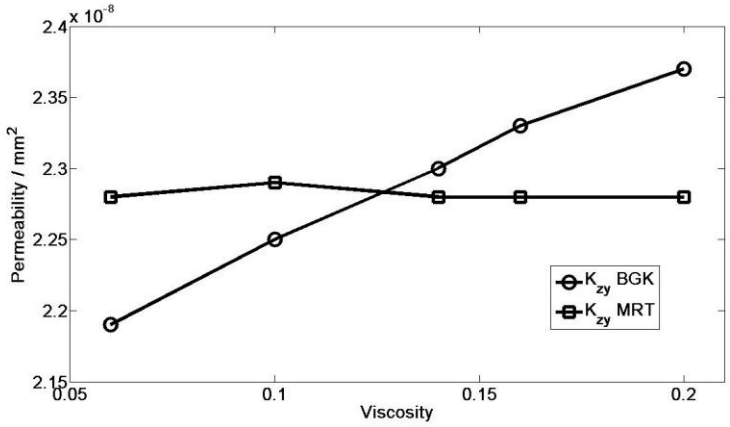

(b)

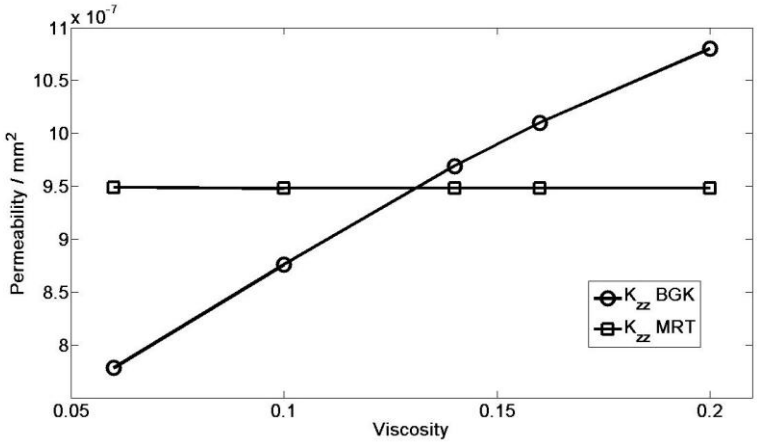

(c)

Figure 5.10 Comparison of the permeability simulated by BGK and MRT models using different relaxation parameters for the compressed GDL under 20Mpa when flow is in the x direction (a), in the y direction, and in the z direction (c).

Figure 5.9 and Figure 5.10 compare the BGK and MRT permeability of the compressed GDLs under 0.3 MPa and 20 MPa, respectively. The associated porosity is 0.638 and

0.523, respectively. Similar to the uncompressed GDL, the BGK permeability also increases with gas viscosity and the MRT permeability is independent of viscosity. For GDL with porosity of 0.638, the BGK permeability and MRT permeability are almost the same when the viscosity is 0.148, equivalent to a relaxation parameter of $\tau = 0.944$. For the GDL with porosity of 0.523, the BGK permeability and MRT permeability are the same when the viscosity is 0.13, equivalent to a relaxation parameter of $\tau = 0.89$.

Theoretical analysis based on flow between two parallel plates showed that the fluid-solid boundary can be accurately solved when the relaxation parameter is 1. As we anticipated, this value does not apply to flow in porous media as the fluid-solid boundary in porous materials is more complicated than the parallel plates. From the results shown in Figures 5.7-5.10, the optimum relaxation-relaxation parameter does not appear to be constant but varies with porosity, indicating that there is no optimal single relaxation time for the BGK model. However, they are very close to unity. Given that the computational time of BGK could be significantly reduced when using a unity relaxation time parameter, setting the relaxation time τ=1 might be the best choice for calculating permeability.

5.5 Velocity and pressure distribution in the GDL

The attraction of the LB simulations is that they also can reveal the detailed gas velocity and pressure distributions in the pore space at micron scale. Figures 5.11 and 5.12 show the pressure and streamlines in the uncompressed GDL when mean flow is in the x, y and z directions, respectively. Figures 5.13 and 5.14 show the pressure distribution and streamlines for gas flow in the compressed GDL. For both compressed and uncompressed GDLs, the streamlines in the through-plane direction appear to be more tortuous than that in the in-plane direction. In the compressed GDL under 20MPa, the streamlines appear to be more tortuous than that in the uncompressed GDL.

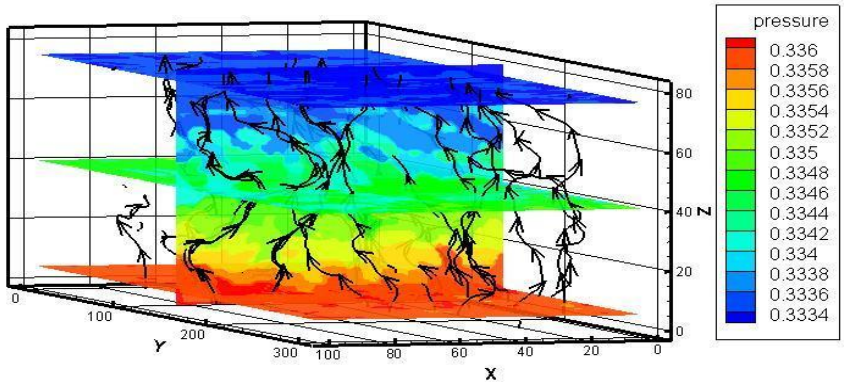

Figure 5.11 Change of the simulated permeability by MRT with porosity with the predictions of TS- and the K-C relations in the through-plane direction

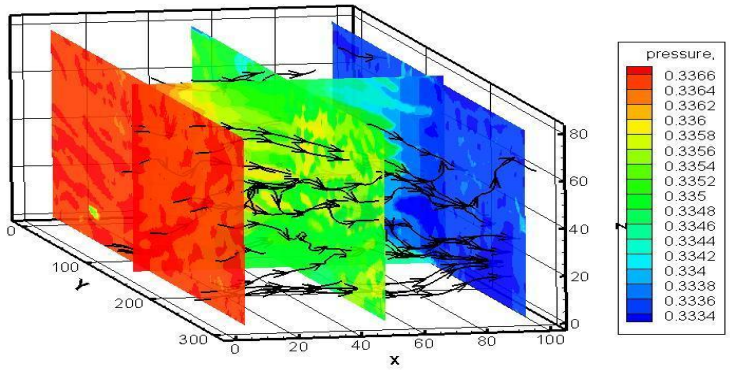

Figure 5.12 Change of the simulated permeability by MRT with porosity with the predictions of TS- and the K-C relations in the in-plane direction

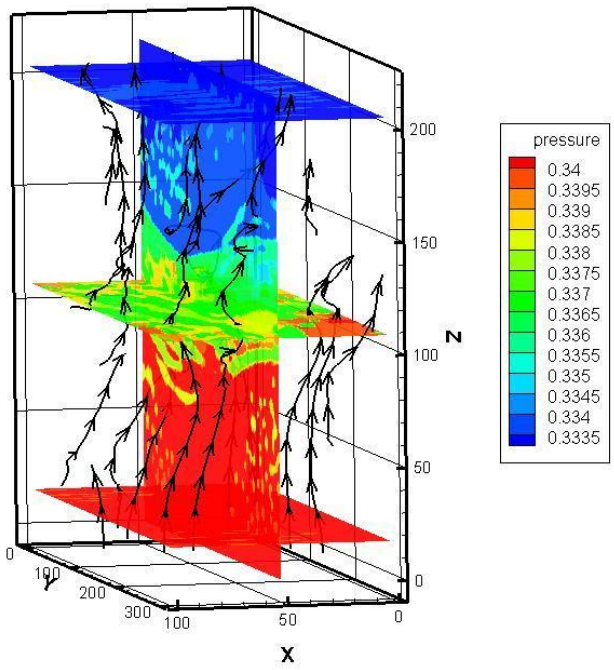

Figure 5.13 Streamlines and pressure distribution in the uncompressed GDL when the mean gas flow is in through-plane direction

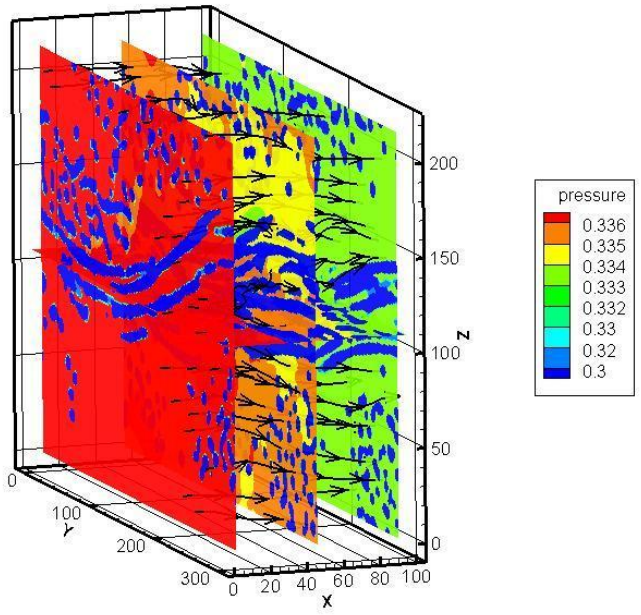

Figure 5.14 Streamlines and pressure distribution in the uncompressed GDL when the mean gas flow is in the in-plane direction .

5.6 Conclusions and discussions

This chapter demonstrates the potential of using the x-ray micro-tomography and lattice Boltzmann modelling to investigate the change of GDL permeability due to compression in fuel cell assembly.

The x-ray tomography successfully captured the structure change in the GDLs due to compression under different pressures, and the LB simulations can calculate the reduction in the ability of GDL to conduct gases due to the compression. The simulated results reveal that the decrease in permeability with porosity due to the compression can be well described by the empirical K-C relation and the T-S equation in both through-plane and in-plane directions for porosity in the range from 0.5 to 0.84.

We simulated all the GDLs using both BGK and MRT models. Although the BGK model can give accurate results, but only when a specific relaxation parameter is used; the value of this optimal relaxation parameter appears to increase with porosity, and cannot be determined priori. However, for all the samples we simulated, the optimal relaxation time parameter is from 0.89 to 0.98, very close 1. Therefore, using a unity relaxation time parameter in the BGK model will not result in significant errors. Overall, the MRT model is more robust, but is more computationally expensive. For calculating permeability, the BGK might be more practically useful as it does not give rise to significant errors by using a unity relaxation time parameter. Using a unity relaxation time parameter simplifies the collision calculation and can thereby further enhance computational efficiency as demonstrated in Chapter 4. In using a unity relaxation parameter, different viscosity can be achieved by changing the time step. However, when simulating transient flow where both pressure and velocity change with time, the MRT model is more superior over the BGK model. Also, since the error of BGK model lies in its inaccuracy in solving the fluid-solid boundary, and such error should depend on the size of the pores. Therefore, in terms of unrevealing detailed flow paths in the pore geometry, the BGK might not be able to give as accurate results as the MRT does.

Chapter 6 Simulate two-phase flow in GDLs

6.1 Introduction

The last two chapters focused on the LB models for single-phase flow. As reviewed in Chapter 1, when a fuel cell is in operation, the reducing reaction at the cathode produces water. Since the PEM fuel cells operate at low temperature ($<100C^{o}$), some water vapour will condense in the GDL and the catalyst layer at the cathode. Accumulation of liquid water could block pathways for oxygen movement and result in cell failure. Hence, to keep the cell work, the condensed liquid water needs to be drained to gas channel first and is then flushed out of the assembly. In this chapter, we will focus on the modelling of two-phase flow in the GDL.

To ensure the GDL to provide pathways for both liquid water and gases to move simultaneously in opposite directions, the GDL is often made hydrophobically heterogeneous so as to force water into a few channels, thereby leaving some space for gases to move through in opposite direction from the gas-supply channel to the catalyst layer. As a result, spatial distribution of the water in the GDL controls gas flow and hence fuel cell performance. Because of its opaque nature, water distribution in GDL is difficult to visualise. The existing work on water management in fuel cells is largely based on macroscopic models to predict saturation [127]. Whilst the saturation tells the percentage of pores that is filled by water, what controls gas flow in GDL is the connectedness of the pores that remain unoccupied by water. The development in imaging technology over the past decade has been overcoming this barrier, and there have been increased research in the use of neutron imaging to visualise liquid water distribution in operating cells [128]. In our previous work, we have successfully visualised 3D structure of the GDL at a resolution less than one micron using both computed x-ray tomography and FIB technology [54]. This, in combination with computational fluid dynamics, such as lattice Boltzmann (LB) method and smooth particle hydrodynamic methods, has made simulations of water flow and water distribution in GDLs feasible at scales as fine as a few hundred nano-meters [129].

Several LB models have been developed since the 1980s to simulate two-phase flow. The earliest lattice-type two-phase model is the approach proposed by Rothman and Keller [130] (referred to as RK model hereafter) based on the lattice gas algorithm (LGA).

Because of its nature, the RK model inherited some drawbacks of LGA such as numerical noises. Gunstensen et al. [131, 132] developed the LGA-based RK model into LB model based on the concept of McNamara and Zanetti [64] using a linearized collision operator proposed by Higuera and Jimenez [133]. The RK model used two colour particles to represent the two phases, and a perturbation to approximately recover the Laplace's law at the fluid interface; it overcomes some drawback of the original RK model, including lack of Galilean invariance and statistical noise. The drawback of this model is that it is not rigorously based upon thermodynamics and is thus difficult to incorporate microscopic physical processes [134]. In addition, the pressure in this model is velocity-dependent, and the linearized collision operator is not computationally efficient [135]. Recently, Ahrenholz et al has combined the RK model with the multiple-relaxation time LB model to simulate unsaturated water flow in glass beads column [136].

Another two-phase LB model is the method proposed by Shan and Chen [137, 138] (referred to SC model hereafter) and its modified versions [139, 140]. In the SC model, a nonlocal interaction force between particles of different fluids at neighbouring lattice is introduced, similar to the van der waals attraction between fluid particles. Phase separation occurs when the attraction interaction is strong enough. Hou et al. [141] compared the RK and SC models, finding that the SC model is superior to the RK model in reducing numerical noise and handling fluids with contrasting densities. Recent development in RK model has shown that such spurious noise can be reduced or even eliminated if using Latva-Koko's operator in the re-recolor step [142]. This could makes the RK model more competitive than the SC model as revealed in a comparative study by Huang et al. [143]. Both the RK model and the SC model are based on the same lattice Boltzmann equation, thus they are efficient for parallelization and easy to handle complicated boundaries. The SC model is a phenomenally-based model and does not conserve momentum locally. As such, some key parameters such as fluid-fluid surface tension cannot be derived as a priori, and has to be estimated based on numerical experiments. Also, the SC model cannot handle fluids with large density ratio.

The third two-phase LB model is the free-energy approach developed by Swift et al. [144, 145]. In this model, the equilibrium distribution functions in the classical LB model for ideal gases are modified so as to make it capable of simulating two-phase flow. The free-energy LB model conserves mass and momentum both locally and globally, and is

formulated to account for the equilibrium thermodynamics of non-ideal gases. The major drawback of this model is the unphysical non-Galilean invariance for the viscous terms in the macroscopic Navier-Stokes equation.

The above three models are widely used in the literature to simulate two-phase flow with each having the pros and cons as they are not directly derived from the kinetic theory. He et al proposed a two-phase model by linking the LB model to the Boltzmann equation in the kinetic theory [146]. However, numerical experiences revealed that this model is susceptible to numerical instability, particularly for fluids with large density and viscosity ratios. To improve numerical stability, Lee and Lin [121] developed a stable discretization method to solve the lattice Boltzmann equation proposed by He et al. [146]; results showed that the improved discretization method significantly enhances stability and can hence handle fluids with density as high ratio as 1:1000. Other two-phase models developed over the past decade for simulating fluids with high density ratios include the methods of Zheng et al. [147] and of Inamuro [148]. One drawback of these methods is that they need to calculate the derivatives up to second order, making them cumbersome to simulate two-phase flow in pore media because of the complicated fluid-solid boundary. Furthermore, most two-phase flow in porous media is dominated by capillary force. As a result, both the RK and SC models can offer good solutions and are widely used in practice.

There has been an increase in the use of LB models to simulate two-phase flow in fuel cells over the past few years. For example, Mukherjee and Wang [31] studied the influence of pore structure and GDL wettability on water transport and interfacial dynamics in stochastically constructed 3D catalyst layers and gas diffusion layer in fuel cells. Niu et al. [28] did similar work in attempts to examine water flow in stochastically reconstructed GDLs and the dependence of relative-permeability of both air and water on water saturation. For water flow in gas-supply channel, Hao and Cheng [33] simulated the dynamic behaviour of a water droplet under different flow conditions. We will investigate the impact of hydrophobicity on water intrusion in the GDLs using the SC model.

6.2 Pseudo Potential Model for simulation of Multiphase Flow

The lattice Boltzmann method for two-phase also consists of two steps: The first step is to calculate the collision between fluid particles, and the second step is to stream the fluid particles. The details of the method have already demonstrated in the Chapter 3.

The difference between the two-phase model and the single phase model is that the two-phase model needs to use a particle distribution function for each phase to track the movement and reaction of the two phases. Apart from this, there is phase reaction force that needs to be considered. Using the MRT lattice Boltzmann model, the evolution of the particle distribution function for each phase can be written as follows:

$$f_i^k\left(x+c\Delta t,t+\Delta t\right)-f_i^k\left(x,t\right)=-\Omega^k\left[f_i^k\left(x,t\right)-f_i^{k(eq)}\left(x,t\right)\right] \tag{6. 1}$$

where the subscript k (k=1, 2) represent the two phases. For the D3Q19 model, the equilibrium distribution function for each phase in Equation (6.1) is

$$\begin{aligned} f_a^{k(eq)} &= \omega_a\rho_k\left[1-\frac{3}{2}\frac{u_k^{eq}\cdot u_k^{eq}}{c_s^2}\right] \quad a=0, \\ f_a^{k(eq)} &= \omega_a\rho_k\left[1+3\frac{c_a\cdot u_k^{eq}}{c_s^2}+\frac{9}{2}\frac{(c_a\cdot u_k^{eq})^2}{c_s^4}-\frac{3}{2}\frac{u_k^{eq}\cdot u_k^{eq}}{c_s^2}\right] \quad a=1,\ldots,18, \end{aligned} \tag{6. 2}$$

where $\omega_0=1/3,\omega_{1,\ldots,6}=1/18,\omega_{7,\ldots,18}=1/36$ and $c_s^2=c^2/3\Delta t^2$.

Because of the phase reactions, the equilibrium distribution functions defined in Equation (6.2) need to be modified to include the reaction forces.

Shan and Chen proposed to incorporate the effect of external forces in the model by shifting the equilibrium velocity. In this regard, they proposed to use equation (6.3) to calculate the new equilibrium velocity which includes the forces.

The equilibrium velocity u_k^{eq} in equation (6.2) for fluid k is calculated from

$$\rho_k u_k^{eq}=\rho_k u'+\tau_k F_k \tag{6. 3}$$

where u' is the bulk fluid velocity of the two phases and is calculate by

$$u' = \frac{\sum_k \rho_k u_k / \tau_k}{\sum_k \rho_k / \tau_k} \tag{6. 4}$$

in which ρ_k is the density of fluid k and calculated by $\rho_k = \sum_{i=0}^{18} f_a^k$, and u_k is the velocity of fluid k and calculated by $\rho_k u_k = \sum_{i=0}^{18} f_a^k c_a$. F_k is the net force acting on fluid k , including fluid – fluid interaction F_1^k and fluid –solid interaction F_2^k . That is,

$$F_k = F_1^k + F_2^k \tag{6. 5}$$

where F_1^k and F_2^k are the fluid-fluid interaction force, fluid-solid interaction force, respectively for phase k. Any external force can be incorporated into the model through shifting the velocity. This will allow extension of the model to any kind of external forces.

6.3. Fluid-fluid interaction

In order to drive the phase separation , Martys and Chen [149] proposed to use a nearest neighbour interaction force in the lattice that depends on the density of each fluid as given by equation (6.6).

$$F_1^k(x) = -\rho_k(x) \sum_{x'} \sum_{\bar{k}} G_{k\bar{k}}(x, x') \rho_{\bar{k}}(x')(x' - x) \tag{6. 6}$$

where $\rho_k(x)$ is a function of density and is called the " effective mass". Different forms of $\rho_k(x)$ lead to different equations of state for each component, but here we adopt the simplest form. $G_{k\bar{k}}(x, x')$ is a coupling constant based upon a Green's function which controls the interaction force strength between the two fluids. $G_{k\bar{k}}(x, x')$ is defined as zero for the same fluid component and different from zero for different components. For the D3Q19 model $G_{k\bar{k}}(x, x')$ takes the form given in equation (6.7)

$$G_{k\bar{k}}(x, x') = \begin{cases} g_{k\bar{k}} & |x - x'| = 1, \\ g_{k\bar{k}}/2 & |x - x'| = \sqrt{2}, \\ 0 & \textit{otherwise}, \end{cases} \tag{6. 7}$$

where $g_{k\bar{k}}$ represents the strength of fluid-fluid reaction.

In general, in the SC model, an increase in relaxation time increases the diffusion. The effect becomes very significant for $\tau > 2.0$. Therefore, when relaxation time increases, mixing increases and the sharpness of the phase interface is lost. On the other hand, smaller fluid-fluid interaction strength due to small constant $g_{k\bar{k}}$ could increase diffusion. If the value of $g_{k\bar{k}}$ is smaller than a critical value, it could lead to complete mixing and no fluid separation. High $g_{k\bar{k}}$ values assure sharp interfaces with a small interface width, but there is an upper limit to $g_{k\bar{k}}$ because of the limitation of stability. The above model has limitation on density ratio of the two phases, and high density ratio could lead to numerical instability.

6.4 Fluid-solid interaction

Depending on the surface of the solid, the solid surface could either adsorb or repel one or two of fluids. This fluid-solid reaction is described by the following equation:

$$F_2^k(x) = -\rho_k(x) G_{ks}(x, x') n_s(x')(x' - x) \tag{6. 8}$$

where $G_{ks}(x, x')$ represents fluid-solid interaction strength and defines the wall wettability, $n_s(x')$ is a none-zero constant at the fluid-solid interface and zero otherwise. Therefore, by adjusting the parameter $G_{ks}(x, x')$ it is possible to control if the fluid wets the solid surface by attracting, or repels the fluid particles away from the solid surface. To ensure consistency with the fluid-fluid interaction, the fluid-wall interactive strength is described by

$$G_{ks}(x, x') = \begin{cases} g_{ks} & |x - x'| = 1 \\ g_{ks}/2 & |x - x'| = \sqrt{2} \\ 0 & otherwise \end{cases} \tag{6. 9}$$

The sign of g_{ks} describes hydrophobic or hydrophilic solid.

6.5. Parameter determination

The measurable parameters at macroscopic scale which control water intrusion in GDL are fluid-fluid surface tension and the fluid-fluid-solid contact angle, whilst the input parameters to the LB model are fluid-fluid reaction strength parameter $g_{k\bar{k}}$ and fluid-solid reaction strength parameter g_{ks}, which are not measurable. For given two fluids, their

surface tension is fully determined by g_{ks}, but there is no analytical expression for them. The same applies to the dependence of contact angle on $g_{k\bar{k}}$ and g_{ks}.To establish these relationships, a series of numerical experiments were carried out to numerically calculate the dependence of surface tension on $g_{k\bar{k}}$, and the dependence of contact angle on $g_{k\bar{k}}$ and g_{ks}.

6.5.1 Surface Tension

To establish the relationship between surface tension and $g_{k\bar{k}}$, the formation of water droplets with different diameters was simulated in a domain consisting of $50\times50\times50$ cubic cells; all the boundaries were treated as periodic boundaries. After the two fluids reached steady state, the pressure drop across the fluid-fluid interface was measured. The relationship between the pressure drop ΔP and the radius of the water droplet *R* is described by the following equation:

$$\Delta P = \frac{\sigma}{R} \tag{6. 10}$$

where σ is surface tension and ΔP is the pressure difference across the fluid-fluid interface.

One limitation of the SC model is that it is unable to deal with fluids with large density ratio. For water-air system investigated in this paper, the density and viscosity ratios are 1:800 and 1:15, respectively, which is beyond what the SC model can handle.

Water transport in the GDLs is controlled by several forces and to determine which force is in dominance, we estimated the Bond number (ratio of gravity to interfacial tension force), capillary number (ratio of viscose force to interfacial force) and Reynolds number (Ratio of inertial force to viscose force). The average pore size in the GDLs is approximately 10 microns. As a result, the ranges of the three numbers are: 1.6×10^{-4} for the Bond number, 2.47×10^{-8} – 1.92×10^{-7} for the capillary number, and 2.12×10^{-4} – 1.65×10^{-4} for the Reynolds number. This reveals that water flow in the GDL is dominated by capillary force. For numerical stability, in all the simulations were used $\rho_1 = 0$ and $\rho_2 = 1.0$ inside the initial bubbles and $\rho_1 = 1.0$ and $\rho_2 = 0.0$ outside the bubbles. The two dimensionless relaxation-time parameters were set to be $\tau_1 = 1.0, \tau_2 = 1.2$ and the dimensionless fluid-fluid interaction coefficient $g_{k\bar{k}}$ was set to be 0.001 in all the

simulations. Steady state was deemed to have achieved when the relative difference of the overall fluid velocity between two adjacent simulations was less than 10^{-6}.

Figure 6.1 shows the change of pressure drop across the fluid-fluid interface as the radius of the bubbles decreases. It is nicely fitted by Equation (6.10); the resulting surface tension is 0.366 in lattice unit.

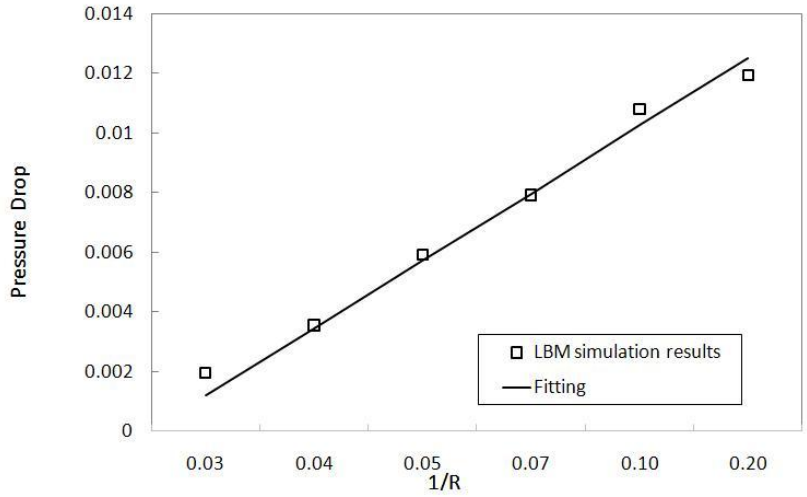

Figure 6. 1 Change of the pressure drop across the bubble surface with the bubble radius

6.5.2 Contact Angle

For a given $g_{k\bar{k}}$ and hence surface tension, the water-air-solid contact angle is entirely determined by g_{ks}. To establish the dependence of the contact angle on g_{ks}, a water droplet with radius of eight lattice units was placed on a solid wall in the z direction; we then simulated its settlement on the wall by using different fluid-solid reaction parameter g_{ks}. Periodic boundaries were applied to other sides of the computational domain. Simulations were carried out using various g_{ks} ranging from –0.002 to 0.002; other parameters remain the same as that in the surface-tension simulations. Once the two fluids reached steady state, the water-air-solid contact angle, θ, was calculated as follows:

$$\tan\theta = \frac{L}{2(R-H)} \tag{6. 11}$$

The finial radius R is evaluated from H and L by

$$R = \frac{H}{2} + \frac{L^2}{8H} \tag{6. 12}$$

where L is the length of the contact area between the droplet and the solid surface, H is the height of the droplet.

Figure 6.2 shows three contact angles obtained using different fluid-solid interaction parameter g_{ks} and the associated density contours of the droplets. The contact angle increases with g_{ks}. When g_{ks} is negative, the contact angle is less than 90^o and the solid is hydrophobic; when g_{ks} is positive, the contact angle is greater than 90^o and the solid is hydrophilic; when g_{ks} is zero, the solid is neutral and the associated contact angle is 90^o.

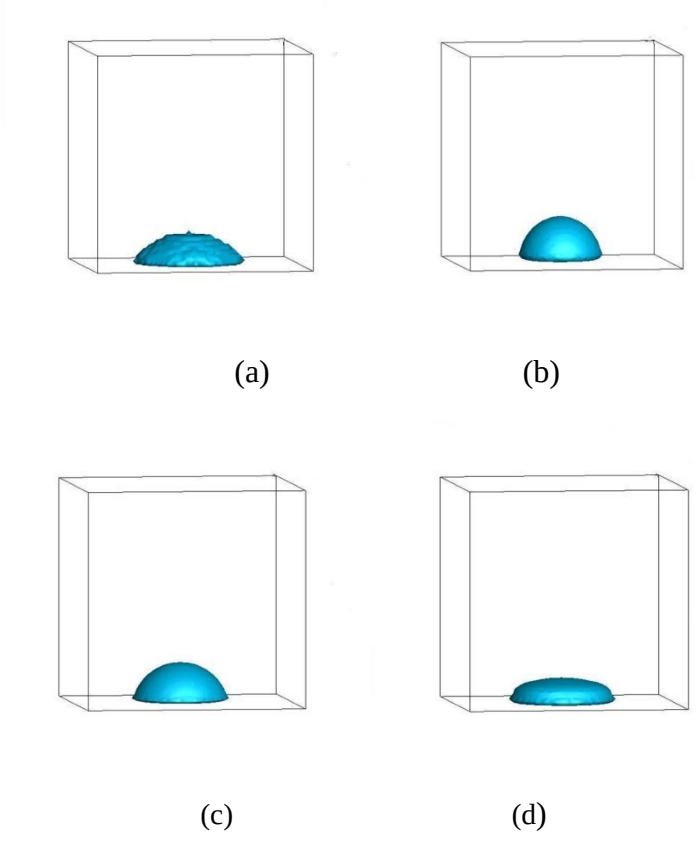

Figure 6. 2 Impact of g_{ks} on the shape of the droplets. (a) Initial state; (b) $\theta > 90^o$ for hydrophobic solid; (c) $\theta = 90^o$ for neutral solid; (d) $\theta < 90^o$ for hydrophilic solid.

Figure 6.3 shows the water distribution in narrow slits simulated using the model for both hydrophobic and hydrophilic slits.

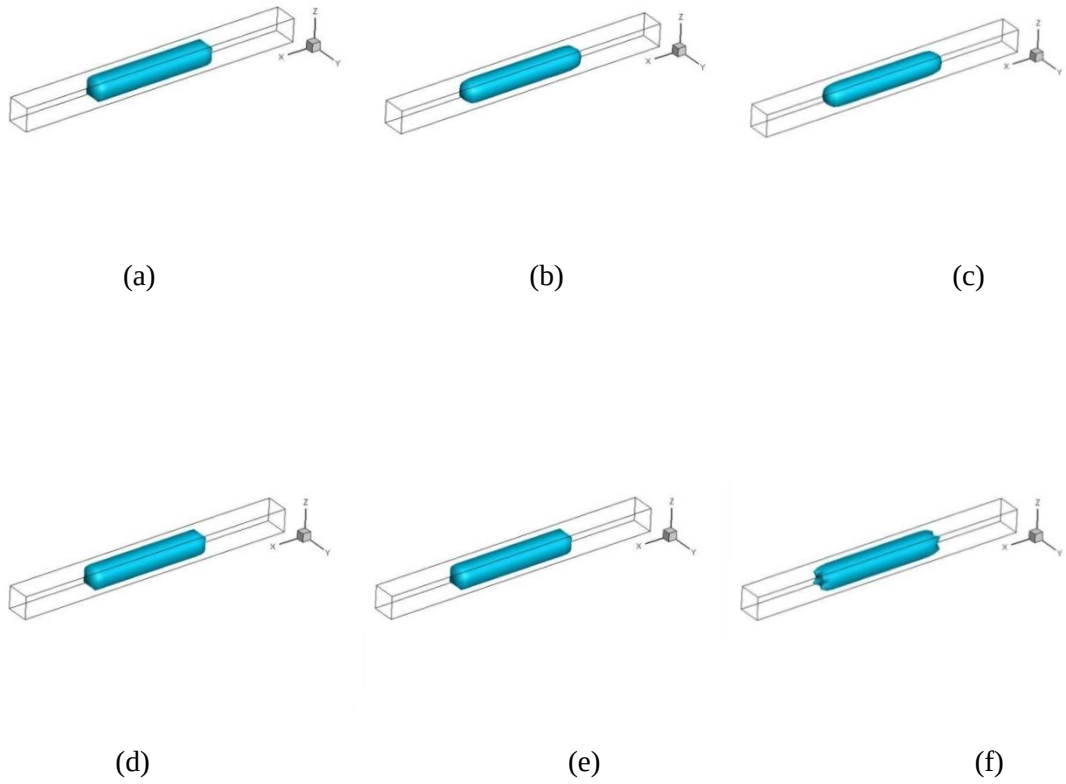

(a) (b) (c)

(d) (e) (f)

Figure 6. 3: Evolution of a water droplet in slits. (a)-(c) In hydrophobic slit: (a) initial state, (b) after 5000 time steps and (c) after 5000 time steps. (d)-(e) In hydrophilic slit: (d) initial state, (e) after 5000 steps and (f) after 5000 time steps.

6.6 Water flow in the GDLs

Water intrusion through a 3D x-ray image was simulated by applying a pressure drop in one direction; the pressure drop was simulated by imposing a prescribed pressure at the inlet boundary and a prescribed pressure at the outlet boundary; other four sides of the 3D image were treated as periodic boundary in which any particle exiting the image from one side re-enters the image from the opposite side with its mass and momentum remaining unchanged. The prescribed pressures were solved using the method proposed by Zou and He [92].

The GDLs used in the simulations were acquired by the x-ray micro-tomography at a resolution of 1.76 microns. Because of the limitation of computational power, we only simulated a small portion of the acquired image. The image is shown in Figure 6.4 and its size is 50×50×150 voxels. To mimic water flow in GDLs during cell operation, a pressure

drop was applied in the z direction in an initially dry GDL. Driven by the pressure drop, water moved into the GDLs, but the intrusion speed and water distribution in the GDLs change with the pressure drop and the hydrophobicity. The pressure drop was maintained by applying a constant water pressure and zero air pressure at the inlet, and a constant air pressure and zero water pressure at the outlet. Figure 6.4 (b) shows the initial setup of the simulations.

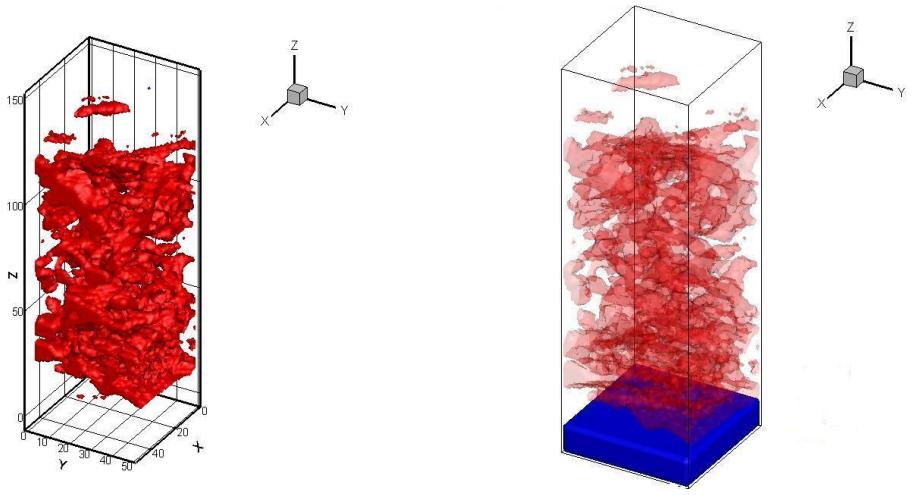

(a) (b)

Figure 6. 4 (a) Reconstructed GDL image. (b) Initial condition for water intrusion into a dry GDL.

To investigate the impact of hydrophobicity, we simulated water intrusion into both hydrophobic and hydrophilic GDLs. Figures 6.5-6.8 show the water distribution and the invasion pattern driven by different pressure drops. It is evident that the water intrudes faster as pressure drop increases.

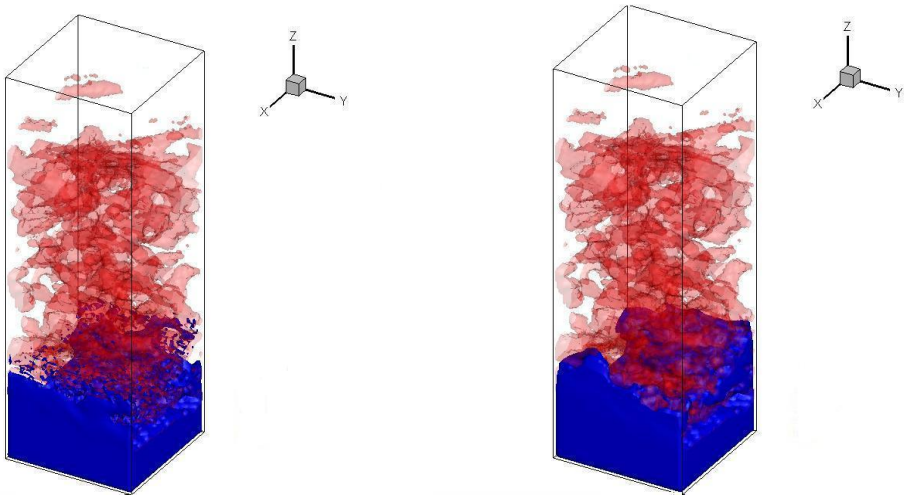

(a) (b)

Figure 6. 5 Water intrusion into hydrophilic GDL (a), and hydrophobic GDL (b) under a pressure drop of 0.594 *KPa* .

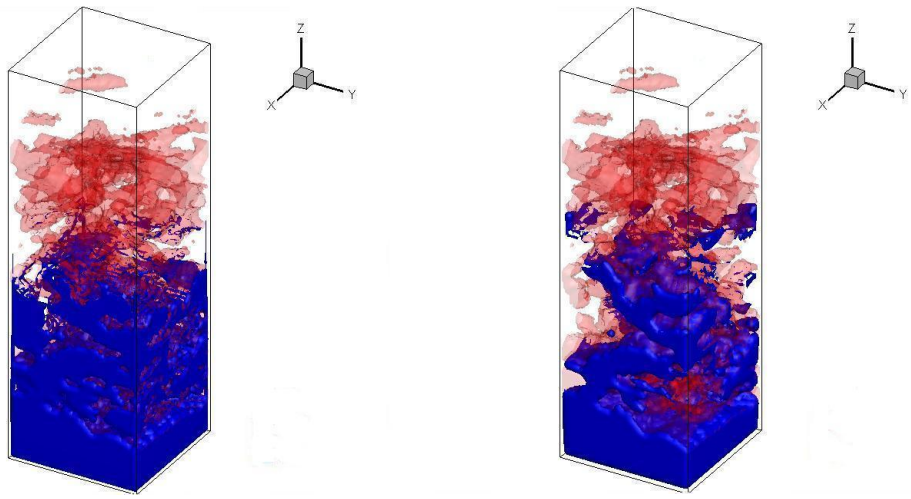

(a) (b)

Figure 6. 6 Water intrusion into hydrophilic GDL (a), and hydrophobic GDL (b) under a pressure drop of 2.97 *KPa* .

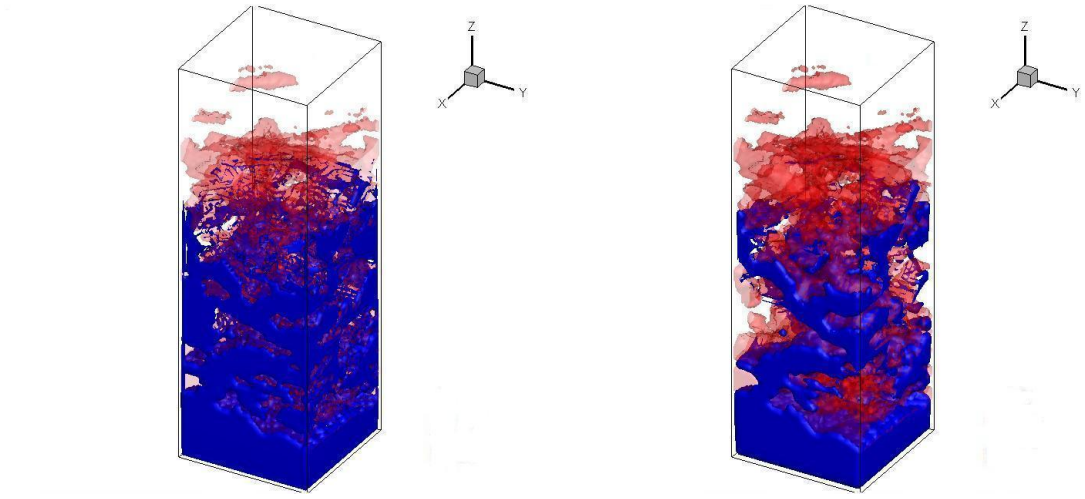

(a) (b)

Figure 6. 7 Water intrusion into hydrophilic GDL (a), and hydrophobic GDL (b) under a pressure drop of 5.94 KPa .

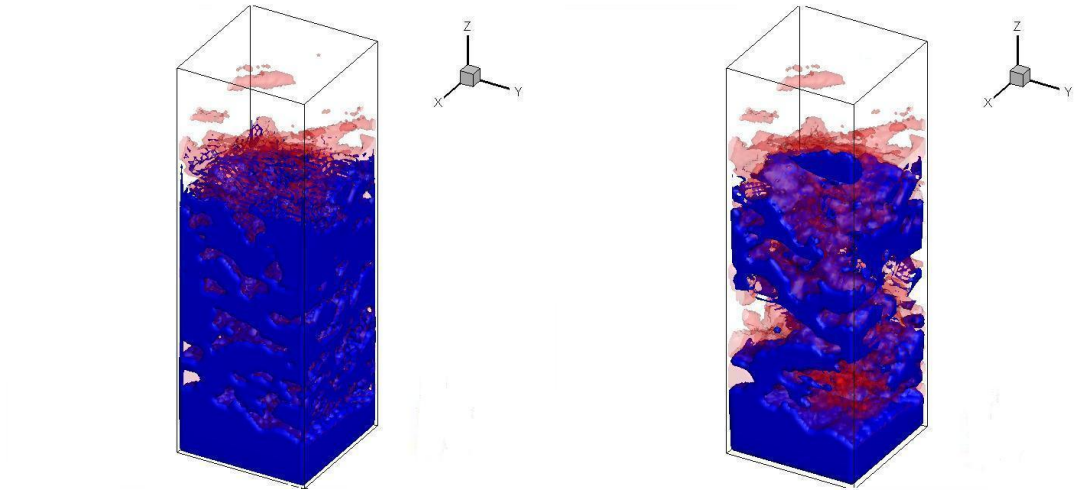

(a) (b)

Figure 6. 8 Water intrusion into hydrophilic GDL (a), and hydrophobic GDL (b) under a pressure drop of 11.88 KPa .

Figure 6.5 shows water distribution in both hydrophobic and hydrophilic GDLs driven by a pressure drop of 0.594 KPa . It reveals that at low pressure drop, the invading front of the water overcomes the barrier pressure only at some preferential locations due to the resistance of the capillary force. It is evidence that as the applied pressure drop increases, the water intrudes deep in both hydrophobic and hydrophilic GDLs as shown in Figures 6.6-6.8. However, the water distribution in hydrophobic GDL differs noticeably from that

in hydrophilic GDLs. As the pressure drop increases, water intrusion in the hydrophilic GDL likes piston-flow, occupying almost all the available pore space as shown in Figure 6.8(a), whilst in the hydrophobic GDL, the water was channelled, leaving a significant space for the air to flow. This has important implication in fuel cell design.

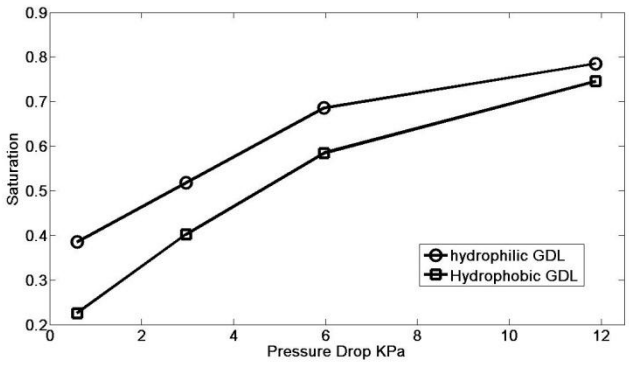

Figure 6. 9 Water intrusion into hydrophilic GDL (a), and hydrophobic GDL (b) under a pressure drop of 11.88 KPa .

Figure 6.9 further demonstrates the change of saturation under different pressure drops when water intrusion reached steady state in both hydrophobic and hydrophilic GDLs. The results indicated that the saturation increases with the pressure drop for both hydrophilic and hydrophobic GDLs. However, at low pressure drop, the saturation in the hydrophobic GDL is much lower than the saturation in hydrophilic GDL, and as the pressure drop increases, the difference between hydrophilic and hydrophobic GDLs decreases.

6.7 Conclusions and discussion

We investigated numerically the impact of hydrophobicity on water intrusion in GDLs used in hydrogen fuel cell industry. The numerical simulations were based on the multiple-relaxation time lattice Boltzmann model. In the simulations, the dependence of water-air surface tension and water-air-solid contact angle on the LB model parameters was established by simulating the formation of water droplets in air and on the top of a solid wall respectively. Simulated results revealed that, under high pressure drop, water intrusion in hydrophobic GDLs is likely to be channelled, bypassing some pores, whilst in the hydrophilic GDLs, water intrusion likes a piston-flow in which water occupies all the pore space. Under low and medium pressure drops, because of the capillary barrier, water

in both hydrophilic and hydrophobic GDLs is unsaturated, but water distribution in them is different. In hydrophobic GDL, the water exists in large pores, whilst in hydrophilic GDL the water intrudes into the small pore first.

We used the SC two-phase model to simulate water intrusion. The SC model is a phenomenal model, solving the fluid-fluid interface by diffused interface method in which the interface thickness spans several lattices. Therefore, spatial resolution needs to be sufficiently high in order to accurately represent the fluid-fluid interface. For example, a recent study of Yu and Fan [150] reveals that the surface tension estimated by the SC model using different spatial resolutions could differ significantly and depends on the value of the relaxation parameters. In fuel cells design, what is interesting is water distribution when flow reaches steady state. Furthermore, since water flow in GDL is dominated by capillary, we use relaxations parameters for both fluids close to unity in the simulations; the water-air surface tension is recovered by adjusting the time step. This naturally overcomes the dependence of surface tension on the relaxation parameters. For the impact of the spatial resolution, the porosity of a typical GDL is approximately 0.8 and the average pore size is 10 microns. The X-ray images were acquired at a very high resolution, 1.7 microns, which should be sufficient for LB simulations. Because of the heterogeneous nature of GDLs, however, it is likely that some fine pores in the GDLs might have been poorly represented in the X-ray image; the impact of such pores on the accuracy of the simulated results is an issue that needs a further investigation. In all 3D simulations, there is always a trade-off between solution accuracy and the size of the sample which should be big enough to representative. Yu and Fan [150] proposed an adaptive mesh method which could be useful to solve this dilemma, using fine mesh in fine pores and coarse mesh in big pores. Nonetheless, the results presented in this paper provide some insights into the impact of hydrophobicity on water intrusion in GDLs. The results show that manufacturing GDLs hydrophobic is able to force water into channels, but hydrophobicity makes water difficult to move from GDLs to gas supply channel. Therefore, in design, fully hydrophobic GDLs might not be able to improve water management. An alternative is to make GDL heterogeneously hydrophobic in that some areas are hydrophilic and some areas are hydrophobic. As such, liquid water can be channelled under both high pressure and low pressure. How to experimentally quantify the heterogeneous hydrophobicity of GDL and its effect on water flow needs further work.

Chapter 7: Gas flow in catalyst layer

7.1 Introduction

Previous chapters investigated gas flow and liquid water intrusion in gas diffusion layers (GDL). In a typical GDL, the average pore size is approximately 10 micron, and the impact of fluid-wall collision is negligible, and the dynamic properties of the fluid can be described by single viscosity. In catalyst layer, however, the averaged pore size is less than 100 nano-metres, and fluid-wall collision could have a considerable impact on fluid properties. What characterises the relative dominance of fluid-fluid collision and fluid-wall collision is the Knudsen number, which is defined as the ratio between an averaged distance that a gas molecule travels between two consecutive collisions with other gas molecules and the characteristic size of the domain in which gas flows. As the Knudsen number increases, the impact of fluid-wall collision becomes increasingly important, and the dynamical property of the fluid is no longer able to be described by a single viscosity. Such flow is often called micro-flow, and in fuel cells it occurs in the catalyst layers.

There has been an increased interest in micro-flow over the past decade[151]. Micro-flow cannot be described by the continuum approach such as the Navier-Stoke equation and some extra processes need be considered [152, 153]. The most important one is rarefaction, which is attributed to the original characteristics of fluid itself. Since micro-flow is in the dimension of 0.1 to 10 nm , the fluid-wall collision frequency is comparable with fluid-fluid collision frequency. As such, the fluid velocity at the wall surface can no longer be assumed to be non-slip, and as a result, it cannot be given a priori value. Instead, the slip velocity is part of the problem to be solved in micro-flow.

Traditional modelling of micro fluid flow is based on molecular dynamics (MD). In MD modelling, the fluid is treated as a collection of particles, whose number should be sufficient to yield average-meaningful results to characterise the flow at a scale at which flow phenomena are measurable. The MD models are computational costly. Over the last few years, efforts have been made to develop the lattice Boltzmann model as an alternative to simulate fluid flow at nano scales. For example, Nie et al developed a LB model to simulate compressible flow in 2D micro-channels, finding that the LB model can capture fluid behaviours such as velocity slip, nonlinear pressure distribution along the

channel and the dependence of mass flow rate on Knudsen number [154, 155]. In their model, the impact of Knudsen number was accounted for in the viscosity, which in turn was solved by allowing the relaxation-time to change with the Knudsen number.

Review on micro-fluid modelling has been given by several researchers [152, 156-159], and the lattice Boltzmann models for simulating micro-flows were also improved [154, 160-162]. When gas flows in micro-pores, because of the gas slippage on the solid boundaries, the frictional dragging force is reduced. Such reduced dragging force depends on Knudsen number; the higher the Knudsen number, the less the dragging force is. In terms of the impact of the Knudsen number on gas flow in porous media, this means that the medium permeability is no longer the property of the medium, but also depends on the Knudsen number. This has been experimentally proven for H_2, N_2 and CO_2 flow through a porous medium[163] .

Shen et al [164, 165] extended the work of Nie et al, and compared their simulated velocity and pressure distributions in micro-channel with that obtained from the MD model. In their LB model simulations, Shen et al used bounce-back method to treat the solid walls and the extrapolation scheme to treat the inlet and outlet boundaries of the channel. The predicted flow rate was found to be in good agreement with the results obtained from other methods with various Knudsen numbers (0.0194, 0.194 and 0.388). The results of Shen et al showed that the LB model of Nie et al. [154, 155] is feasible to simulate gas flow only when the Knudsen number is small or moderate, and that it will give rise to considerable errors as the Knudsen number becomes large. Lee et al. [166, 167] proposed a second order definition of Knudsen number and a wall equilibrium boundary condition for simulating gas flow in micro-channels using the LB model; their tested examples show that the slip velocity simulated by the LB model was in close agreement with Arkilic's prediction [168, 169], indicating that their definition of the Knudsen number and the wall equilibrium boundary conditions are more physically meaningful than those used in previous studies [154, 155, 160, 170].

The catalyst layer is an important component in FEM fuel cells as it is the place where all electrochemical reactions take place. However, since the catalyst layer is only a few hundreds of nano-metre thick, it is difficult to measure and quantify its ability to conduct gases. Therefore, in most macroscopic modelling, the catalyst layer was treated as an infinitely thin layer which is solved as prescribed flux boundary to the gas diffusion layer.

The flux is described by the Butler-Volmer equation which relates the flux rate to over-potential and local concentration of the reactants [171, 172]. This is an over-simplification as the local concentration in the catalyst layer depends not only on reactant concentration at the interface between the catalyst layer and the GDL, but also on how the reactants move into the catalyst layer. Over the past few years, there has an increased interest to explicitly include the catalyst layer in macroscopic modelling. This, however, needs to know the effective permeability and effective diffusion coefficients of the catalyst layer to conduct gases, driven by both pressure gradient and molecular diffusion. Several stochastically models have been developed to investigate gas flow in catalyst layer, and Lang et al compared their impact on the effective transport properties [173, 174]. However, in these models, the gas flow was assumed to be diffusion-dominated and the flow in cathode involves oxygen, water vapour and oxygen. The movement of each species is described by the Stefan-Maxwell equations with a modified diffusion coefficient to account for the Knudsen diffusion due to gas-wall collision. In a recent work, Wu et al used pore-network models to simulate oxygen flow in catalyst layer at the cathode by assuming that oxygen flow was driven by molecular and Knudsen diffusion only [175, 176].

The pore geometry in catalyst layer is heterogeneous with the size of its pores ranging from 20 nano-metres to 120 nano-metres. As a result, the Knudsen number is also heterogeneous with smallest pore having the highest Knudsen number. How such a heterogeneous Knudsen number affect the effective transport and reactive ability of the catalyst has attracted attention. For example, Siddique and Liu investigated the impact of heterogeneous Knudsen number on the effective oxygen diffusion based on a numerically re-constructed catalyst layer, finding that the commonly used Bruggemann relation considerably underestimated the increase of effective diffusion coefficient with porosity [177, 178].

A typical catalyst layer consists of carbon to conduct electron and offer support to platinum nano-particles; inoometer binding to provide paths for proton conduction, and pores to provide path ways for gases to flow. To investigate how the carbon affects gas flow and proton conduction, Lange et al numerically generated a catalyst layer assuming that the carbon are uniform spheres [179, 180]. Their result showed that effective oxygen diffusion coefficient depends not only on porosity, but also on how the carbon spheres are packed.

All available work on catalyst layers assumed that the bulk velocity of the mixture of the gases is zero, and that gas flow was dominated by molecular and Knudsen diffusion. The underlined assumption is that there is no friction between gas molecules and solid surface. This is a simplification. The purpose of this chapter is to investigate the impact of nano-pores on the ability of catalyst layer to conduct gases when gas flow is also driven by pressure gradient, in which the dragging force of the solid wall to the gas flow varies with the Knudsen number.

7.2. A simplified approach to the catalyst layer

The pores in catalyst later (CL) are multi-modal with the pore-size distribution centred around 50-100nm. The size of the carbon grains in CL is in the order of 10nm, which can agglomerate to 100 nm clusters. The catalysts deposit on the surface of carbon grains, and their size is in the order of 1nm. Figure 7.1 shows a SEM image of a typical catalyst layer [181-183].

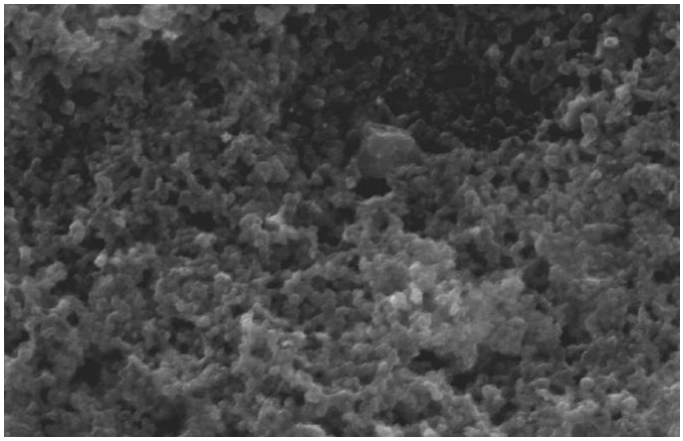

Figure 7. 1 A SEM image of a cathode catalyst layer

Figure 7.2 shows a 3D image acquired by a focused ion beam tomography at resolution of 15 nm, and Figure 7.3 shows the pore-size distribution for the image shown in Figure 7.2. It is evident that 39% of the pores has diameter in the range of 20-60 nm, and 45% in 60-150nm. The reconstructed CL also reveals that the characteristic mean pore radius and the characteristic mean pore-pore lengths are 55nm to 78 nm, respectively.

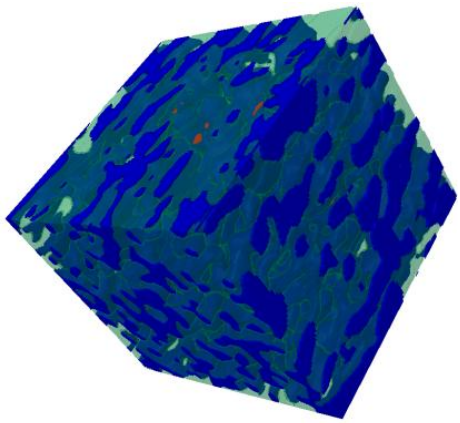

Figure 7.2. FIB/SEM image of the catalyst layer at resolution of 15nm

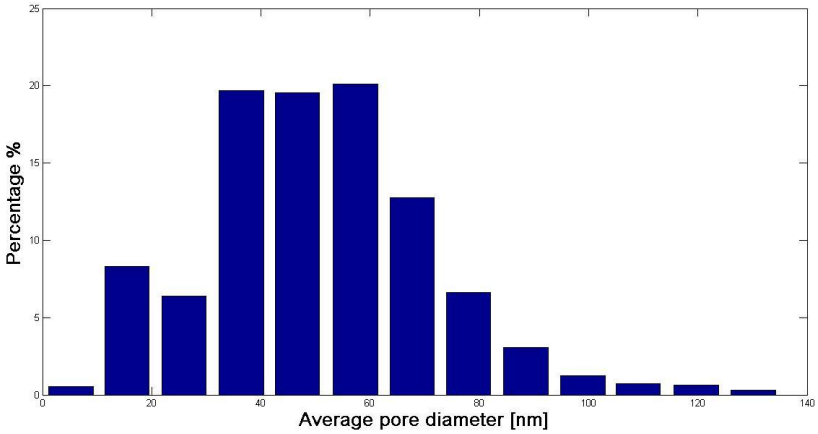

Figure 7. 3 The distribution of averaged pore sizes in the CL

Directly simulating gas flow through the nano-scale pores shown in Figure 7.2 is difficult since the Knudsen number varies not only from pores to pores, but also with flow directions. As an illustrative investigation on how the Knudsen number affects the medium permeability, we idealized the complicated pore geometry into a bundle of tubes. Figure 7.4 shows the pore network extracted from the 3D image shown in Figure 7.2. Based on the network, we further simplify the void space into a bundle of tubes in that gas flow in the tubes is independent of each other. The diameter of each tube and the number of the tubes can be estimated from the pore size distribution.

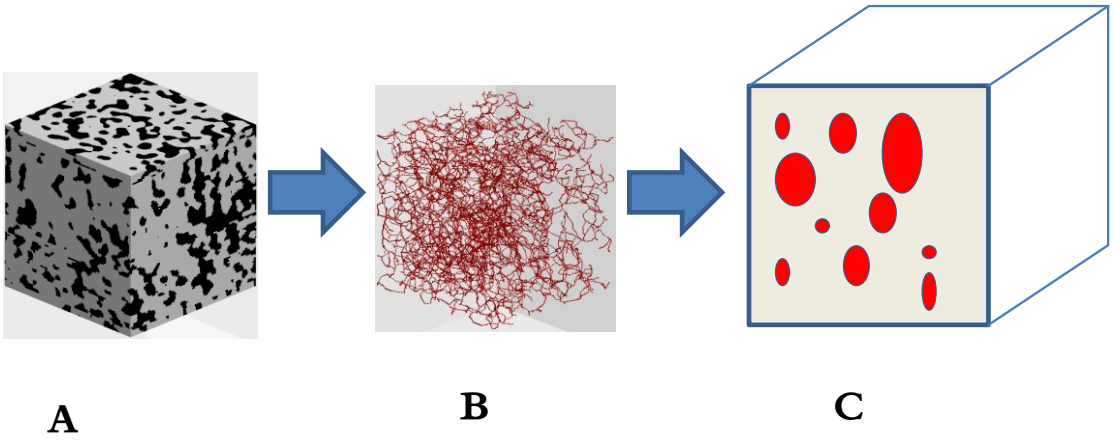

Figure 7.4 From 3D FIB/SEM image (A) to network model (B) and tube model (C)

For a given gas, each tube has a specified Knudsen number. Simulating gas flow in all the tubes with the specified Knudsen numbers could reveal how the heterogeneous Knudsen number affects the ability of the GL to conduct gases. Figure 7.5 shows a tube.

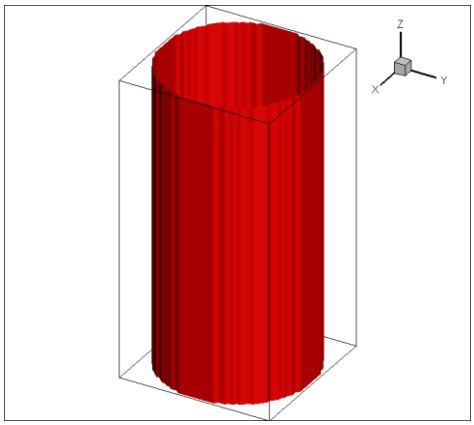

Figure 7. 5 The structure of a single 3D tube in Figure 7.4

Once the flow rates in all the tube are calculated, the averaged flow rate, similar to the Darcy's flow rate explained in previous chapter, can be used to calculate the effective permeability of the catalyst layer as follows,

$$k = \frac{\mu Q}{\nabla p} \tag{7. 1}$$

where μ is the kinematic viscosity of the gas, ∇p is the pressure gradient and Q is the averaged flow rate which is the volume of gas flowing across an area of A during a period

of unit time. The value of A can be calculated from porosity and pore-size distribution. For example, for a catalyst layer with porosity of 40% and known pore-size distribution, the area A is calculated from

$$\frac{\sum_{i=1}^{N} \pi R_i^2 \times w_i}{A} = 40\% \tag{7. 2}$$

where w_i is the percentage of the pores that have diameter of R_i.

7.3. LB model for gas flow in a single tube

For flow in micro-channel, the wall-gas collision frequency is comparable to gas-gas collision frequency. As such, there is a slip on the solid wall, and the dynamic property of the gas depends not only on its viscosity, but also on the Knudsen number. In LB models, this is solved by accounting for the impact of Knudsen number into the relaxation time parameter and modifying the boundary treatment.

7.3.1 The relationship between relaxation time and Knudsen number

In dynamic theorem, the mean free path of a gas molecule is proportional to its dynamic viscosity and inversely proportional to its pressure; that is;

$$\lambda = \frac{\eta}{p\sqrt{\pi RT/2}} \tag{7. 3}$$

where λ the is the mean free path, $\eta = \rho\mu$ is the dynamic viscosity, p is gas pressure, R is the gas constant and T is temperature.

For flow in a 3D micro-tube driven by pressure gradient, because of the pressure change, the Knudsen number also change, increasing as the pressure decreases. If the pressure at the outlet of the tube is known, the value of the Knudsen number at the outlet can be determined as follows:

$$K_{n0} = \frac{\lambda}{H} \frac{\eta\sqrt{\pi}}{H\sqrt{2\rho^2 RT}} \tag{7. 4}$$

where ρ is density, H is the diameter of the tube. Assuming the Knudsen number at the outlet is K_{n0}, then the Knudsen number at location z from the inlet, $K_n(z)$, can be expressed as follows:

$$K_n(z) = K_{n0} \cdot P_{out} / P(z) \tag{7. 5}$$

where P_{out} is the prescribed pressure at the outlet.

Recent studies showed that most LB models for micro-flows are inadequate when K_n >0.1 [184, 185] due to their inaccuracy to capture the Knudsen layer near the solid surface. To improve LB model for simulating flow with high Knudsen number, one can use effective relaxation time as detailed below.

When fluid flows over a solid surface, a Knudsen layer exists near the solid surface with its thickness comparable to the mean free path. If the K_n is not negligible, one can use the effective Knudsen number defined as follows [184, 186-188]:

$$K_{ne} = K_n \psi(K_n) \tag{7. 6}$$

where K_{ne} is the effective Knudsen number, and K_n is the local Knudsen number calculated from the Eq. (7.5). For gas flow in a tube, the value of ψ can be described as follows:

$$\psi(K_n) = 1 + 0.5[(a-1)e^{-a} + (\beta-1)e^{-\beta} - a^2 E_i(a) - \beta^2 E_i(\beta)] \tag{7. 7}$$

where $a = x/\lambda$, $\beta = (H-x)/\lambda$, and $E_i(x) = \int_1^\infty t^{-1} e^{-xt} dt \quad x = 1, 2, ...H$ is the exponential integral function, which considers the variation of the effective Knudsen number in both stream-wise and span-wise directions.

For gaseous micro-flow, the effective relaxation parameter τ in the lattice Boltzmann equation approximation is modified to consider the gas compressibility, and the effective Knudsen number is calculated from

$$\tau = 0.5 + \sqrt{6} N_y \cdot K_{ne} / \sqrt{\pi} \tag{7. 8}$$

Where L is the length of the tube, δy is the side length of the voxels, $N_y = L/\delta y$ is the lattice number, and K_{ne} is the local effective Knudsen number.

7.3.2 Fluid-solid boundary

The gas velocity at the solid wall is not zero but depends on the Knudsen number. It thus needs a special treatment. For the wall boundary, the bounce-back method is usually used with a specular reflection to reflect that the solid wall is no longer a non-slip boundary [160, 170].

For the D3Q19 model used in this work, the combination of the bounce-back and specular -reflection boundary treatment is.

$$f_a(x,t) = r f_{\bar{a}}(x,t) + (1-r) f_{a'}(x,t) \tag{7. 9}$$

where $0 \le r \le 1$ is a coefficient that weights the portion of the contribution of the no-slip bounce-back and specula reflection, respectively. As an illustration example, we take the upper wall as an example. The particle distribution functions are computed as follows after the bounce-back treatment:

$$\begin{aligned}
f_8(x,t) &= r f_{10}(x,t) + (1-r) f_7(x,t) \\
f_7(x,t) &= r f_9(x,t) + (1-r) f_8(x,t) \\
f_1(x,t) &= f_2(x,t) \\
f_{10}(x,t) &= r f_8(x,t) + (1-r) f_9(x,t) \\
f_7(x,t) &= r f_9(x,t) + (1-r) f_8(x,t) \\
f_4(x,t) &= f_3(x,t)
\end{aligned} \tag{7. 10}$$

The value of *r* in the above equation can be chosen as follows [189, 190]. For the MRT model

$$r = \frac{2c_1}{\sqrt{\frac{\pi}{6}} + c_1} \tag{7. 11}$$

where $c_1 = 1.11$ will be used in the simulation.

For BGK model

$$r = \{1 + \sqrt{\frac{6}{\pi}}[\frac{\Delta^2}{4Kn} + A_1 + (2A_2 - \frac{8}{\pi})Kn]\}^{-1} \quad (7.12)$$

where $\Delta = y/H$ with y varing from 1 to H, and A_1 and A_2 are the accumulation coefficients between the wall and gas, and are usually chosen as $A_1 = 2\zeta/\sqrt{\pi} = 1.1466$ and $A_2 = (1+2\zeta^2)/2 = 0.9757$.

We assume that the gas flow is driven by a pressure drop between the inlet and outlet. The pressure at the inlet and outlet are P_{in} and P_{out} respectively; $P_r = P_{in}/P_{out}$ is pressure ratio. When the Knudsen number can be neglected, the pressure is linearly distributed along the tube:

$$P_l(z) = P_{in} + \frac{z}{L}(P_{out} - P_{in}) \quad (7.13)$$

With the impact of Knudsen number, the pressure distribution is P(z), and the difference between P(z) and $P_l(z)$ is defined as pressure deviation, which, after normalization, is,

$$P^* = [P(z) - P_l(z)]/P_{out} \quad (7.14)$$

The analytical solution for the normalised pressure deviation along the channel is given as follows [191].

$$P^*(\bar{z}) = -8K_{n0} + \sqrt{(8K_{n0})^2 + (1+16K_{n0})\bar{z} + (P_r^2 + 16K_{n0}P_r)(1-\bar{z})} \quad (7.15)$$

where $\bar{z} = z/L$.

7.4 Model validation

Gas flow in the tube shown in Figure 7.6 was simulated to validate the model. The simulations are for gas flow both in both the cathode and anode. As such, we consider hydrogen, oxygen and water vapour. The associated Knudsen number for H_2, O_2, and H_2O (vapour) at the outlet is 0.1, 0.054472 and 0.062413, respectively, and are calculated by Equation (7.4).

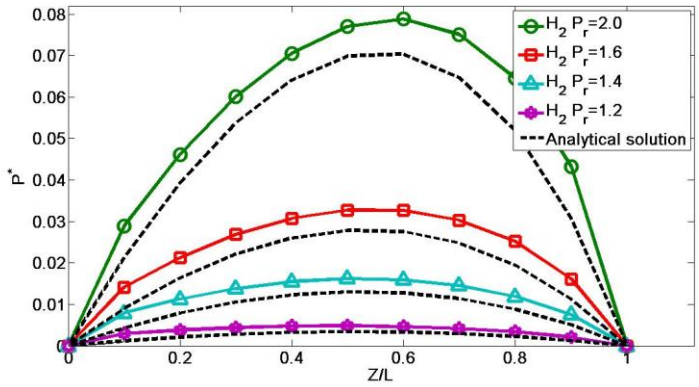

(a)

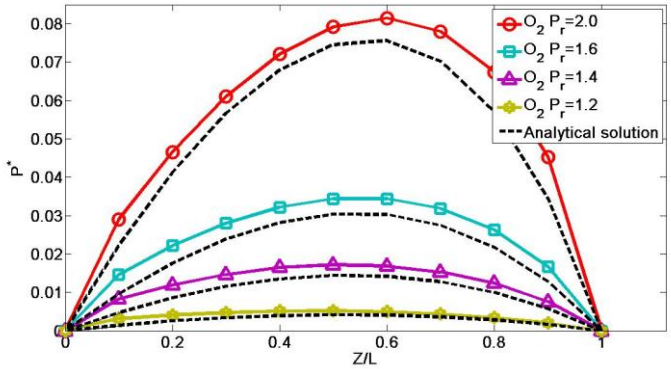

(b)

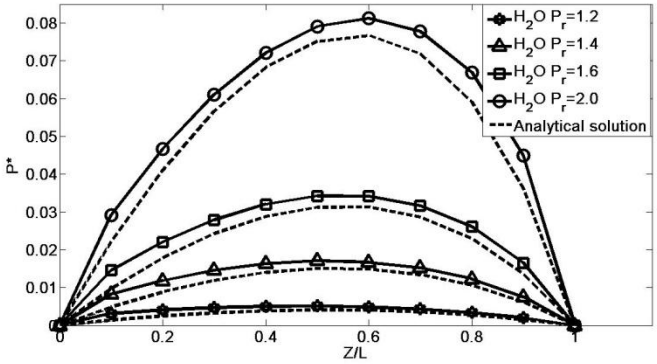

(c)

Figure 7. 7 Nonlinear pressure profiles for: (a) hydrogen with K_{n0}=0.10 and pressure ratio from 1.2 to 2.0; (b) oxygen with K_{n0}=0.055 and pressure ratio from 1.2 to 2.0; (c) water vapour K_{n0}=0.062413, pressure ratio from 1.2 to 2.0

Figures 7.7 (a-c) compare the analytical normalized pressure deviation distributions to the simulated pressure deviation distribution for the three gases under different pressure drops. They agree well.

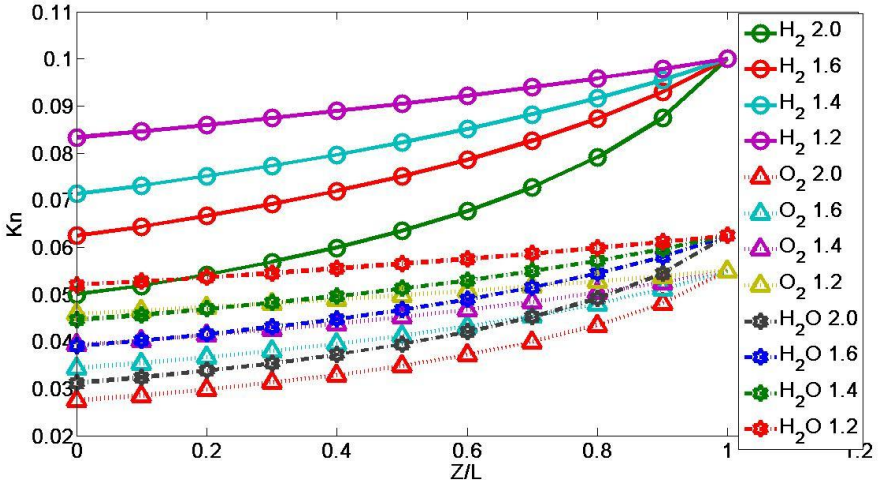

Figure 7. 8 Change of local K_n of the three gases along the tube under different P_r

Figure 7.8 shows the change of local Knudsen number along the tube under different pressure ratios for the three gases. As the pressure decreases from the inlet to the outlet, the gas density decreases. As a result, the Knudsen number also increases. For different the three gases, which have different out Knudsen number K_{no}, the increasing rate of K_n along the tube is different. For smaller outlet Knudsen K_{n0}, the increasing rate of K_n along the tune is slower even although the pressure ratio P_r is the same. For the same outlet Knudsen K_{n0}, the increasing rate of K_n along the tube increases with P_r.

7.5 Relationship between flow rate and pressure gradient

Under a given pressure gradient, the flow rate reflects the resistance of the material to gas flow. Since the size of the pores in catalyst layers is in nano scale, it is very difficult to measure the ability of the catalyst layer to conduct gases. The model presented in this work provides a way to qualitatively investigate the flow phenomena in nano-pores.

The Figure 7.9(a, b) shows the flow rate of hydrogen and oxygen through the tubes with different diameter. As shown in the figures, the flow rate increases with the tube diameter and pressure drop.

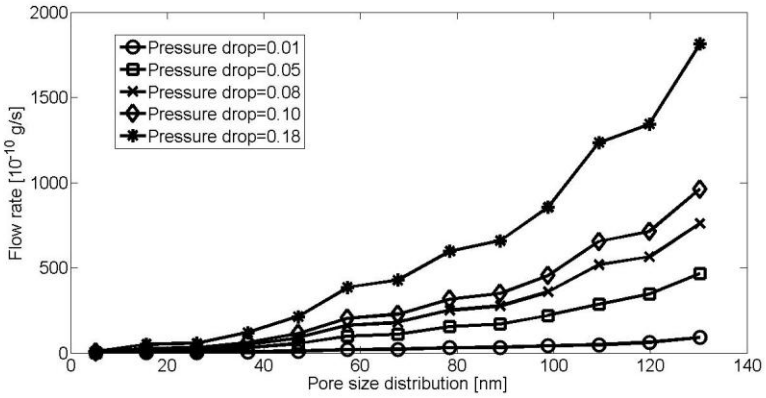

(a)

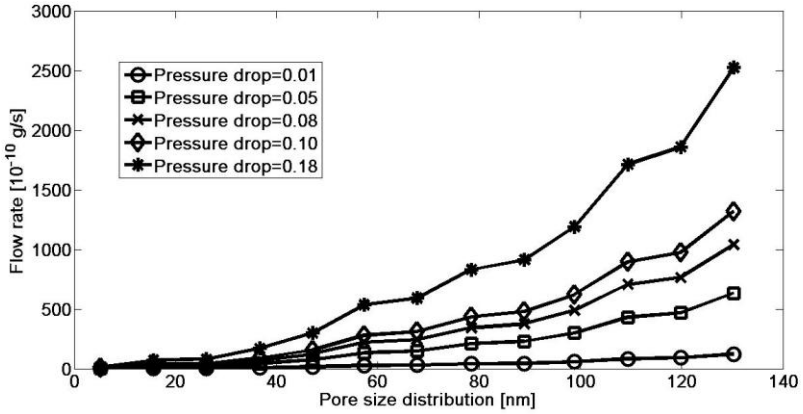

（b）

Figure 7. 9 The calculated gas flow rate under different pressure drops in the tubes estimated from the pore-size distribution of catalyst layer. (a) hydrogen, and (b) oxygen.

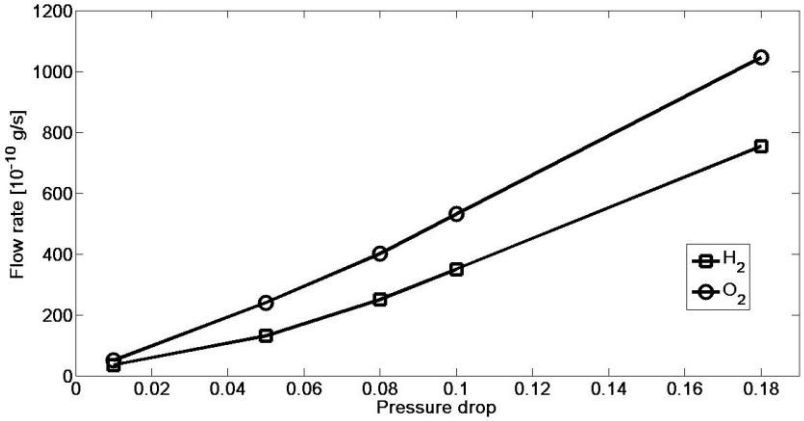

Figure 7. 10 Comparison of the simulated increase of flow rate with pressure drop for both hydrogen and oxygen.

Figure 7.10 shows the increase of flow rate through a unit area of the catalyst layer as the pressure drop increases. The flow rate is calculated by $Q = \sum_{i=1}^{n} q_i \times w_i / A$, with the value of A calculated by Equation (7.2). As shown in the figure, under the same pressure drop, the flow rate decreases when the *Kn* number increases from 0.055 to 0.1. Also seen from Figure 7.10 is that the increase of the flow rate with pressure drop is nonlinear, and the non-linearity increases with the Knudsen number.

7.6 Conclusions and discussion

This chapter presented a simplified model to simulate gas flow in nano-pores in an attempt to understand the flow behaviour when gas-wall collision frequency is comparable to gas-gas collision frequency for gas flow in the FEM catalyst layers. The complicated pore geometry in the catalyst layer is simplified into a bundle of tubes and the number and the diameters of the tubes are derived from the porosity and pore-size distribution. A lattice Boltzmann method is then presented to simulate gas flow in each tube. Summing up the flow rates in all the tubes could reveal how the nano-pores affect the gas flow behaviour in the catalyst layer. The impact of the Knudsen number on the dynamic properties of the gases is adsorbed in the relaxation time parameters, and the non-slip boundary was solved by a modified bounce–back method to yield a slip velocity at the gas-wall interface. The simulated results were validated against analytical solutions, and the comparison shows good agreement. The model was then applied to simulate gas flow in the simplified catalyst layer. The results reveal that, when the Knudsen number becomes significant, the flow rate through the catalyst layer is no longer linearly increases with presser gradient. With an increase in Knudsen number, the increase of flow rate with pressure gradient becomes increasing nonlinear.

This chapter aimed to shed some insight into gas flow in the catalyst layers. Although the catalyst layer is idealised, the results still has some implications. For example, it revealed that the permeability of the catalyst layer for hydrogen differs from its permeability for oxygen and water vapour due to the effect of gases-wall collision. Therefore, in macroscopic modelling the permeability of the catalyst layer for different gases and water should take different values.

Chapter 8 Conclusions and suggestions for future work

8.1 Conclusions

This PhD thesis used a combination of pore-scale lattice Boltzmann modelling and 3D x-ray computed tomography to simulate fluid flow in the GDL and CL at micro- and nano-scales. The simulated pore-scale velocity and pressure distribution were then used to calculate the macroscopic transport properties such as permeability and tortuosity. To test the feasibility of the methodology, we simulated fluid flow in a column packed with glass beads. The simulated permeability showed good agreement with the experimental measurements.

The commonly used LB models in the literature for pore-scale simulation are the single-relaxation time (also known as BGK model) and the multiple-relaxation time (MRT) model. The attraction of BGK model is its simplicity and computational efficiency. However, it cannot accurately solve the fluid-solid boundary if the relaxation time parameters is not properly selected, making it unfavourable to simulate fluid in porous media where fluid-wall interface dominates fluid flow. In contrast, the MRT model is more robust and can accurately solve the fluid-wall boundary. Its drawback is the highly computational cost, which is crucial in 3D simulations as a meaningful 3D simulation requires that the size of the sample should be sufficiently enough to be representative.

To compare the performance of the BGK and MRT models, we run a number of simulations using samples with various porosities ranging, approximately, from 0.35 to 0.8. The results show that the BGK model indeed gives rise to a permeability that increases, un-physically, with fluid viscosity due to its inaccuracy in solving fluid-solid boundary. In contrast, the permeability calculated by the MRT model is viscosity-independent. However, for all the media we simulated, the BGK model can calculate permeability with reasonably accuracy when using unity relaxation time parameters. Since the computational efficiency of BGK model can be further increased when unity relaxation time parameter is used, we concluded that, for calculating medium permeability, BGK model is more attractive than MRT because it uses only one third of the computational time of the MRT model. However, if the pore-scale velocity and pressure distribution are also a concern, MRT model might be preferred to the BGK model.

Building on this, we simulated the impact of compression on gas flow in GDL and its consequent effect on fuel cell performance. The power output of a single cell is limited, and in practice, a number of cells are often stacked. As such, the GDLs are compressed. Binary x-ray images under different pressures in the range from 0.3 MPa to 20 MPa were acquired. Gas flow in both through-plane direction and in-plane directions in the GDLs was simulated using the developed LB model. The simulated results show that the permeability in both in-plane direction and through-plane significantly decreases with compression. The decrease of the permeability with the porosity of the GDLS due to compression can be well described by empirical formulae. These findings will provide guidance to fuel design.

The electrochemical reactions at both anode and cathode take place inside the catalyst layer lying between the membrane and the gas diffusion layer. Unlike the GDL, the pore size in the catalyst layer is less than one micron and gas flow through it is more complicated than that in the GDL. In the CL, the gas-wall collision frequency is comparable to gas-gas collision frequency. As a result, the dynamic property of the gas in the CL is no longer able to be described by a single viscosity; it also depends on gas-wall collision frequency. Simulation of gases in such media is challenging, and the available models are still in their infancy. Attempt was made in this thesis to use the LB model to simulate gas flow in the catalyst layer. The idea is similar to the network model. The complicated pore geometry was idealised into a bundle of tubes; the number of the tubes and the diameter of each tube were determined for the pore-size distribution and the porosity, which are calculated from the 3D images. We developed a LB model to simulate gas flow each tube pipes, and the preliminary results show some encouragement.

Another issue in PEM fuel cells is liquid water. At the cathode, the oxygen is firstly reduced, and then reacts with electrons and the protons to form water in the catalyst layer. The oxygen is supplied from the channel in the bipolar pales; it flows from the channel to the catalyst layer, via the GDL. On the one hand, the electrochemically reaction requires continuous supply of oxygen to the catalyst layer. On the other hand, the accumulation of water at the cathode will result in flooding, thereby blocking the pathway of the oxygen. To avoid flooding, the water must be drained out of the catalyst and gas diffusion layers, and the water drainage should not block the pathways for oxygen to flow from the channel to the catalyst layer. To achieve this, the GDLs at the cathode are often made heterogeneously hydrophobic in that some areas in the GDL are hydrophobic and some

areas are hydrophilic. This could enforce the water to flow only along a number of channels from the catalyst layer to the gas supply channel, leaning other space for oxygen to diffuse in the opposite direction. As such, the impact of hydrophobicity on water flow is critical to fuel cell performance. We developed a two-phase LB model to simulate water flow in GDLs with various hydrophobicities in an attempt to investigate how hydrophobic degree affects flow pattern. The results indicated that, in a hydrophilic GDL the water flows like a piston flow, occupying all the available void area, leaving no area for oxygen to diffuse. When GDL changes from hydrophilicity to hydrophobicity, water flow changes from piston-type flow to channelled-type flow, leaving some space for gas to diffuse.

8.2 Suggestions for future work

All the simulations carried out in this work were run using a PC working station. There was a limitation on the size of the 3D samples. As a result, the simulated results might not be very representative. This limitation could be overcome by using super-computers. Apart from this, there are some other issues that need further work.

The first one is to extend the LB model to include multiple components, which, at the anode, include hydrogen and water vapour; and at the cathode, include oxygen, nitrogen and water vapour. What is particularly important is how a change in liquid water affects the movement of these gases at the cathode as the electrochemical reactions at the cathode are more sluggish. Preliminary study had been carried out by project partners, but their work did consider liquid water at the cathode. Combing it with the work presented in this paper will further improve our understanding of the complicated transport processes in fuel cells.

Another is that the model for gas flow with the Knudsen number in consideration idealised the pore geometry. Although the simulated results show good agreement with the analytical solutions, the flow domain is restricted to simple pipe. Method has been proposed to extend this simple pipe model to network model, but its verification needs further work as experimentally measuring flow process in nano-scale is a challenge.

The third one is that the two-phase model we used for simulating water flow in the GDL was based on the model developed by Shan and Chen [137]. This is a phenomenal model and cannot simulate fluids with high density ratio due to the limitation of numerical

stability. Such a model might work for GDL as the capillary force is the dominant force for water flow in the GDL. However, such model cannot extend to the gas-supply channel as the capillary force in no longer the dominant force in the channels. Two-phase LB models that are able to deal with fluids with high density ratio have been developed, but all of them need to calculate second-order spatial derivatives. This makes them less favourable to be used in GDL because of numerical stability.

References

1. EG&G Technical Services, I.S.A.I.C., *Fuel Cell Handbook (Sixth Edition)*. 2002: DIANE Publishing.
2. Li, X., *Principles of Fuel Cells*. 2006, New York: Taylor & Francis.
3. Zhang, J., *PEM Fuel Cell Electrocatalysts and Catalyst Layers: Fundamentals and Applications*. 2008: Springer. 1137.
4. Tawfik, H., Y. Hung, and D. Mahajan, *Metal bipolar plates for PEM fuel cell-A review.* Journal of Power Sources, 2007. **163**: p. 755-767.
5. Davies, H., Y. Hung, and D. Mahajan, *Bipolar plate materials for solid polymer fuel cells.* Journal of Applied Electrochemistry, 2000. **30**: p. 101-105.
6. Mathias, M.F., et al., *Diffusion media materials and characterization*, in *Handbook of Fuel Cells-Fundamentals, Technology and Applications*, W. Vielstich, H.A. Gasteiger, and A. Lamm, Editors. 2003, John Wiley & Sons: New York. p. 517-537.
7. Zhong, C.J., et al., *Nanostructure catalysts in fuel cells.* Nanotechnology, 2010. **21**: p. 1-20.
8. Barbir, F., *PEM Fuel Cell: Theory and Practice*. 2005, London: Elsevier Academic Press.
9. Schulze, M., A. Schneider, and E. Gulzow, *Alteration of the distribution of the platinum catalyst in membrane-electrode assemblies during PEFC operation.* Journal of Power Sources, 2004. **127**: p. 213-221.
10. Benziger, J., et al., *Water flow in the gas diffusion layer of PEM fuel cells.* Journal of Membrane Science, 2005. **261**(1-2): p. 98-106.
11. Bernardi, D.M. and M.W. Verbrugge, *Mathematical Model of a Gas Diffusion Electrode Bonded to a Polymer Electrolyte.* Am.Inst.Chem.Eng.J., 1991. **37**: p. 1151-1163.
12. Bernardi, D.M. and M.W. Verbrugge, *Mathematical Model of the Solid-polymer Electrolyte Fuel Cell.* j.Electrochem.Soc., 1992. **139**: p. 2477-2491.
13. Springer, T.E., J.T.A. Zawodzinski, and S. Gottesfeld, *Polymer Electrolyte Fuel Cell Model.* J.Electrochem.Soc., 1991. **138**: p. 2334-2341.

14. Wang, C.Y. and P. Cheng, *Multiphase flow and heat transfer in porous media.* Advances in Heat Transfer, 1997. **30**: p. 193-196.
15. Wang, C.-Y., *Fundamental models for fuel cell engineering.* Chemical Reviews, 2004. **104**(10): p. 4727-4765.
16. Wang, C.Y. and P. Cheng, *A multiphase mixture model for multiphase,multicomponent transport in capillary porous media-1 Model development.* International Journal of Heat and Mass Transfer, 1996. **39**(17): p. 3607-3618.
17. Shah, A.A., et al., *Recent trends and developments in polymer electrolyte membrane fuel cell modelling.* Electrochimica Acta, 2010. **56**: p. 3731-3757.
18. Gurau, V., H.T. Liu, and S. Kakac, *Two-dimensional model for proton exchange membrane fuel cells.* AIChE Journal, 1998. **44**(11): p. 2410-2422.
19. Siegel, N.P., et al., *Single domain PEMFC model based on agglomerate catalyst geometry.* Journal of Power Sources, 2003. **115**(1): p. 81-89.
20. Mazumder, S. and J.V. Cole, *Rigorous 3D mathematical modeling of PEM fuel cells.* Journal of the Electrochemical Society, 2003. **150**(11): p. 1510-A1517.
21. Nam, H.M. and M. Kaviany, *Effective diffusiveity and water saturation distribution in single and two layer PEMFC diffusion medium.* International Journal of Heat and Mass Transfer, 2003. **46**: p. 4595-4611.
22. Lee, K.J., J.H. Nam, and C.J. Kim, *Pore network analysis of two-phase water transport in gas diffusion layers of polymer electrolyte membrane fuel cells.* Electrochinica Acta, 2009. **54**: p. 1166-1176.
23. Sinha, P.K., P.P. Mukherjee, and C.Y. Wang, *Impact of GDL strucrture and wettability on water management in polymer electrolyte fuel cells.* journal of Materials Chemistry, 2007a. **17**: p. 3089-3103.
24. Koido, T., T. Furusawa, and K. Moriyama, *An approach to modeling two phase transport in the gas diffusion layer of a proton exchange membrane fuel cell.* Journal of Power Sources, 2008. **175**: p. 127-136.
25. Sinha, P.K. and C.Y. Wang, *Pore-network modeling of liquid water transport in gas diffusion layer of a polymer electrolyte fuel cell.* Electrochimica Acta, 2007b. **52**: p. 7936-7945.
26. Gostick, J.T., et al., *Pore network modeling of fibrous gas diffusion layers for polymer electrolyte membrane fuel cells.* Journal of Power Sources, 2007. **173**: p. 277-290.

27. Chen, S.Y. and G.D. Doolen, *Lattice Boltzmann method for fluid flows.* Annual Review of Fluid Mechanics, 1998b. **30**: p. 329-364.
28. Niu, X.D., et al., *An investigation of water gas transport processes in the gas diffusion layer of a PEM fuel cell by a multiphase multiple relaxation time lattice Boltzmann model.* Journal of Power Sources, 2007. **172**: p. 542-552.
29. Park, J., Matsubara, M. , Li, X. , *Application of lattice Boltzmann method to a micro-scale flow simulation in the porous electrode of a PEM fuel cell.* J. Power Sources, 2007: p. 404-414.
30. Park, J., Li, X. , *Multi-phase micro-scale flow simulation in the electrodes of a PEM fuel cell by lattice Boltzmann method.* Journal of Power Sources, 2008: p. 248-257.
31. Mukherjee, P.P., C.Y. Wang, and Q. Kang, *Mesoscopic modeling of two-phase behavior and flooding phenomena in polymer electrolyte fuel cells.* Electrochimica Acta, 2009b. **54**(27): p. 6861-6875.
32. Hao, L. and P. Cheng, *Lattice Boltzmann simulations of water transport in gas diffusion layer of a polymer electrolyte membrane fuel cell.* Journal of Power Sources, 2010. **195**: p. 3870-3881.
33. Hao, L. and P. Cheng, *Lattice Boltzmann simulation of liquid droplet dynamic behaviour on a hydrophobic surface of a gas flow channel.* J.Power Sources, 2009. **435-466**.
34. Rama, P., et al., *Multiscale Modeling of Single-Phase Multicomponent Transport in the Cathode Gas Diffusion Layer of a Polymer Electrolyte Fuel Cell.* Energy & Fuels, 2010. **24**: p. 3130-3143.
35. Joshi, A.S., et al., *Lattice Boltzmann modeling of 2D gas transport in a solid oxide fuel cell anode.* Journal of Power Sources, 2007. **164**(2): p. 631-638.
36. Zhou, P. and C.W. Wu, *Liquid water transport mechanism in the gas diffusion layer*. Journal of Power Sources, 2010. **195**(5): p. 1408-1415.
37. Park, J. and X. Li, *Multi-phase micro-scale flow simulation in the electrodes of a PEM fuel cell by lattice Boltzmann method.* Journal of Power Sources, 2008. **178**(1): p. 248-257.
38. Auzerais, F.M., et al., *Transport in sandstone: A study based on three dimensional microtomography*. Geophys.Res.Lett., 1996. **23**: p. 705-708.
39. Flannery, B.P., et al., *Three-Dimensional X-ray Microtomography.* Science, 1987. **237**: p. 1439-1444.

40. Spanne, P., et al., *Synchrotron computed microtomography of porous meida-Topology and transports.* Phys.Rev.Lett., 1994. **73**: p. 2001-2004.
41. Wildenschild, D., et al., *Quantitative analysis of flow processes in a sand using synchrotron-based X-ray microtomography.* Vadose Zone J., 2005. **4**: p. 112-126.
42. Haddad, W.S., et al., *Ultrahigh-Resolution X-ray Tomography.* Science, 1994. **266**: p. 1213-1215.
43. Herman, G.T., *Image Reconstruction from Projections -The Fundamentals of Computerized Tomography*. 1980, USA: Academic Press.
44. Leonard, A., et al., *Image analysis of X-ray microtomograms of soft materials during convective drying.* Journal of Microscopy, 2003. **212**: p. 197-204.
45. Sasov, A. *X-ray microtomography of plastics and composite materials, Developments in X-ray tomography* in *proceedings of the Society of Photo optical instrumentation engineers (SPIE).* 2002.
46. SkyScan, *SkyScan 1172 desktop X-ray microtomography.* 2005.
47. SkyScan, *SkyScan 1072 desktop X-ray microtography user maunal*. 2008.
48. SkyScan, *SkyScan 2011 desktop X-ray nanotomgraphy user manual.* 2009.
49. Lorensen, W.E. and H.E. Cline, *Marching cubes: a high resolution 3D surface construction algorithm.* Computer Graphics, 1987. **21**: p. 163-169.
50. Bouvier, D.J., *Double time cubes:a fast surface construction algorithm for volume visualization*. 2000, Uiniversity of Arkansas, 313 Engineering Hall: Fayetteville.
51. Manke, I., et al., *Investigation of water evolution and transport in fuel cells with high resolution synchrotron x-ray radiography.* App.Phys.Lett., 2007. **90**(17): p. 174501-174505.
52. Feser, J.P., A.K. Prasad, and S.G. Advani, *Experimental characterization of in-plane permeability of gas diffusion layers.* J. Power Sources, 2006. **161**: p. 1226-1231.
53. Hung, T.F., et al., *Highly efficient single-layer gas diffusion layers for the pronton exchange membrane fuel cell.* J.Power Sources, 2008. **184**(1): p. 165-171.
54. Ostadi, H., et al., *Nanotomography based study of gas diffusion layers.* Microelectron. Eng., 2010a. **87**(5-8): p. 1640-1642.
55. Frisch, U., B. Hasslacher, and Y. Pomeau, *Lattice-gas automata for the Navier-Stokes equation.* Phys. Rev. Lett., 1986. **56**: p. 1505-1508.
56. Hazi, G., et al., *Lattice Boltzmann methods for two phase flow modelling.* Ann.Nuclear Energy, 2002. **29**: p. 1421-1453.

57. Nourgaliev, R.R., et al., *The lattice Boltzmann equation method: throretical interpretation, numerics and implications.* Int.J.Multiphase Flow, 2003. **29**: p. 117-169.

58. Raabe, D., *Overview of the lattice Boltzmann method for nano and microscale fluid dynamics in materials science and engineering.* Modelling Simu.Mater.Sci.Eng., 2004. **12**: p. R13-R46.

59. Pan, Y., Horne, R. N. , *Generalized Macroscopic Models for Fluid Flow in Deformable Porous Media II: Numerical Results and Applications.* Transport in Porous Media, 2001: p. 195-213.

60. Shamsai, A., Vosoughifar, H.R., *Finite Volume Discretization of Flow in porous media by the matlab system.* Seientia iranica, 2004: p. 146-153.

61. Juanes, R., *A variational multiscale finite element method for multiphase flow in porous media.* Finite Elements in Analysis and Design, 2005: p. 763-777.

62. Sivertsen, B.R., Djilali, N. , *CFD-based modelling of proton exchange membrane fuel cells.* Journal of Power sources, 2005. **141**: p. 65-78.

63. Joshi, A.S., et al., *Lattice Boltzmann Modeling of 2D Gas Transport in a Solid Oxide Fuel Cell Anode.* J. Power Sources, 2007. **164**: p. 631-638.

64. McNamara, G.R. and G. Zanetti, *Use of the Boltzmann equation to simulate lattice gas automata.* Phys.Rev.Lett, 1988. **61**(20).

65. Qian, Y.H., D. Dhumieres, and P. Lallemand, *LATTICE BGK MODELS FOR NAVIER-STOKES EQUATION.* Europhysics Letters, 1992. **17**(6BIS): p. 479-484.

66. d'Humieres, D., et al., *Multiple-relaxation-time lattice Boltzmann models in three dimensions.* Philosophical Transactions of the Royal Society of London Series a-Mathematical Physical and Engineering Sciences, 2002. **360**(1792): p. 437-451.

67. Pan, C., Luo, L.-S., *An evaluation of lattice Boltzmann schemes for porous medium flow simulation.* Computers & Fluids, 2006. **35**: p. 898-909.

68. He, X.Y., et al., *Analytic solutions of simple flows and analysis of nonslip boundary conditions for the lattice Boltzmann BGK model.* Journal of Statistical Physics, 1997. **87**(1-2): p. 115-136.

69. He, X., et al., *Analytical solutions and analysis on non-slip boundary condition for lattice Boltzmann BGK model.* J Stat Phys, 1997b. **97**: p. 115-136.

70. Zhang, X.X., et al., *Determination of soil hydraulic conductivity with the lattice Boltzmann method and soil thin-section technique.* Journal of Hydrology, 2005. **306**(1-4): p. 59-70.

71. Chen, C., A.I. Packman, and J.F. Gaillard, *Pore-scale analysis of permeability reduction resulting from colloid deposition.* Geophysical Research Letters, 2008. **35**(7).

72. Dreweke, A., *Lattice Boltzmann method for DSM systems:Implementation and optimization with JAVA*. 2008, Saarbrucken,Germany: VDM Verlag.

73. Koelman, J.M.V.A., *A simple lattice Boltzmann scheme for Navier-Stokes fluid flow*. Europhys Letts., 1991. **15**(6): p. 603-607.

74. He, X. and G. Doolen, *LatticeBoltzmannMethod on CurvilinearCoordinates System: Flowarounda Circular Cylinder.* Journal of Computational Physics, 2002a. **134**(2): p. 306-315.

75. Frisch, U., et al., *Lattice gas hydrodynamics in two and three dimensions.* Complex Systems, 1987. **1**: p. 649-707.

76. Wolf-Gladrow, D.A., *Lattice-Gas Cellular Automata and Lattice Boltzmann Models*. Springer. 2000. 308.

77. Succi, S., *The Lattice Boltzmann Equation For Fluid Dynamics and Beyond*. 2001: Oxford University Press.

78. D'Humieres, D., *Generalized lattice Boltzmann equations*, in *Rarefied gas dynamics:theory and simulations*, B.D. Shizgal and D.P. Weaver, Editors. 1992, Prog Aeronaut Astronaut. p. 450-458.

79. Lallemand, P. and L.S. Luo, *Theory of the lattice Boltzmann method: dispersion, dissipation, isotropy, Galilean invariance and stability.* Phys. Rev. E., 2000. **61**: p. 6546-6562.

80. Lallemand, P., et al., *Theory of the lattice Boltzmann method: Three dimensional model for viscoelastic fluid.* Physical Review E, 2003. **67**(2): p. 021203.

81. Maier, R.S., R.S. Bernard, and D.W. Grunau, *Boundary conditions for the lattice Boltzmann method.* Phys.Fluids, 1996. **8**(7): p. 1788-1801.

82. Ziegler, D.P., *Boundary conditions for lattice Boltzmann simulations.* Journal of Statistical Physics, 1993. **71**(5-6): p. 1171-1177.

83. Ginzbourg, I. and D. D'Humieres, *Local second-order boundary methods for lattice Boltzmann models.* J.Stat.Phys., 1995. **84**: p. 927-971.

84. Aidun, C.K. and J.R. Clausen, *Lattice Boltzmann method for complex flows.* Annual Review of Fluid Mechanics, 2010. **42**(1): p. 439-472.

85. Gallivan, M., et al., *An evaluation of bounce back boundary condition for lattice Boltzmann simulations.* Int.J.Numer.Meth.Fluids, 1997. **25**(3): p. 249-263.

86. He, X., et al., *Some progress in the lattice Boltzmann method. Part I, non-uniform mesh grids.* J.Comp.Phys., 1996. **129**: p. 357-363.

87. Kandhai, D., et al., *Implementation aspects of 3D lattice-BGK: Bundaries, accuracy and a new fast relaxation method.* J.Comp.Phys., 1999. **150**: p. 482-501.

88. Guo, Z., C. Zheng, and B. Shi, *Discrete lattice effects on the forcing term in the lattice Boltzmann method.* Phys.Rev.E, 2002. **65**(4): p. 046308.

89. Verberg, R. and A.J.C. Ladd, *Accuracy and stability of a lattice Boltzmann model with subgrid scale boundary conditions.* Phys.Rev.E, 2001. **65**: p. 016701.

90. Chen, H., C. Teixeira, and K. Molving, *Realization of Fluid Boundary Condition via Discrete Boltzmann Dynamics.* Int.J.Modern Phys.C, 1998a. **9**(8): p. 1281-1292.

91. Filippova, O. and D. Hanel, *Boundary fitting and local grid refinement for lattice BGK models.* Int.J.Modern Phys.C, 1998. **9**(8): p. 1271-1280.

92. Zou, Q.S. and X.Y. He, *On pressure and velocity boundary conditions for the lattice Boltzmann BGK model.* Phys. Fluids, 1997. **9**(6): p. 1591-1598.

93. Zhou, Q., He, X., *On pressure and velocity boundary conditions for the lattice Boltzmann BGK model.* Phys. Fluids, 1997. **9**(6): p. 1591-1598.

94. Wang, L.P., Afsharpoya, B. , *Modeling fluid flow in fuel cells using the lattice-Boltzmann approach.* Mathematics and Computers in Simulation, 2006: p. 242-248.

95. Berryman, J.G., Blair, S.C. , *Using of digital image analysis to estimate fluid permeability of porou materials: Application of two-point correlation functions.* J.Appl.Phys., 1986: p. 1930-1938.

96. Zhang, D.X., et al., *Pore scale study of flow in porous media: Scale dependency, REV, and statistical REV.* Geophys. Res. Lett., 2000. **27**: p. 1195-1198.

97. Fredrich, J.T., Digiovanni, A.A. , *Predicting macroscopic transport properties using microscopic image data.* J.Geo-phys.Res., 2006. **111**: p. B03201.

98. Clague, D.S., Kandhai, B.D. , Zhang, R., Sloot, P.M.A., *Hydraulic permeability of (un)bounded fibrous media using the lattice Boltzmann method.* Phys. Rev. E, 2000: p. 616-625.

99. Pan, C.X., L.S. Luo, and C.T. Miller, *An evaluation of lattice Boltzmann schemes for porous medium flow simulation.* Computers & Fluids, 2006. **35**(8-9): p. 898-909.

100. He, X. and L.S. Luo, *Theory of the lattice Boltzmann method:from the Boltzmann equation to the lattice Boltzmann equation.* Phys.Rev.E, 1997a. **56**: p. 6811-6817.

101. Ostadi, H., et al., *Nanotomography based study of gas diffusion layers.* Microelectron. Eng., 2010. **87**(5-8): p. 1640-1642.

102. Chen, C., A.I. Packman, and J.F. Gaillard, *Pore-scale analysis of permeability reduction resulting from colloid deposition.* Geophys. Res. Lett., 2008. **35**: p. L07404.

103. Kozeny, J., *Uber Kapillare leitung des wassers im boden.* Sitzungsber.Akad.Wiss.Wien, 1927. **136**: p. 271-306.

104. Carman, P., *Fluid flow through a granular bed.* Trans.Inst.Chem.Eng., 1937. **15**: p. 150-167.

105. Bosl, W.J., Dvorkin, J. , Nur. A. , *A study of porosity and permeability using a lattice Boltzmann simulation.* Geohpys.Res.Lett. , 1998. **25**: p. 1475-1478.

106. Costa, A., *permeability-porosity relationship: A rexamation of the Kozeny-carman equation based on a fractal pore-space geometry assumption.* Geophys.Res.Lett., 2006. **33**: p. L02318.

107. Wittmann-Teneze, K., Caron, N., Alexandre, S., *Gas permeability of porous plasma-sprayed coatings.* Journal of thermal spray technology, 2008. **17 (5-6)**: p. 902-907.

108. Zhan, Z.G., Xiao, J.S., Li, D.Y., Pan, M., Yuan, R.Z., *Effects of porosity distribution variation on the liquid water flux through Gas Diffusion layers of PEM fuel cells.* J. Power Sources, 2006. **160**: p. 1041-1048.

109. Rama, P., et al., *An X-Ray Tomography Based Lattice-Boltzmann Simulation Study on Gas Diffusion Layers of Polymer Electrolyte Fuel Cells.* J. Fuel Cell Sci. Technol., 2010b. **7**(3): p. 031015

110. Tomadakis, M.M. and T.J. Robertson, *Viscous Permeability of Random Fiber Structures: Comparison of Electrical and Diffusional Estimates with Experimental and Analytical Results.* Journal of Composite Materials 2005. **39**(2): p. 163-188.

111. Tomadakis, M.M. and S.V. Sotirchos, *Ordinary and Transition Rdgime Diffusion in Random Fiber Structure.* AIChE J., 1993. **39**: p. 397-412.

112. Gostick, J.T., et al., *In-plane and through-plane gas permeability of carbon fiber electrode backing layers.* J. Power Sources, 2006b. **162**(1): p. 228-238.

113. Nabovati, A. and A.C.M. Sousa, *Fluid flow simulation in random porous media at pore level using the Lattice Boltzmann method.* Journal of Engineering Science and Technology, 2007. **2**(3): p. 226-237.

114. Hottinen, T. and O. Himanen, *PEMFC temperature distribution caused by inhomogeneous compression of GDL.* Electrochemistry Communications, 2007. **9**(5): p. 1047-1052.

115. Ge, J., A. Higier, and H. Liu, *Effect of gas diffusion layer compression on PEM fuel cell performance.* Journal of Power Sources, 2006. **159**(2): p. 922-927.

116. Bazylak, A., et al., *Effect of compression on liquid water transport and microstructure of PEMFC gas diffusion layers.* Journal of Power Sources, 2007. **163**(2): p. 784-792.

117. Escribano, S., et al., *Characterization of PEMFCs gas diffusion layers properties.* Journal of Power Sources, 2006. **156**(1): p. 8-13.

118. Nitta, I., et al., *Inhomogeneous compression of PEMFC gas diffusion layer: Part I. Experimental.* Journal of Power Sources, 2007. **171**(1): p. 26-36.

119. Lee, W.K., et al., *The effects of compression and gas diffusion layers on the performance of a PEM fuel cell.* Journal of Power Sources, 1999. **84**: p. 45-51.

120. Lin, J.H., et al., *Effect of gas diffusion layer compression on the performance in a proton exchange membrane fuel cell.* Fuel Cells, 2008. **87**: p. 2420-2424.

121. Lee, T. and C.L. Lin, *A stable discretization of the lattice Boltzmann equation for simulation of incompressible two-phase flows at high density ratio.* J.Comput.Phys., 2005b. **206**(1): p. 16-47.

122. Chi, P.H., et al., *On the effects of non-uniform property distribution due to compression in the gas diffusion layer of a PEMFC.* International Journal of Hydrogen Energy, 2009. **doi:10.1016/j.ijhydene.2009.05.066**.

123. Zhou, P. and C.W. Wu, *Numerical study on the compression effect of gas diffusion layer on PEMFC performance.* Journal of Power Sources, 2007. **170**: p. 93-100.

124. Williams, M., V., H.R. Kunz, and J. Fenton, M., *Influence of Convection Through Gas-Diffusion Layers on Limiting Current in PEM FCs Using a Serpentine Flow Field.* J.Electrochem.Soc. , 2004a. **151**(10): p. A1617-A1627.

125. Hussaini, I.S. and C.Y. Wang, *Measurement of Relative Permeability of Fuel Cell Diffusion Media.* J. Power Sources, 2010a. **195**: p. 3830-3840.

126. Gurau, V., et al., *Characterization of transport properties in gas diffusion layers for proton exchange membrane fuel cell:2.Absolute permeability.* J.Power Sources, 2007. **165**(2): p. 793-802.

127. Pasaogullari, U., et al., *Anisotropic Heat Water Transport in a PEFC Cathode Gas Diffusion Layer.* Journal of Electrochemical Society, 2007. **154**(8): p. B823-B834.

128. Mukundan, R. and R.L. Borup, *Visualising liquid water in PEM Fuel Cells Using Neutron Imaging.* Fuel Cells, 2009. **9**(5).

129. Gao, Y., et al., *Modeling Fluid Flowin the Gas Diffusion Layers in PEMFC Using theMultiple Relaxation-time Lattice Boltzmann Method.* Fuel Cells, 2012b. **DOI: 10.1002/fuce.201000074**.

130. Rothman, D.H. and J.M. Keller, *Immiscible cellular-automaton fluids.* J.Stat.Phys., 1988. **52**(3-4).

131. Gunstensen, A.K., et al., *Lattice Boltzmann model of immiscible fluids.* Phys.Rev.A., 1991. **43**(8): p. 4320-4327.

132. Gunstensen, A.K. and D.H. Rothman, *Microscopic Modeling of Immiscible Fluids in Three Dimensions by a Lattice Boltzmann Method* Europhysics Letters, 1992. **18**(2).

133. Higuera, F.J. and J. Jimenez, *Boltzmann Approach to Lattice Gas Simulations.* Europhysics Letters, 1989. **9**(7): p. 663-668.

134. He, X. and G.D. Doolen, *Thermodynamics foundations of kinetic theory and lattice boltzmann models for multiphase flows.* J.Stat.Phys., 2002b. **107**(1-2): p. 309-328.

135. Grunau, D.W., S.Y. Chen, and K. Eggert, *A lattice Boltzmann model for multiphase fluid flows.* Phys.Rev.A., 1993a. **5**(10): p. 2557-2563.

136. Ahrenholz, B., et al., *Prediction of Capillary hysteresis in a porous material using lattice Boltzmann methods and comparison to experimental data and a morphological pore network model.* Advances in Water Resources, 2008. **31**: p. 1151-1173.

137. Shan, X. and H. Chen, *Lattice Boltzmann model for simulating flows with multiple phases and components.* Phys.Rev.E., 1993. **47**(3).

138. Shan, X. and H. Chen, *Simulation of nonideal gases and liquid-gas phase transitions by the lattice Boltzmann equation.* PHys.Rev.E., 1994. **49**(4): p. 2941-2948.

139. Shan, X. and G.D. Doolen, *Diffusion in a multi-component lattie Boltzmann equation model.* phys.Rev.E., 1996. **54**(4): p. 3614-3620.

140. Martys, N. and J.F. Douglas, *Critical properties and phase separation in lattice Boltzmann fluid mixtures.* PHys.Rev.E., 2001. **63**(3): p. 031205.

141. Hou, S.L., et al., *Evaluation of two lattice Boltzmann models for multiphase flows.* J.Comput.Phys., 1997. **138**(2): p. 695-713.

142. Leclaire, S., M. Reggio, and J.-Y. Trepanier, *Numerical evaluation of two recoloring operators for an immiscible two-phase flow lattice Boltzmann model.* Applied Mathematical Modelling, 2012. **36**(5): p. 2237-2252.

143. Huang, H., L. Wang, and X.-y. Lu, *Evaluation of three lattice Boltzmann models for multiphase flows in porous media.* Computers and Mathematics with Applications, 2011. **61**(12): p. 3606-3617.

144. Swift, M.R., W.R. Osborn, and J.M. Yeomans, *Lattice Boltzmann simulation of nonideal fluids.* Phys.Rev.Lett, 1995. **75**(5): p. 5041-5052.

145. Swift, M.R., W.R. Osborn, and J.M. Yeomans, *Lattice Boltzmann simulations of liquid-gas and binary fluid systems.* Phys.Rev.E., 1996. **54**(5): p. 5041-5052.

146. He, X., S. Chen, and R. Zhang, *A lattice Boltzmann scheme for incompressible multiphase flow and its application in simulation of Rayleigh-Taylor instability.* J.Comput.Phys., 1999. **152**(2): p. 642-663.

147. Zheng, H.W., C. Shu, and Y.T. Chew, *A lattice Boltzmann model for multiphase flows with large density ratio.* Journal of Computational Physics, 2006. **218**(1): p. 353-371.

148. Inamuro, T., et al., *A lattice Boltzmann method for incompressible two-phase flows with large density differences.* Journal of Computational Physics, 2004. **198**(2): p. 628-644.

149. Martys, N.S. and H.D. Chen, *Simulation of multicomponent fluids in complex three-dimensional geometries by the lattice Boltzmann method.* Phys. Rev. E, 1996. **53**(1): p. 743-750.

150. Yu, Z. and L.-S. Fan, *An interaction potential based lattice Boltzmann method with adaptive mesh refinement (AMR) for two-phase flow simulation.* Journal of Computational Physics, 2009. **228**(17): p. 6456-6478.

151. Arkilic, E.B., K.S. Breuer, and M.A. Schmidt. *Gaseous Flow in Microchannels*. in *International Mechnical Engineering Congress and exposition ASME*. 1994. Chicago.

152. Karniadakis, G., A. Beskok, and N. Aluru, *Microflows and Nanoflows:Fundamentals and simulations*. 2005, New York: Springer.

153. Karniadakis, G., A. Beskok, and N. Aluru, *Microflows and Nanoflows: Fundamentals and Simulations*. 2005, New York: Springer.

154. Nie, X., G.D. Dollen, and S. Chen, *Lattice Boltzmann simulations of fluid flow in MEMs.* Journal of Statistical Physics, 2002. **107**: p. 279-289.

155. Nie, X., G.D. Doolen, and S. Chen, *Lattice Boltzmann simulations of fluid flow in MEMs.* Journal of Statistical Physics, 2002a. **107**: p. 279-289.

156. Bruus, H., *Theoretical microfluidics*. Oxford master series in physics. 2008, Oxford: Oxford University Press.

157. Kockmann, N., *Transport phenomena in micro process engineering*. 2008, Berlin: Springer.

158. Dietrich, T.R., *Microchemical engineering in practice*. 2009, Oxford: Wiley.

159. Whitesides, G.M., *The origins and the future of microfluidics.* Nature, 2006. **442**(7101): p. 368-373.

160. Lim, C., *Application of lattice Boltzmann method to simulate microchannel flows.* Physics of fluids, 2002. **14**(7): p. 2299-2308.

161. Tang, G., W. Tao, and Y. He, *Gas flow study in MEMs using lattice Boltzmann method*, in *1st International Conference on Microchannels and Minichannels*. 2004, ASME: New York.

162. Tang, G., W. Tao, and Y. He, *Lattice Boltzmann model for incompressible flows through porous media.* Journal of Applied physics, 2005. **97**(10).

163. Tang, G., W. Tao, and Y. He, *Three dimensional lattice Boltzmann model for gaseous flow in rectangular microducts and microscale porous media.* Journal of Applied physics, 2005a. **97**(10).

164. Shen, C., et al., *Examination of the LBM in simulation of microchannel flow in transitional regime.* Microscale Thermophysical Engineering, 2004. **8**: p. 423-432.

165. Shen, C., et al., *Examination of the LBM in simulation of microchannel flow in transitional regime.* Microscale Thermophysical Engineering, 2004. **8**(4): p. 423-432.

166. Lee, T. and C.L. Lin, *Rarefaction and compressibility effects of the lattice Boltzmann equation method in a gas microchannel.* Phys.Rev.E., 2005. **71**: p. 046706.

167. Lee, T. and C.L. Lin, *Rarefaction and compressibility effects of the lattice BOltzmann equation metod in a gas microchannel.* Phys.Rew.E, 2005. **71**(4): p. 046706.

168. Arkilic, E.B. and M.A. Schmidt, *Gaseous Slip Flow in Long Microchannels.* JOURNAL OF MICROELECTROMECHANICAL SYSTEMS, 1997. **6**(2).

169. Arkilic, E.B., M. Schmidt, and K. Breuer, *Gaseous slip flow in long microchannels.* Journal of Microelectromechanical systems, 1997. **6**(2): p. 167-178.

170. Lim, C., et al., *Application of lattice Boltzmann method to simulate microchannel flows.* Physics of Fluids, 2002. **14**(7): p. 2299-2308.

171. Berning, T., D.M. Lu, and N. Djilali, *Three dimensional computational analysis of transport phenomena in a PEM fuel cell.* J.Power Sources, 2002. **106**: p. 284-294.

172. Berning, T., D.M. Lu, and N. Djilali, *Three-dimensional computational analysis of transport phenomena in a PEM fuel cell.* Journal of Power Sources, 2002. **106**(1-2): p. 284-294.

173. Lange, K.J., P.C. Sui, and N. Djilali, *Determination of effective transport properties in a PEMFC catalyst layer using different reconstruction algorithms.* J.Power Sources, 2012. **208**: p. 354-365.

174. Lange, K.J., P.C. Sui, and N. Djilali, *Determination of effective transport properties in a PEMFC catalyst layer using different reconstruction algorithms.* Journal of Power Sources, 2012. **208**: p. 354-365.

175. Wu, R., et al., *Pore network modeling of cathode catalyst layer of proton exchange membrane fuel cell.* Int.J.Hydrog.Energy, 2012. **37**: p. 11255-11267.

176. Wu, R., et al., *Pore network modeling of cathode catalyst layer of proton exchange membrane fuel cell.* International Journal of Hydrogen Energy, 2012. **37**(15): p. 11255-11267.

177. Siddique, N.A. and F.Q. Liu, *Process base reconstruction an simulation of a three dimensional fuel cell catalyst layer.* Electrochimica Acta, 2010. **55**.

178. Siddique, N.A. and F.Q. Liu, *Process based reconstruction and simulation of a three-dimensional fuel cell catalyst layer.* Electrochimica Acta, 2010. **55**(19): p. 5357-5366.

179. Lange, K.J., P.C. Sui, and N. Djilali, *Pore scale mideling of a proton exchange membrane fuel cell catalyst layer:effect of water vapor and temperature.* J.Power Sources, 2011. **196**: p. 3195-3203.

180. Lange, K.J., P.C. Sui, and N. Djilali, *Pore scale modeling of a proton exchange membrane fuel cell catalyst layer: Effects of water vapor and temperature.* Journal of Power Sources, 2011. **196**(6): p. 3195-3203.

181. Uchida, M., et al., *Investigation of the microstructure in the catalyst layer and effects of both perfluorosulfonate ionomer and PTFE-loaded carbon on the catalyst layer of polymer electrolyte fuel cells.* Journal of the Electrochemical Society, 1995. **142**: p. 4143-4149.

182. Xie, J., et al., *Porosimetry of MEAs made by "Thin Film Decal" method and its effect on performance of PEFCs.* Journal of the Electrochemical Society, 2004. **151**: p. 1841-1846.

183. Zhong, C.J., et al., *Nanostructure catalysts in fuel cells.* Nanotechnology, 2010. **21**: p. 1-20.

184. Guo, Z., T.S. Zhao, and Y. Shi, *Physical symmetry, spatial accuracy and relaxation time of the lattice Boltzmann equation for micro gas flows.* Journal of Applied physics, 2006. **99**.

185. Guo, Z., T.S. Zhao, and Y. Shi, *Physical symmetry, spatial accuracy, and relaxation time of the lattice Boltzmann equation for microgas flows.* Journal of Applied Physics, 2006. **99**(7).

186. Guo, Z.L., et al., *Discrete effects on boundary conditions for the lattice Boltzmann equation in simulating microscale gas flows.* Phys.Rev.E., 2007. **76**: p. 056704.

187. Guo, Z.L., T.S. Zhao, and Shi.Y., *Physical symmetry,spatial accuracy, and relaxation time of the lattice Boltzmann equation for microgas flows.* J. Appl. Phys., 2006. **99**: p. 074903.

188. Guo, Z.L., et al., *Discrete effects on boundary conditions for the lattice Boltzmann equation in simulating microscale gas flows.* Phys.Rev.E, 2007. **76**: p. 056704.

189. Chai, Z.H., et al., *Gas glow through square arrays of circular cylinders with klinkenberg effect: a lattice Boltzmann study.* Commun.Comput.Phys., 2010. **8**: p. 1052-1073.

190. Chai, Z.H., et al., *Gas flow through square arrays of circular cylinders with klinkenberg effect: a lattice Boltzmann study.* Commun. Comput. Phys., 2010. **8**: p. 1052-1073.

191. Weng, C.I., W.L. Li, and C.C. Hwang, *Gaseous flow in microtubes at arbitary Knudsen numbers.* Nanotechnology, 1999. **10**: p. 373-379.